Design, Fabrication, and Characterization of Biocompatible Soft Strain Sensors for Implantable Applications

by

Abdulkadir Yasin Atik

A Dissertation Submitted to the
Graduate School of Sciences and Engineering
in Partial Fulfillment of the Requirements for
the Degree of

Master of Science

in

Mechanical Engineering

April 28, 2025

Design, Fabrication, and Characterization of Biocompatible Soft Strain Sensors for Implantable Applications

Koç University

Graduate School of Sciences and Engineering

This is to certify that I have examined this copy of a master's thesis by

Abdulkadir Yasin Atik

and have found that it is complete and satisfactory in all respects,
and that any and all revisions required by the final
examining committee have been made.

Committee Members:

_____

Assist. Prof. Levent Beker (Advisor)

_____

Assist. Prof. Murat Kuşcu

_____

Prof. Can Yücesoy

Date: _____

To my family,

for their unwavering love, sacrifices, and constant belief in me.

To my dearest friends,

for their encouragement, understanding, and the laughter that made this journey lighter,

And to the love of my life,

thank you for your boundless support, your patience,

and for being my greatest source of strength and joy.

ABSTRACT

Design, Fabrication, and Characterization of Biocompatible Soft Strain Sensors for Implantable Applications

Abdulkadir Yasin Atik

Master of Science in Mechanical Engineering

April 28, 2025

Cardiovascular diseases remain a major global health challenge, with effective post-operative monitoring critical for improving patient outcomes and reducing hospital readmissions. This study presents the design, fabrication, and characterization of biocompatible soft strain sensors for implantable applications, focusing on continuous and precise cardiac strain monitoring. Two sensor types were developed: resistive and capacitive. While the resistive sensors provided initial insights, they faced durability limitations under cyclic loading, leading to the design of capacitive sensors with interdigitated configurations.

The capacitive sensors were constructed with polydimethylsiloxane encapsulation and 25 μm copper conductive elements. Theoretically, this design yielded a baseline capacitance of 0.228 pF and demonstrated sensitivity increments of 10, 20, and 30 fF under 5%, 10%, and 15% strain, respectively. Durability tests included continuous cyclic loading at 10% strain for over 12 hours, where the sensors exhibited minimal baseline drift and consistent signal integrity. Additionally, the capacitive sensors maintained stability under large strain amplitudes of 25% and demonstrated pressure insensitivity, ensuring operational reliability in dynamic physiological environments.

Characterization under simulated cardiac conditions using a ViVitro Superpump confirmed the sensor's ability to detect minimal volumetric changes and to accurately trace distinct phases of a heartbeat. These findings underscore the potential of the proposed sensors for real-time telemetric cardiac monitoring, offering high sensitivity, durability, and biocompatibility. This work lays a critical foundation for next-generation implantable devices aimed at enhancing cardiovascular care.

ÖZETÇE

İmplant Uygulamaları için Biyo-uyumlu gerinim sensörlerinin tasarım, üretim ve karakterizasyonu

Abdulkadir Yasin Atik

Makine Mühendisliği, Yüksek Lisans

28 Nisan 2025

Kardiyovasküler hastalıklar, dünya genelinde önemli bir sağlık sorunu olmaya devam etmekte ve ileri teşhis ve tedavi araçlarına olan ihtiyacı vurgulamaktadır. Sol ventrikül gerinim analizi yoluyla sürekli kardiyak izleme, özellikle ameliyat sonrası sonuçların iyileştirilmesinde ve hastane tekrar yatış oranlarının azaltılmasında önemli bir potansiyel sunmaktadır. Bu çalışma, hassas ve uzun vadeli kardiyak izleme çözümleri için özel olarak tasarlanmış biyouyumlu yumuşak gerinim sensörlerinin tasarımı, üretimi ve karakterizasyonuna odaklanmaktadır. Direnç tabanlı ve kapasitif olmak üzere iki sensör tipi geliştirilmiştir. Direnç bazlı sensörler, gerinim ölçümünde uygulanabilirliği göstermiş, ancak döngüsel yükleme altında dayanıklılık sorunlarıyla karşılaşmıştır. Bu bağlamda, istikrar ve hassasiyet açısından üstünlük sunan tarak konfigürasyonlu kapasitif sensörler tasarlanmıştır. Polidimetilsiloksan ile enkapsüle edilen ve 25 μm bakır iletken elemanlarla üretilen kapasitif sensörler, tasarımında teorik olarak 0,228 pF'lik bir başlangıç kapasitansı sağlamış ve sırasıyla %5, %10 ve %15 gerinim altında 10, 20 ve 30 fF kapasitans artışları göstermiştir. Dayanıklılık testlerinde, sensörler 12 saat döngüsel gerinime maruz bırakılmış ve minimal başlangıç kayması ve tutarlı sinyal devamlılığı sergilemiştir. Ayrıca, kapasitif sensörler %25 gibi büyük gerinim genliklerinde stabil kalmış ve çeşitli kuvvetlere karşı basınç duyarsızlığı göstermiştir, bu da dinamik fizyolojik ortamlar için operasyonel güvenilirliği garanti etmektedir. ViVitro Superpump kullanılarak simüle edilmiş kardiyak koşullar altında yapılan karakterizasyon, sensörün düşük hacimsel değişiklikleri algılama ve bir kalp atışının farklı evrelerini doğru bir şekilde izleme yeteneğini doğrulamıştır. Bu bulgular, önerilen sensörlerin gerçek zamanlı telemetrik kardiyak izleme için yüksek hassasiyet, dayanıklılık ve biyouyumluluk sunduğunu göstermektedir. Bu çalışma, kardiyovasküler bakımı geliştirmeyi amaçlayan bir sonraki nesil implant edilebilir cihazlar için kritik bir temel oluşturmaktadır.

AKNOWLEDGEMENTS

First and foremost, I would like to express my deepest gratitude to my supervisor, Dr. Levent Beker, for his invaluable guidance, patience, and encouragement throughout the course of my thesis. His insight and expertise have played a crucial role in shaping my academic journey and this work.

I would also like to extend my sincere thanks to my fellow colleagues and friends at the Bio-Integrated Microdevices Lab, whose collaboration and support made both the research and daily work an inspiring experience. The knowledge shared and the friendships formed during this time have meant a great deal to me.

I am also thankful to the Scientific and Technological Research Council of Turkey (TÜBİTAK) 2210 National Scholarship Program for their generous financial support, which allowed me to focus on my studies and research without distraction.

TABLE OF CONTENTS

LIST OF FIGURES

ABBREVIATIONS

HF	Heart Failure
SIRS	Systemic Inflammatory Response Syndrome
TEE	Transesophageal Echocardiography
CPB	Cardiopulmonary Bypass
TTE	Transthoracic Echocardiography
SNR	Signal-to-Noise Ratio
PDMS	Polydimethylsiloxane
PET	Polyethylene Terephthalate
ADC	Analog-To-Digital Converter
FEA	Finite Element Analysis

Chapter 1:
INTRODUCTION

1.1 Cardiovascular Diseases

Heart failure (HF), a condition in which the heart cannot pump enough blood to meet the body's needs, poses a significant health and economic challenge worldwide [1]. Affecting over 6 million adults in the United States alone, HF incurs an annual cost exceeding $30 billion [2]. Globally, cardiovascular diseases remain the leading cause of death, accounting for an estimated 19 million fatalities in 2020—a staggering 18.7% increase from 2010 [3]. The increasing incidence of heart disease has resulted in more elective cardiac surgeries and heart transplantations, especially among older populations, emphasizing the critical need for effective management strategies. [4].

Coronary heart disease, the most common type of heart disease in the United States, was responsible for 382,000 deaths in 2020 [5]. Advanced cardiovascular interventions, such as coronary artery bypass grafting—the most frequently performed surgery for cardiac disease—and mechanical circulatory support devices, have significantly improved patient outcomes and extended lifespans. Despite these advancements, high-risk patients, though constituting less than 15% of in-patient procedures, account for a staggering 80% of deaths [6]. Furthermore, gaps in post-acute care remain evident, with unplanned readmission rates as high as 20% [7], [8]. Continuous and reliable monitoring of cardiac activity has emerged as a promising solution. It helps patients stick to their medication plans, improves the quality of care, and lowers costs for outpatient visits and hospital stays. [9]. This approach has proven particularly effective for chronic heart failure patients, enabling cost-effective reductions in hospitalizations and improved long-term outcomes [10], [11].

Open-heart surgery has historically played a pivotal role in improving survival rates for patients with cardiovascular disease [12]. However, the postoperative phase can be very challenging, especially for patients with HF. These patients have a much higher risk of death after surgery compared to those without HF. [13]. In complex surgeries, the one-year mortality rate can climb as high as 30%, highlighting the urgent need for enhanced care strategies for high-risk individuals [14]. Complications such as chest pain, kidney

and liver failure, and neurological disorders often hinder recovery, with 1 in 4 patients being rehospitalized within six months of surgery [15]. These complications severely impact the cardiovascular system's physiology during and after surgery, making improved postoperative outcomes a critical factor for functional recovery, long-term survival, and reducing healthcare costs [16], [17], [18].

Systemic inflammatory response syndrome (SIRS) and vasoplegia are common postoperative complications, with incidence rates ranging from 5%–25% in the general population and up to 50% in high-risk groups, significantly lowering survival rates [19]. After surgery, heart function can get worse over days or weeks. This decline often happens outside of hospitals and may go unnoticed during occasional check-ups [20]. By the time symptoms become evident, irreversible myocardial damage and functional impairments may have already taken hold [21], [22], [23], [24], [25]. Continuous monitoring systems offer a critical solution, enabling the timely detection of major adverse cardiac events such as malignant ventricular arrhythmias or myocardial infarctions. This early detection can dramatically improve clinical outcomes and patient recovery [26], [27], [28].

The lack of quantitative monitoring following cardiac surgery leaves a significant gap in patient care, leading to a cycle of worsening conditions that includes hospitalization, treatment, and readmission [29], [30]. Currently, patients are discharged without medical monitoring devices, and healthcare providers must rely on subjective patient reports to assess the need for rehospitalization. Implementing a reliable method to quantitatively monitor cardiac function—specifically cardiac output—could enable early detection of complications, significantly improving patient outcomes. Continuous monitoring of left and right heart volumes is particularly crucial for optimizing survival during surgery and postoperative intensive care [18], [19], [31]. For high-risk HF patients, early detection of declining cardiac function in both LV and RV is vital for effective post-acute care and preventing irreversible deterioration [18], [23], [32], [33].

Monitoring LV activity is crucial for detecting systolic and diastolic dysfunctions and identifying early signs of HF [34], [35], [36]. Recent studies highlight myocardial strain as a sensitive and robust early indicator of cardiac dysfunction, offering superior prognostic value compared to traditional metrics [37], [38], [39]. Preclinical investigations reveal that abnormalities in myocardial strain emerge earlier in the progression of HF than other factors, such as changes in ventricular filling pressures [40],

[41], [42], [43], [44], [45], [46]. The measurement of ventricular strain, primarily through advanced imaging techniques like magnetic resonance and ultrasound, is an area of active research in cardiovascular medicine [47], [48]. Reduced strain, often coupled with increased myocardial stiffness, serves as a hallmark of cardiomyopathy progression and is a strong predictor of major adverse cardiac events, disability, and mortality in clinical settings [49], [50]. This evidence underscores the potential of strain metrics in improving early diagnosis and intervention strategies for HF patients.

During surgery, heart volume is typically monitored indirectly through central venous pressure measured via invasive pressure lines and visualized using transesophageal echocardiography (TEE) [19]. This continuous monitoring enables real-time volume management, such as administering or retaining fluid through a modified cardiopulmonary bypass (CPB). Post-surgery, patients are moved to the intensive care unit, where TEE is discontinued due to its need for sedation [51] (Figure 1.1). During the critical first 48 hours, patients are at high risk for complications like vasoplegia and SIRS, which cause blood to leak into the periphery. This reduces the heart's filling volume at end-diastole, impairing stroke volume and cardiac output. Early detection of these volume changes allows timely fluid administration to restore cardiac function; otherwise, severe outcomes may occur.

The most commonly used device for LV volume measurement in clinical settings is transthoracic echocardiography (TTE) [52] (Figure 1.1). However, TTE has limitations, including its reliance on a clinician to manually position the probe for optimal imaging, which affects reproducibility and accuracy [53]. Continuous LV volume measurement methods, such as intra-cardiac electric impedance via a catheter, offer improved precision but are associated with significant thromboembolic risks, limiting their use to short-term experimental animal studies. This underscores the need for a safer, continuous, and reliable LV volume monitoring solution for better clinical outcomes [54], [55], [56].

a) b)

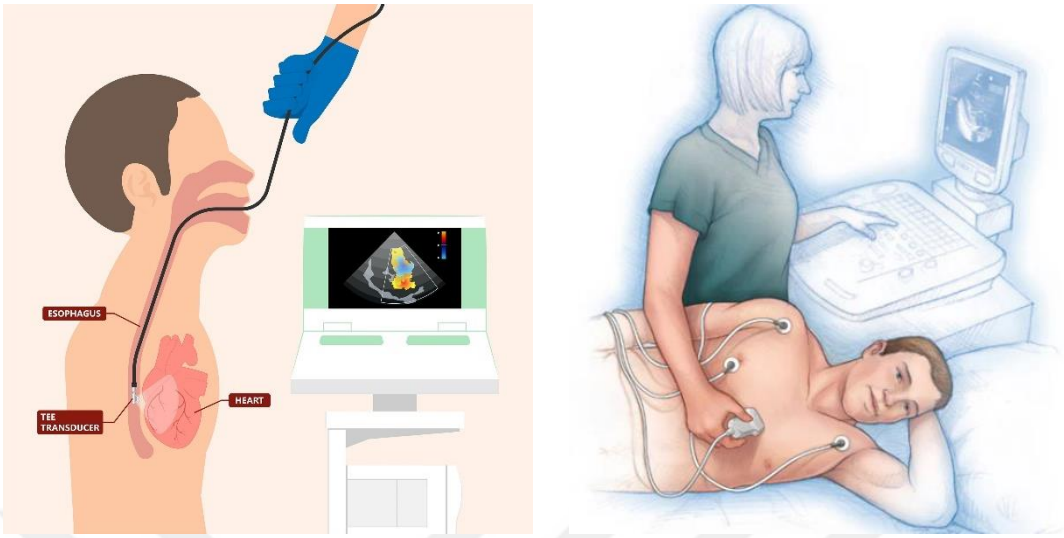

Figure 1.1: Conventional methods for detecting heart volume. a) TEE [57] , b) TTE [58].

Explained by the Frank Starling mechanism, LV volume and myocardial strain are closely related to cardiac output, physiologically [59]. Strain is a specific metric and can be measured along multiple axes. It provides clear insights into health conditions and helps in understanding different disease types, leading to better ways to categorize them. [60], [61]. Studies have shown that left ventricular epicardial strain closely correlates with preload and stroke volume, making it a valuable parameter for evaluating hemodynamic performance [62]. Beyond cardiac tissue, strain measurements can be applied to compliant outflow vessels, such as the aorta, where circumferential strain serves as an indicator of systolic pressure. This versatility highlights the broad utility of strain analysis in both cardiac and vascular contexts [63].

Traditional imaging systems for cardiac monitoring are limited by their reliance on operator-driven investigations and their confinement to hospital settings, making them unsuitable for continuous use. An implantable, soft, miniaturized, and sensitive strain-sensing device could revolutionize cardiac care by enabling long-term monitoring of critical parameters in everyday settings. Such a device would facilitate the early detection of major cardiac adverse events at home and allow real-time tracking of the heart's response to medications, paving the way for personalized therapies. Implantable cardiac sensors, positioned in closer proximity to the heart, offer significant advantages, including enhanced precision, a higher signal-to-noise ratio (SNR), and the ability to detect subtle changes in cardiac activity [64]. While technologies like the CardioMEMS (Abbott, IL, USA) pressure sensors provide valuable data on pulmonary artery pressures correlated

with left ventricular function, they are influenced by pulmonary resistance and fail to address the need for direct LV myocardial strain [65], [66], [67]. Thus, the demand for an innovative sensor technology persists—one that can detect LV strain anomalies in real time, remain permanently implanted due to its small size, and ensure biocompatibility for long-term use.

In addition to transthoracic echocardiography (TTE) and transesophageal echocardiography (TEE), several alternative techniques exist for cardiac volume and output monitoring. Doppler ultrasound, particularly pulsed-wave Doppler (PWD), offers a non-invasive means to estimate stroke volume by measuring blood flow velocities across cardiac valves, combined with anatomical estimations of valve cross-sectional areas [68]. While widely utilized, Doppler-based methods inherently provide flow-derived rather than direct volumetric measurements and are highly operator-dependent, with significant accuracy contingent upon correct alignment and anatomical assumptions. Cardiac magnetic resonance imaging (MRI) represents the gold standard for precise volumetric assessment, offering high-resolution, three-dimensional visualization of ventricular volumes and ejection fractions; however, it remains impractical for continuous monitoring due to high cost, limited accessibility, and procedural duration [69]. Computed tomography (CT) angiography similarly provides detailed static volumetric data but is primarily restricted to anatomical evaluations owing to radiation exposure and its non-continuous nature [70]. Emerging technologies such as bioimpedance cardiography estimate stroke volume by detecting changes in thoracic electrical impedance during the cardiac cycle, offering continuous, non-invasive monitoring albeit with reduced accuracy in patients with high body mass or fluid overload [71]. Additionally, pulse contour analysis techniques based on arterial waveform monitoring (e.g., PiCCO, LiDCO systems) allow semi-continuous estimation of cardiac output in critical care settings, though they infer rather than directly measure ventricular volume [72]. Implantable pressure sensors, exemplified by CardioMEMS, indirectly assess cardiac function by monitoring pulmonary artery pressures but lack direct left ventricular volume measurement capability [73]. Overall, while multiple modalities are available, each presents specific limitations in terms of invasiveness, continuity, or precision, underscoring the clinical need for novel implantable technologies capable of direct, continuous heart volume monitoring—such as the strain-sensing device proposed in this study.

1.2 Implantable Devices

Research in implantable devices has garnered substantial interest over the past few years, leading to significant advancements in the field. This surge in interest can be attributed to the growing potential of these devices to improve patient outcomes and enhance quality of life. Recent studies have reported a variety of innovative implantable devices that have successfully demonstrated their functionality and efficacy in vivo. These developments highlight the ongoing commitment to refining medical technologies that can be integrated into the human body, paving the way for new therapeutic approaches and monitoring solutions in healthcare.

Biodegradable materials are used by Boutry et al. In this work, they created an arterial blood flow monitor implant, which is completely biodegradable and transmits signals wirelessly. It works as a pressure sensor just as a capacitor utilizing fringing-field capacitance. Having minimal hysteresis, short response time and very good cyclic stability on top of being undoubtedly robust are present on the sensor. With these capabilities, the sensor happens to be a ready-to-use implant. Hence, an in vivo test is demonstrated in the study with rats. Surgeons delicately sutured the sensor on femoral vessel and signals are collected via a Vector Network Analyzer. This study paves the way for using capacitance-based sensing on implantable applications [74].

Providing sensitive electrical signal with an implant having mechanical properties close to myocardial tissue is demonstrated for the first time in the study of Sim et al. They created an epicardial patch loaded with transistors ready to generate a spatiotemporal map of the patient's heart. This is done by fabricating fully rubbery transistor array encapsulated by biocompatible elastomer. The elastomer lets the implant stretch in harmony with heart while measuring vitals like temperature and strain. They showed the capabilities of the device on a beating porcine heart. Also, with slight adjustments, the device can be therapeutic and harvest its own energy from heart beats [75].

CardioMEMS (Abbott, IL, USA) is a wireless, implantable monitoring device designed to track pulmonary artery pressure (PAP) in heart failure (HF) patients. Approved by the FDA in 2014, it plays a significant role in early detection and management of HF by enabling remote hemodynamic monitoring. The device consists of a pressure sensor implanted in the pulmonary artery, which operates without batteries or leads, relying on radiofrequency signals for power. Patients transmit daily pressure

readings through an external electronic unit and an antenna-equipped pillow. This real-time data allows healthcare providers to make timely adjustments to medication, reducing the risk of hospitalizations and improving patient outcomes. Studies have demonstrated that CardioMEMS significantly lowers HF-related admissions and may contribute to mortality reduction. Beyond HF, it has shown potential applications in monitoring pulmonary hypertension, optimizing left ventricular assist devices (LVADs), and early detection of cardiovascular complications [76].

Hwang et al. present an innovative single-device platform for in situ cardiac diagnosis and treatment, integrating mechanophysiological sensing and therapeutic electrical stimulation. Unlike conventional electrophysiological methods that rely on electrical signal detection, this platform employs an active-matrix array of pressure-sensitive transistors to monitor cardiac pressure distribution in real time, ensuring minimal interference with electrical pacing signals. The device also features biocompatible, low-impedance platinum-black electrodes for efficient cardiac stimulation and an alginate-based hydrogel adhesive for stable attachment to the epicardium. In vivo experiments on rabbits demonstrate the system's ability to detect abnormal heart rhythms and synchronize cardiac pacing with high precision. The key novelty of this study lies in its seamless integration of pressure-based sensing with therapeutic electrical stimulation within a single platform, enabling simultaneous diagnosis and treatment of arrhythmias while overcoming the limitations of ECG-based monitoring [77].

Liu et al. introduce a self-powered, ultrasensitive endocardial pressure sensor (SEPS) based on a triboelectric nanogenerator (TENG) for real-time cardiac monitoring. Unlike conventional pressure sensors that require external power sources and are limited in long-term applications, this device harnesses the energy from blood flow to generate electrical signals, enabling continuous monitoring without battery dependency. The SEPS is miniaturized, flexible, and integrated with a surgical catheter for minimally invasive implantation, making it suitable for real-time tracking of endocardial pressure changes. In vivo experiments in a porcine model demonstrate its high sensitivity (1.195 mV $mmHg^{-1}$) and excellent linearity ($R^2 = 0.997$), allowing detection of both normal cardiac function and pathological conditions such as ventricular fibrillation. This study shows a remarkable combination of self-powering capability, high sensitivity, and minimally invasive design, paving the way for next-generation implantable cardiovascular sensors [78].

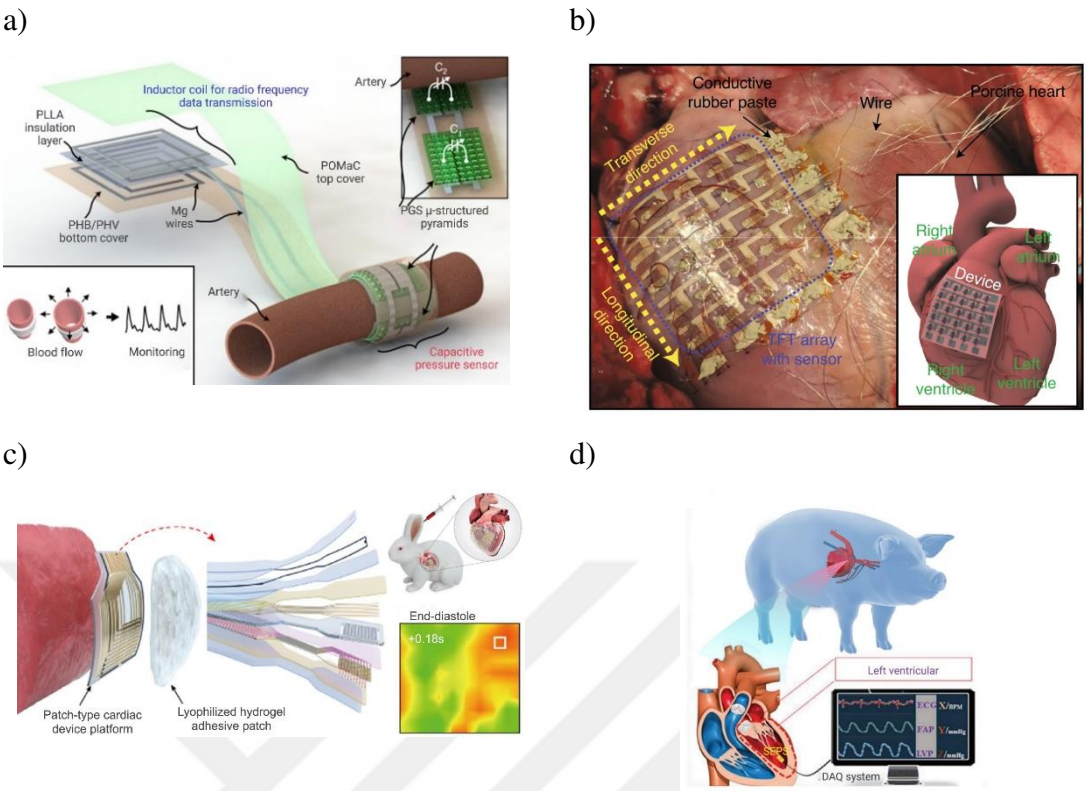

Figure 1.2: a) A fully biodegradable, wireless arterial-pulse sensor based on fringe-field capacitor technology, enabling real-time, battery-free blood flow monitoring after surgery without requiring device removal [74]. b) A soft, stretchable epicardial bioelectronic patch, enabling spatiotemporal mapping of electrophysiological activity, strain, and temperature while conforming seamlessly to a beating heart [75]. c) A single-device platform that integrates mechanophysiological sensing and therapeutic electrical stimulation for real-time, in situ cardiac diagnosis and treatment, using a pressure-sensitive transistor array to overcome the limitations of traditional ECG-based monitoring [77]. d) A self-powered, ultrasensitive endocardial pressure sensor based on a triboelectric nanogenerator, enabling real-time, battery-free cardiac pressure monitoring with high sensitivity and minimal invasiveness [78].

Flexible electronics hold great promise for cardiovascular healthcare monitoring, but several challenges hinder their widespread clinical adoption. One major issue is the trade-off between flexibility, durability, and electrical performance; achieving high mechanical stretchability while maintaining stable signal transmission remains difficult. Motion artifacts caused by unpredictable body movements can distort readings, affecting the reliability of continuous monitoring. Additionally, power consumption and energy sustainability present challenges, as many flexible sensors still require external power sources, limiting their long-term usability. Biocompatibility and long-term stability are also concerns, as implantable or skin-mounted devices must integrate seamlessly with biological tissues without causing adverse reactions. Furthermore, data accuracy and processing require improvements, as noise interference and calibration complexities can impact diagnostic reliability. Overcoming these challenges will require advancements in

materials, fabrication techniques, and signal-processing algorithms to ensure flexible electronics provide reliable, real-time monitoring for cardiovascular health.

1.3 Strain Sensors

Dr. Arthur C. Ruge is credited with creating the first strain sensor in 1938, and his fundamental strain sensing mechanism is still used in most commercial sensors today. The initial strain gauge relies on the relationship between electrical resistance and material geometry, favoring highly conductive and sometimes ductile materials for their lower voltage requirements and broader elasticity range.

Soft material sensors have a low modulus and are flexible, which helps solve problems that stiffer sensors face. Because of their flexibility, these sensors can easily fit onto curved surfaces and can measure a larger range of movements. Many devices, such as wearables, implants, soft robots, and flexible robots, need strain sensors that can handle more than 30% strain. In contrast, traditional strain gauges often break at strains of 5% or less. Additionally, differences in stiffness can cause the sensors to delaminate, leading to inaccurate measurements.

The effectiveness of soft sensors depends a lot on the choice of soft conductors and the elastomers that cover them. The main materials used for the elastomeric layer in sensors are Polydimethylsiloxane (PDMS), Ecoflex series, and Dragon Skin. Polyurethane-based elastomers are also commonly used because they have a wide range of stiffness and can be 3D printed. Flexible conductors can be divided into three types based on their material and structure: conductive liquids, conductive composites, and soft structural conductors. Each type will be discussed in the following sections.

1.3.1 Conductive Liquids

For a liquid to exhibit electrical conductivity, it is essential for it to contain free electrons. This property can be accomplished in two primary ways: the use of liquid metals, which have a high density of free electrons, or by dissolving ionic compounds in a liquid, creating charged particles that can move freely and carry an electrical current. A particularly innovative and effective method for creating a soft strain sensor involves encapsulating a conductive liquid within a soft elastomer. This approach not only provides a high degree of flexibility and sensitivity but also minimizes the risks typically

associated with electronic components, such as rupture or delamination. By employing this technique, the durability and reliability of the sensor are significantly enhanced, making it suitable for a variety of applications where strain detection is critical.

High hysteresis is commonly observed in sensing applications utilizing liquid conductors, particularly in microfluidic systems. This phenomenon often stems from the deformation of the microfluidic channels themselves, which can occur under pressure or flow conditions. Additionally, there are inherent delays in liquid recovery after the initial loading phase, further contributing to inconsistencies in sensor readings. A significant challenge in accurate measurements lies in the need to differentiate between the genuine sensor signals and the piezoresistive effects generated by the cabling connected to the sensors [79].

While liquid conductors are capable of effectively measuring substantial deformations, they come with complications. The high conductivity associated with liquid metals, for example, tends to result in a decrease in measurement resolution. This trade-off between the ability to detect large changes and the precision of the readings is critical to consider in the design and implementation of sensing technologies [80].

1.3.2 Conductive Composites

Conductive composites are comprised of elastomeric matrix and conductive fillers. Their mechanical and electrical properties can be delicately adjusted via changing the base elastomer and filler ratios. They can be integrated in microfabrication processes and therefore have the potential for miniaturization. Considering these, they are good candidates for implantable devices.

Almost all of the conductive composite sensors rely on piezoresistive effects. This is an advantage since easy-read out circuits like Wheatstone bridges can be integrated. However, piezoresistive sensors are known for their high hysteresis and varying nominal resistance. This is due to the continuously changing pathways of electric current in the composite with respect to applied strain. This effect worsens as the number of cycles the sensor is exposed to increases.

Dual et al. developed an innovative implantable soft strain sensor that incorporates gold-coated titanium dioxide nanowires (Au-TiO2 NW), encapsulated within a soft elastomeric material PDMS. The choice of gold and titanium is significant, as researchers

are actively seeking alternatives to silver, which is traditionally the most common conductive filler used in conductive composite sensors.

In their study, the sensor was subjected to an extensive testing regimen that included a 72-hour cyclic deformation experiment, where it experienced a strain of 30%. This assessment was carried out using an ex vivo model, in addition to a shorter-duration experiment performed on an in vivo porcine model to evaluate its performance in a living organism.

Results from these experiments indicated a progressive increase in the resistance of the sensor, aligning with expectations due to the reorientation and potential disconnection of the Au-TiO2 NW during the cyclic loading. This change in resistance is a critical parameter, as it reflects the sensor's material behavior under sustained mechanical stress.

The researchers hypothesize that with the implementation of an effective preconditioning process in future work, the resistance of the sensor could eventually stabilize at a steady state. This stabilization would be significant, as it would mean that the introduction of an increasing number of cycles would not lead to further changes in resistance, thereby enhancing the reliability and longevity of the sensor in practical applications [62].

1.3.3 Structurally Soft Conductors

Soft sensors that incorporate embedded structurally soft conductors are commonly designed using a combination of elastomeric films and more rigid conductive materials such as silicon and copper. These traditional rigid conductors are essential for effective sensing but can limit the overall flexibility and stretchability of the sensor. To overcome this challenge, engineers and designers employ geometric tuning techniques that modify the arrangement and dimensions of the embedded conductors, promoting a balance between conductivity and the necessary mechanical properties.

One of the primary strategies for enhancing flexibility involves adjusting the thickness of the metallic conductors. By reducing their thickness, the conductive elements become more compliant and capable of bending without compromising their electrical performance. This adaptation is crucial for applications where the sensor must conform to dynamic surfaces or be subjected to frequent deformation.

In addition to thickness modification, the use of innovative structural designs, such as wavy or serpentine patterns, plays a key role in enhancing the stretchability of the conductors. These non-linear geometries allow the conductors to expand and contract significantly without breaking or losing their conductive properties. By strategically implementing these design principles, soft sensors can effectively maintain functionality while adapting to a wide range of movements and environmental conditions. This approach not only increases the usability of soft sensors in various applications, including wearable and implant technology but also opens up new possibilities for creating devices that require both flexibility and reliable electrical performance.

Despite the inherent flexible and stretchable characteristics of structurally soft conductors, these materials are not without their limitations, particularly due to certain rigid aspects. The utilization of serpentine patterns in these conductors, which is a common strategy to enhance flexibility, results in an increased volume requirement. Consequently, the operational range per unit area or volume remains lower compared to entirely soft sensors. However, one of the advantages of using rigid conductors is their compatibility with micromachining techniques. These special fabrication methods allow for the miniaturization of these conductors, making them suitable for use in implantable devices.

Moreover, the ability to freely pattern these rigid materials opens up possibilities for employing capacitive sensing technology rather than relying solely on piezoresistive sensing. Capacitive sensing is particularly advantageous as it typically avoids certain defects that trouble piezoresistive sensors, such as hysteresis and fluctuations in nominal resistance. In contrast to piezoresistive sensors, which measure changes in resistivity, capacitive sensors primarily respond to changes in the geometry of the sensor structure. This distinction provides capacitive sensors with the capability to deliver more reliable measurements, especially when dealing with dynamic loads and rapid rate changes [81].

Both capacitive and resistive sensors share the benefit of relatively straightforward architectures, which often include designs such as interdigitated combs and parallel plates. This simplicity in design enhances their practicality and appeal for various applications. Given these compelling attributes, capacitive sensing has been chosen as the foundational mechanism for the strain sensors developed in this study. The decision to utilize capacitive sensing was driven by the desire to leverage its promising attributes,

thereby enhancing the overall performance and reliability of the strain sensing technology.

1.4 Scope of the Thesis

In this research, we propose a novel soft implantable cardiac strain sensor specifically designed to facilitate essential telemetric measurements for patients who have undergone open-heart surgeries, such as coronary artery bypass grafting. These patients are at an increased risk of readmission due to complications like vasoplegia, making continuous monitoring critical for their post-operative care.

One of the unique aspects of this study is the exploration of the effect of the distance between the neutral axis and the sensing layer of the strain sensor, a topic that has not been addressed in the existing literature until now. By conducting controlled experiments, we aim to investigate how this distance impacts sensor performance. A primary design goal for our sensor is to ensure its functionality and accuracy regardless of the pressure applied during use.

The first phase of this thesis centers on the design, fabrication, and characterization of a resistive soft strain sensor. We described the fundamentals of the sensor's design process and evaluated the experiment results, discussing the strengths and weaknesses observed in our findings. Based on these observations, we seek to identify potential design improvements; specifically, we explore the use of capacitance as a more effective measurement alternative.

The second phase of the study shifts focus to the development of a capacitive soft strain sensor, which employs an interdigitated capacitor configuration with a transverse comb structure. We provide a detailed account of the design, fabrication, and characterization processes involved in creating this sensor. Each step of the design phases is meticulously documented, along with the results, which are thoroughly validated through both analytical and numerical methods. The analytical approach involves applying established formulas based on a series of assumptions to predict sensor behavior, while the numerical approach employs the finite element method within a multi-physics framework to simulate and analyze the sensor's performance under various conditions. This comprehensive approach ensures a robust understanding of the sensor dynamics and its potential applications in clinical settings.

Chapter 2:
DESIGN, FABRICATION AND CHARACTERIZATION OF RESISTIVE STRAIN SENSOR

2.1 Design

Piezoresistive strain sensors operate based on the principle that the resistance of a material changes when it experiences deformation. This change in resistance is fundamentally linked to the geometrical properties described in the resistance formula. The electrical resistance (R) of a piezoresistive strain gauge can be expressed in a simplified form as in the equation (2.1):

$$R = \rho \frac{L}{A} \tag{2.1}$$

where ρ represents the resistivity of the material, L is the length of the sensor, and A is its cross-sectional area.

When the sensor is subjected to stretching, its length increases, while its cross-sectional area decreases, a relationship defined by Poisson's ratio, which quantifies the tendency of a material to expand in directions perpendicular to the direction of compression or stretching. As a result of these changes, the overall resistance R of the strain gauge increases.

To fully comprehend the mechanical and electrical responses of the material, as well as to optimize the design of the strain sensors, multiple prototypes are developed and tested. These various iterations allow for systematic evaluation of their performance under different conditions and provide insights into how design parameters influence sensitivity and accuracy in measuring strain. The iterative prototyping process is crucial for refining the technology to meet specific application requirements.

2.2 Fabrication and Characterization

The fabrication of our sensor involves a detailed three-step process, beginning with the preparation of the substrate, which is composed of PDMS (Sylgard 184, Dow Corning Corporation, Midland, MI, USA). The first step involves creating the substrate by mixing PDMS base with a crosslinker in a precise 1:10 weight ratio. This mixture is thoroughly

stirred to ensure homogeneity before being placed in a desiccator to undergo a degassing process. This step is crucial as it removes any air bubbles entrapped within the PDMS solution, which could compromise the mechanical properties and performance of the final sensor.

Once the degassing is complete and all gas bubbles are eliminated, the liquid PDMS is carefully poured onto a prepared glass slide that has been coated with Parylene-C. The Parylene-C coating process itself requires careful control of conditions; the Parylene-C material is stored as dimers within a specialized coating device (Labcoater 100, PPS, Rosenheim, Germany). Under low-pressure and elevated temperature conditions, these dimers are converted into their monomer form, becoming volatile. As a result, when the Parylene-C monomers are deposited onto the glass surface, they interact with it at room temperature or lower, facilitating a deposition process where the monomers nucleate and polymerize to form a dense, thin layer of Parylene-C.

The Parylene-C consists of poly(chloro-p-xylylene), a polymer whose unique structure - particularly the presence of chlorine branches - endows it with pronounced hydrophobic properties (Figure 2.1). This hydrophobicity is pivotal, as it provides a protective barrier for the underlying glass surface, preventing the PDMS from adhering directly to it during the curing process. Consequently, when the PDMS layer is cured on the Parylene-C-coated glass slide, the interaction between the PDMS and the Parylene-C remains minimal, ensuring the integrity of both materials and optimizing the performance characteristics of the sensor. This careful construction methodology set the foundation for the sensor's functionality and reliability in its intended applications.

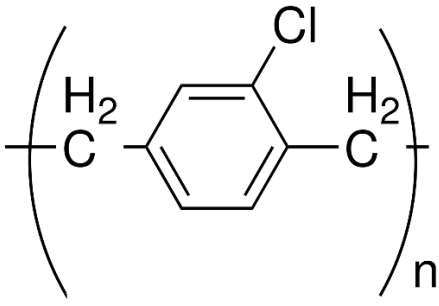

Figure 2.1: Repeating unit of Parylene-C

As the key sensing material for the sensor, we have chosen a conductive paste known as Intexar PE874 (DuPont de Nemours, Inc., Wilmington, Delaware, USA). This particular material is recognized for its exceptional recovery capability and consistent

performance when applied to elastomeric substrates, making it a suitable choice for our application.

To effectively apply this conductive paste onto the elastomeric substrates, we explored multiple methodologies, focusing on two primary techniques: screen printing and inkjet printing. Inkjet printing stands out for its speed and precision in fabrication, allowing for intricate designs to be realized efficiently. However, the implementation of inkjet printing necessitates the use of sophisticated equipment, which can significantly elevate the overall costs associated with sensor fabrication.

In contrast, screen printing emerges as a more cost-effective solution, requiring only a stencil for application. The stencils used in this process are meticulously crafted based on the specific geometrical designs intended for the sensing material, ensuring accuracy in the printing process. For the fabrication of these stencils, we utilized the LPKF R4 System (LPKF ProtoLaser R4, LPKF Laser & Electronics AG, Garbsen, Germany). The laser parameters were optimized to achieve the best results, set at a frequency of 300 kHz, with a power output of 7.3 W, a marking speed of 300 mm/s, and a total of three repetitions during the engraving process (Figure 2.2).

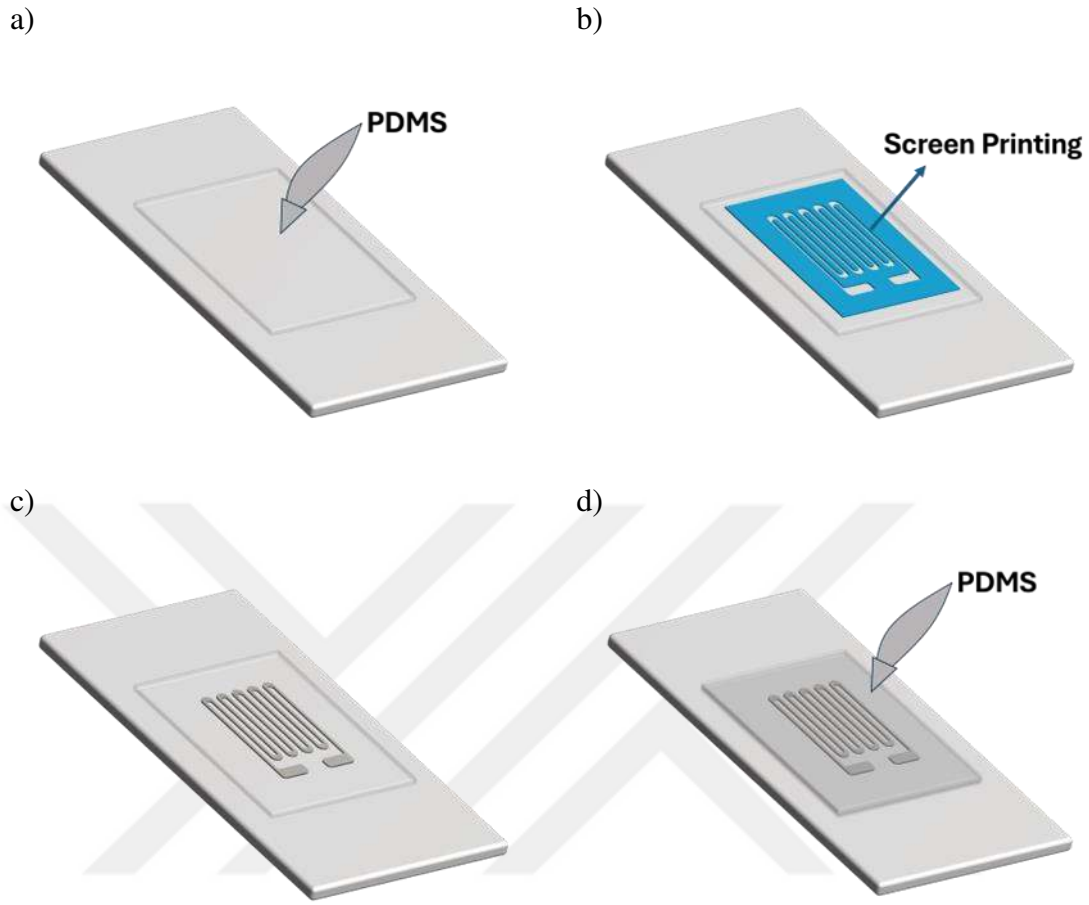

Figure 2.2: Fabrication flow of resistive strain sensor. a) PDMS substrate developed on the glass slide rigid layer. b) Stencil patterned with LPKF ProtoLaser R4 placed on PDMS substrate. c) Conductive paste is screen printed. d) The sensor is encapsulated with PDMS and carefully removed from glass.

As part of the design iteration process, the geometry of the sensing element was systematically refined based on experimental phases and their corresponding results. The initial design consisted of a simple pattern featuring a thick single line, which served as a foundational structure. This straightforward configuration enabled rapid experimentation, allowing us to obtain initial results swiftly thanks to its uncomplicated nature. Notably, the first design was executed without any encapsulation, providing a clear baseline for subsequent modifications and enhancements (Figure 2.3).

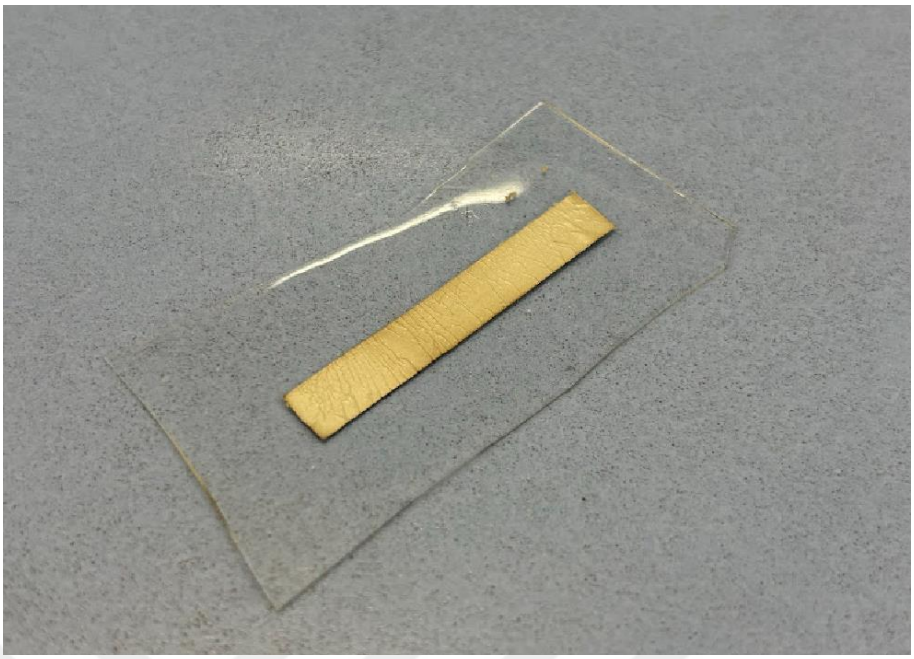

Figure 2.3: Single line design without encapsulation.

To begin the process of fabrication, encapsulation was deliberately omitted to facilitate the acquisition of initial results while conserving both materials and time. The first step involved curing a layer of PDMS on a clean glass slide. This PDMS film undergoes a curing process that involves the cross-linking of siloxane chains, which creates a solid elastomer. Upon completion of the curing phase, the PDMS film is carefully detached from the glass substrate to relieve any residual stress that may have developed during the curing process.

Once the PDMS film is separated, it is allowed to shrink to its final dimensions, and then it is placed on a flat, even surface to ensure stability. The next step involves cutting a stencil from a 33-micron thick polyethylene terephthalate (PET) sheet using an LPKF R4 laser cutter, following a specified recipe designed for precision. The dimensions of the stencil patterns are carefully chosen to be manageable while still suitable for the intended application. Specifically, the width is designed to accommodate the metal clips of the characterization device, ensuring secure attachment, while the length is optimized for a typical cardiac patch.

With the stencil prepared, attention turns to the application of conductive paste. To maintain alignment and to avert imperfections during the patterning process, the PDMS film is fixed onto another glass slide. Following this, the stencil is positioned on top of the glass slide with the PDMS substrate nested underneath, utilizing a spacer that is strategically placed between the stencil and the PDMS. The thickness of this spacer is

critical; if it is too thick, the paste may be under-applied, leading to ineffective patterns or incomplete coverage. Conversely, if the spacer is too thin, there is a risk that the stencil will detach prematurely from the PDMS film during the application, potentially damaging the pattern created.

Once the PDMS film, stencil, and spacer are securely arranged on the glass slide, it is time for the application of the conductive paste. To ensure optimal performance, if the conductive paste has not been utilized in over a week, it is advisable to mix it thoroughly before application. After preparing the paste, approximately one gram is taken using a suitable applicator, which can be made from flexible PET with a thickness of at least one millimeter or more. The paste is applied in a single, smooth swipe to achieve an even layer on the stencil.

Following the application, the stencil is very carefully removed to prevent any damage to the freshly patterned conductive paste underneath. With the glass slide now bearing the PDMS film and the patterned paste, the assembly is placed on a hot plate for curing. A constant temperature of 75°C is maintained for a duration of three hours. During this heating period, the conductive paste undergoes curing, and any solvent present within the paste evaporates, solidifying the pattern. After the designated time has elapsed, the sensor is allowed to cool to room temperature, at which point it is fully prepared for subsequent characterization.

The characterization of sensors can be approached from various perspectives, each focusing on different aspects and requirements that the sensor must fulfill. A fundamental step in this process is to ensure that the electrical signal responses and strain tests yield successful outcomes, as these preliminary tests establish a baseline for meeting additional criteria.

To effectively characterize the sensor, it is imperative to conduct electrical signal acquisition. This procedure typically necessitates specialized instrumentation such as a multimeter, an LCR meter, or an impedance analyzer. In pursuit of a precise and accurate characterization, the Zurich Instruments MFIA Impedance Analyzer (Zurich Instruments AG, Zürich, Switzerland), was selected for its exceptional capabilities.

One notable feature of the sensor design is the absence of traditional wiring, which necessitates the use of metal clips as probes for measurement. These clips provide a reliable and effective means of connecting to the sensor, allowing for accurate readings of the electrical signals and strains. This choice of connection method not only simplifies

the design but also enhances the overall precision of the measurements obtained during the characterization process. By utilizing high-quality instrumentation and innovative connection techniques, the characterization can provide deeper insights into the sensor's performance and capabilities (Figure 2.4).

Figure 2.4: Characterization of the sensor without encapsulation and cabling.

The initial baseline measurement for the sensor is established by carefully connecting the metal clips to the opposite edges of the device. This step is crucial as it provides a reference point for the sensor's performance under normal conditions. Once the baseline is recorded within a readable range, and after confirming the stability of the electrical resistance offered by the conductive paste applied to the sensor, the next phase involves creating strain to monitor any variations in the sensor's electrical properties.

To facilitate this, a precision instrument capable of applying controlled displacement to the sensor is essential. Motorized stages are typically employed for such tasks, offering a range of options tailored to meet specific requirements. Given the level of precision necessary for this experiment and the compact dimensions of the sensor, the Thorlabs MTS50-Z8 motorized stage (Thorlabs, Newton, NJ, USA), emerges as a highly suitable

choice. This particular model features a travel range of 50 mm, ensuring adequate movement capabilities while maintaining the precision required for accurate measurements.

For controlling the movement of the motorized stage, the KDC101 DC servo motor controller (Thorlabs, Newton, NJ, USA), is selected. This controller is key in managing the translation rate and providing precise adjustments to the motion, allowing for fine-tuning as the strain is applied.

To effectively position and secure the sensor onto the motorized stage, a reliable adhesive solution is necessary. In this instance, 3M 9088 (3M, Minnesota, MN, USA) double-sided tape is utilized. This tape not only ensures a strong bond between the sensor and the stage but also facilitates easy placement and removal, which is ideal for the experimental setup.

Following the initial trials, we observed promising results; however, we encountered a significant issue with microcracks that developed rapidly within the conductive paste used in the sensor. During periods when the sensor is at rest, these microcracks do not impact the sensor's functionality and result in the maintenance of the initial baseline resistance value. However, when the sensor is subjected to strain, these microcracks can lead to critical failures by causing either disconnections or an abrupt increase in resistance, which can reach high magnitudes.

To enhance the durability and longevity of the sensor, we are exploring the possibility of encapsulating the sensor while strategically leaving small areas exposed for probing. This method aims to protect the sensing elements from environmental factors and mechanical wear while still allowing for effective data collection and sensor functionality (Figure 2.5).

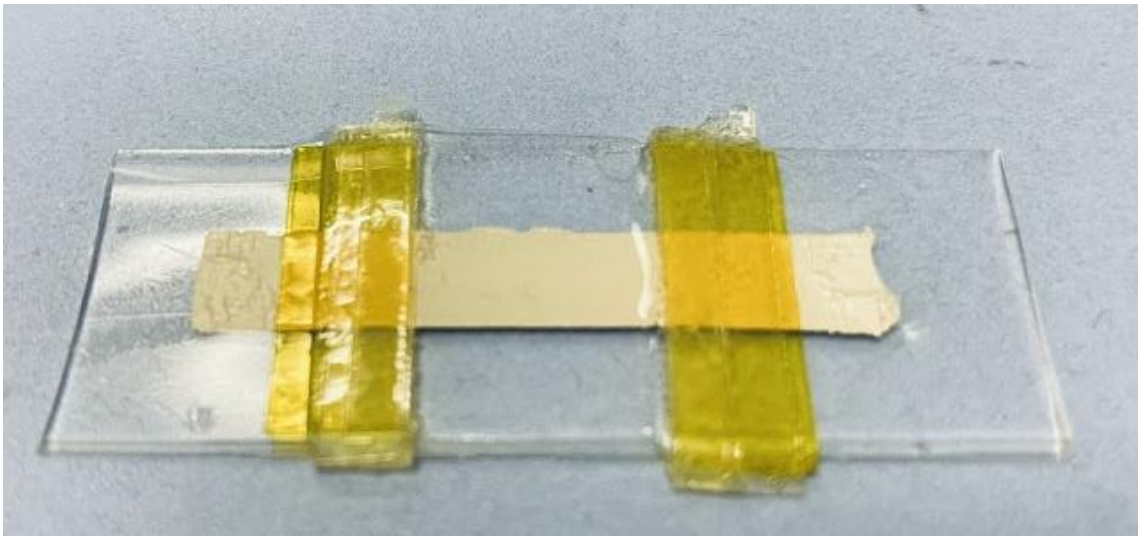

Figure 2.5: Sensor with center encapsulated and edges exposed

During the fabrication of this sensor design, a significant challenge emerged regarding the control of uncured PDMS in the center area of the sensor. To effectively address this issue, a strategy was implemented that involved applying ten layers of polyimide tape to the designated regions, thereby creating robust walls that would prevent the uncured PDMS from spilling into unwanted areas. Once these barriers were set up, the uncured PDMS was poured into the designated zone and subsequently cured, being careful not to cover the probing areas that are critical for sensor functionality.

This innovative design led to marked improvements in the overall durability of the sensor. The encapsulated region exhibited a strong resistance to the formation of microcracks. However, an unexpected downside emerged concerning the durability of the probing area itself. The probing process relies on metal clips that must apply sufficient pressure to maintain a reliable physical connection between the metal and the sensor. Unfortunately, this requirement for constant pressure, coupled with slight movements of the sensor during operation, initiated a deterioration process in this area.

After repeated cycles of strain, the continuous pressure on the conductive paste—used to ensure electrical contact—began to compromise its integrity. Over time, this led to a peeling effect where the conductive paste started to detach from the surrounding material, often resulting in disruptive outcomes such as disconnections or a dramatic increase in resistance values, tracing back to the pressurized region. This highlighted the need for further refinement in the design to enhance the longevity and reliability of the probing area while maintaining the benefits observed in the encapsulated section.

Following the analysis of the initial results, it became clear that incorporating a wiring system into the design was essential. A thorough examination of various options was conducted, comparing the benefits and drawbacks of different approaches, including conductive tape and standard wiring. After careful consideration, conductive tape was chosen as the preferred update for the design, primarily due to its ease of integration into the existing framework.

The introduction of conductive tape not only enhanced the overall design but also allowed for a more efficient flow of electrical signals. The subsequent steps involving the fabrication of the PDMS substrate film and the application of conductive paste were retained from the original protocol to ensure consistency in performance. Once the conductive paste had fully cured, the next step was to meticulously apply the conductive tape along the edges of the substrate. This application process required a precise level of applied pressure; therefore, heightened attention was given to ensuring the tape was adhered correctly to maintain optimal conductivity.

After the tape was applied, a straightforward conductance test was conducted to evaluate the functionality of the circuit. This preliminary test involved checking the signal levels to confirm that the sensor was operating as intended. Once it was established that the circuit met the necessary specifications, the sensor was prepared for encapsulation.

For the encapsulation process, a specific mixture of 2.5 grams of PDMS was prepared, using a weight ratio of 1:10 of curing agent to PDMS base. This mixture was placed in a desiccator for 15 minutes to degas and remove any trapped air bubbles, which could potentially affect the integrity of the final product. Following the degassing, the sensor was positioned on a hot plate to provide a stable and controlled environment for curing. The uncured PDMS was then carefully deposited onto the sensor using the drop-casting technique, ensuring even coverage.

The curing process was conducted at a temperature of 75 degrees Celsius for a duration of three hours, allowing the PDMS to solidify and form a protective layer around the sensor. This step was crucial for ensuring the stability and functionality of the sensor in its final application (Figure 2.6).

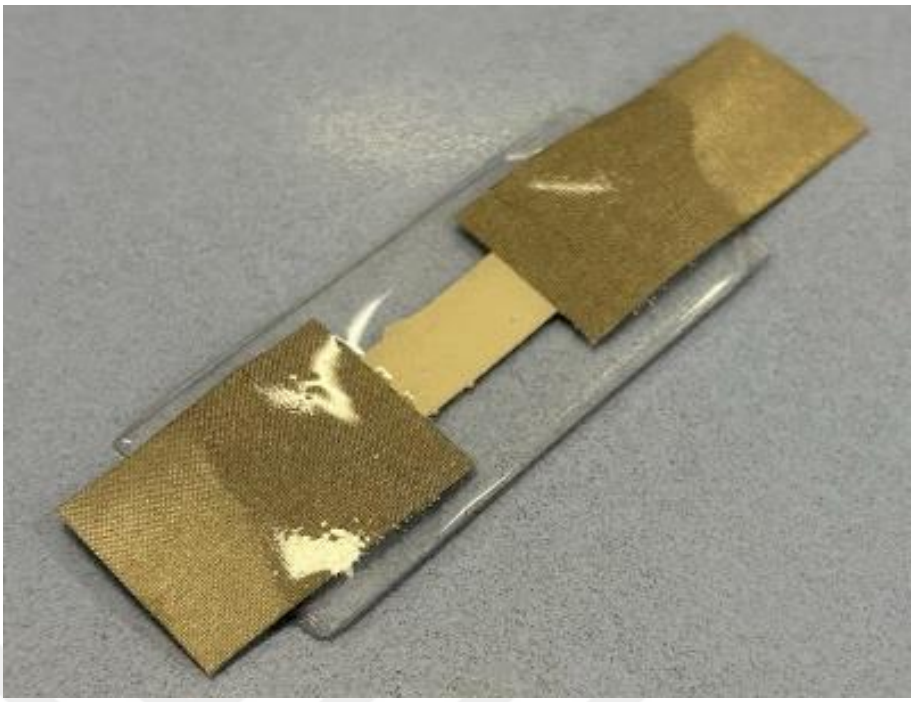

Figure 2.6: Sensor with conductive tape cabling.

The characterization of this design was conducted with the same setup used for previous designs. For this purpose, the Zurich Instruments MFIA impedance analyzer was utilized to gather electrical signals effectively. To establish a reliable physical connection with the conductive tape, metal clips were securely attached to the MFIA.

The initial phase of testing involved measuring resistance and stability under undisturbed conditions, which yielded successful results. Following this, a strain test was implemented to evaluate the sensor's response under various conditions of mechanical stress. The preliminary trials were encouraging, as they indicated the potential for the sensor to perform effectively under strain. The problem of durability, showing itself with either disconnection or extremely high instantaneous resistance values, was overcome.

However, another critical complication emerged with this design. The use of conductive tape led to the sensor output being considerably susceptible to external physical effects. The main factor contributing to variations in sensor readings was the level of pressure exerted by the metal clips. It became evident that both the alignment of the clips and the specific area where they were applied directly impacted the accuracy and reliability of the signal.

This phenomenon is not uncommon when working with conductive tape applications, highlighting a prevalent issue within this domain. Consequently, it is important to note that this type of cabling is typically employed in power line applications

rather than in sensing lines, where greater stability and precision are often required. The challenges faced with the current setup underscore the need for careful consideration of mechanical design in future iterations to enhance sensor performance.

The alternative method for cabling involves the use of standard wiring, which presents several challenges that must be addressed during the design and fabrication processes. The primary issue with standard wiring concerns the method of attachment. Soldering is widely recognized as the most common technique for securing connections in standard wiring applications. Consequently, after careful consideration, soldering was chosen as the preferred attachment method for this design.

The fabrication is repeated until the wiring step, that is, fabricating the PDMS film substrate and the patterned conductive paste. Once these components are ready, the soldering process is initiated. Usual soldering requires the solder to reach melting temperatures, which are usually above 250 degrees Celsius.

To address these temperature constraints, a technique known as “low-temperature soldering” can be employed, which reduces the necessary melting temperature to a range between 150 and 160 degrees Celsius. For our specific application, we initially opted for standard soldering practices to evaluate their effectiveness.

A critical factor in soldering onto sensitive materials like PDMS is the management of heat exposure. It is essential to minimize the duration of heat application to prevent damage to the underlying materials. With this requirement in mind, the soldering process begins by applying a small amount of solder to the edge of the wire. Since PDMS is capable of withstanding temperatures in excess of 200 degrees Celsius, it appears suitable for this situation.

Next, solder is carefully applied to the patterned conductive paste. However, a significant challenge arises during this process: as the conductive paste reaches the required temperatures for soldering, it tends to shrink excessively. This thermal reaction compromises the integrity of its patterned shape, ultimately hindering the ability to establish a reliable solder joint between the wire and the paste. As a result, despite our best efforts, the soldering process fails to achieve a secure connection, necessitating a rethink of our approach.

To ensure that all available options are thoroughly evaluated, a low-temperature soldering kit has been procured. This kit contains two distinct types of solder: one in the conventional wire form and the other in a unique wax form.

The wire solder, which adheres to the typical standards used in soldering, must be applied with a soldering tool, but at lower temperatures than traditional methods. This approach aims to minimize heat exposure while still providing a reliable connection in sensitive applications.

The wax solder offers a different method of application that does not require a soldering iron or any traditional tooling. Instead, this solder relies solely on the local temperature to reach its melting point, making the process more straightforward. Achieving the required temperature can be done using various heat sources such as an oven, a hot plate, or a heat gun.

Both solder forms were tested to allow for a comprehensive comparison of their effectiveness. However, despite these efforts, the adverse effects on the conductive paste repeat themselves. This challenge highlights the need for further investigation into the compatibility and performance of these alternative cabling methods.

Upon exploring various alternatives for wiring solutions, a noteworthy approach has been identified: the use of conductive paste for securing wires. Conductive paste is an innovative material that, once cured, exhibits both flexibility and stretchability, in addition to possessing strong adhesive properties.

The process begins with the careful application of this conductive paste to both the edge of the wire and the corresponding area of connection. This dual application ensures that there is a solid bond between the wire and the surface to which it will be attached. Following this, the wire is delicately positioned within the uncured conductive paste, taking care to maintain optimal alignment for effective conductivity.

To facilitate the curing process, both the sensor and the securely fixed wire assembly are placed on a hot plate, which is then set to a temperature of 75 degrees Celsius. This temperature is maintained for a duration of three hours, allowing the conductive paste to fully cure and create a robust electrical connection while retaining its flexible properties. This method not only enhances the stability of the connections but also contributes to the overall durability and performance of the assembled device.

Now, with the wires attached to the sensor, it is time to encapsulate it completely. To do so, 2.5 gr of PDMS with a 1:10 weight ratio is prepared and degassed. Then, the sensor is placed on a hot plate, and the uncured PDMS is drop casted. The hot plate is set to 75 degrees Celsius and kept for 3 hours. Now the sensor is ready for characterization (Figure 2.7).

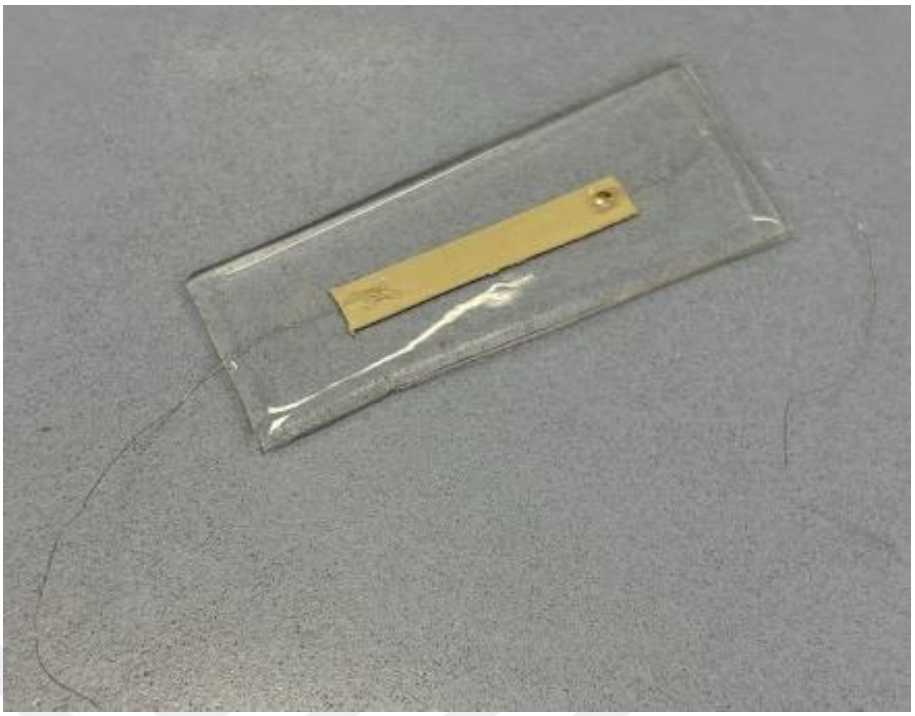

Figure 2.7: Encapsulated sensor with wirings done with conductive paste.

Characterization started with signal testing, like with the previous designs. After reaching successful results, initial strain tests were conducted, and they also met the expectations. At this stage, the problem of varying results with physical effects encountered with conductive tape paste is overcome. Also, fabrication is enabled with conductive paste, while it is not with soldering.

The process of characterization was initiated with comprehensive signal testing, following a methodology similar to that used in previous design iterations. After initial testing benchmarks were successfully achieved, preliminary strain tests were conducted, yielding results that aligned with expectations and indicating robustness in the designs.

At this stage, challenges associated with inconsistent results from the use of conductive tape paste were successfully addressed. By refining the approach, variability in performance that hindered earlier attempts was eliminated. Additionally, the transition to utilizing conductive paste enabled a more reliable fabrication process, in contrast to the limitations posed by traditional soldering methods. This advancement not only enhanced the integrity of the components but also streamlined the overall manufacturing workflow.

The stage of fabrication optimization has now been successfully completed, and the next critical phase, involving the testing of the implant application, is set to commence. A series of tests will be conducted to simulate the extreme environmental conditions and operational stresses that the sensor will endure once it is implanted on the heart. One of

the primary challenges faced is the limitless number of strain cycles that the sensor will experience within the dynamic environment of the heart's beating motion.

To address this specific requirement, a high cycle constant strain test will be performed. The Thorlabs MTS50-Z8 motorized stage (Thorlabs, Newton, NJ, USA) will be utilized for this testing procedure. This advanced motorized stage is well-suited for the purpose due to its programmable user interface, which allows for precise control over the testing parameters.

The anticipated strain levels for the sensor during its operation have been noted, with a maximum strain expected to reach 15% and an average strain level estimated at around 10%. Consequently, the initial test will be focused on applying a 10% strain level while the sensor is subjected to a high number of cycles. Valuable data regarding the sensor's durability and performance under conditions that closely mirror its expected in vivo environment will be obtained through careful monitoring and analysis of these tests. This assessment aims to provide insight into the sensor's resilience and longevity, ensuring its reliability for future implant applications.

The design featuring a single thick line and wiring has undergone durability testing. The initial results for this design are positive. The previous design, which lacked cabling, faced durability issues, but this new design demonstrates the ability to withstand numerous cycles (Figure 2.8).

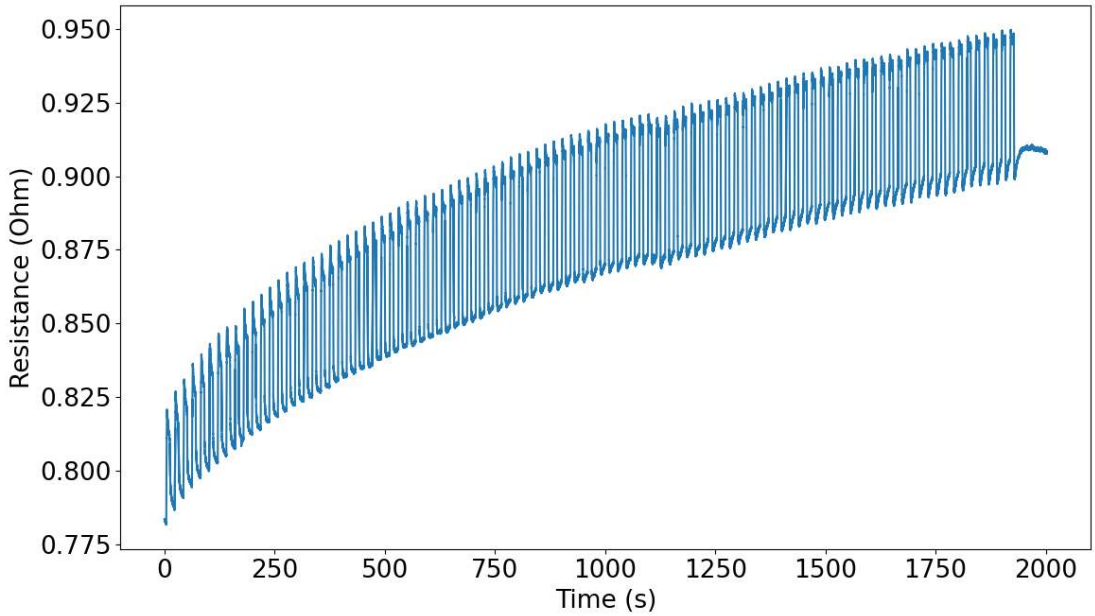

Figure 2.8: Results of first encapsulated sensor.10% cyclic strain.

From a durability standpoint, this design can be deemed successful, as there are no visible signs of physical damage, and the sensor signals remain clearly readable. Nonetheless, it is important to note that the effects of strain vary with each cycle of use. A notable observation is the consistent increase in resistance that occurs with every cycle, indicating a response of the sensor to the applied strain.

Interestingly, despite maintaining a constant strain level throughout the duration of the experiment, two unexpected phenomena have emerged. Firstly, the baseline resistance of the sensor exhibits a gradual increase after each cycle, suggesting a potential change in the material properties or structure of the sensor itself over time. Secondly, there is a noticeable enhancement in the resistance changes corresponding to a consistent application of 10% strain, which intensifies in each successive cycle. This indicates that the sensor's responsiveness to the applied strain is not only consistent but also amplifies with repeated applications, warranting further investigation into the underlying mechanisms responsible for these changes.

To address this issue, a geometric update is proposed to enhance the base resistance value, thereby amplifying the sensor's response to geometric changes. This update involves reducing the cross-sectional area and increasing the length of the sensor, which leads to a higher baseline resistance. As anticipated, this design positively impacted the results (Figure 2.9).

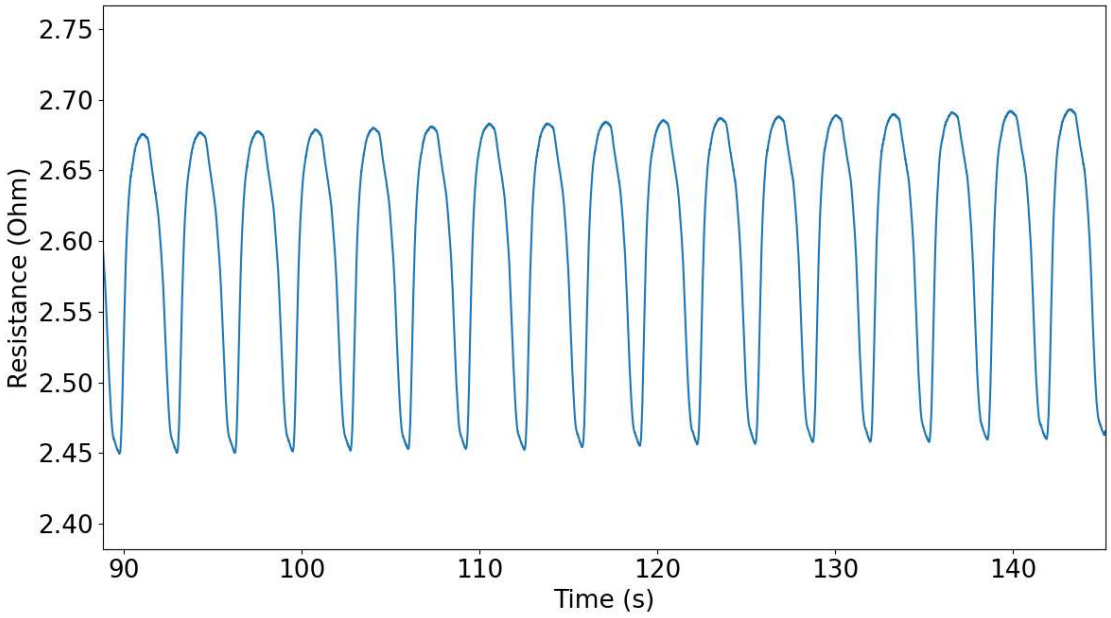

Figure 2.9: Initial results of the long-narrow sensor. 5% cyclic strain.

However, an additional challenge arises with the implementation of the new design. During long-term cyclic strain testing of the sensor, it becomes apparent that extreme peaks begin to occur as the number of cycles increases. This phenomenon suggests the presence of a defect that disrupts the integrity of the connections within the sensor. As the test progresses, these peaks indicate a progressive degradation, likely resulting from fatigue or material failures that compromise the sensor's performance. This issue warrants further investigation to identify the root cause and mitigate the risks associated with prolonged use under cyclic loading conditions. (Figure 2.10)

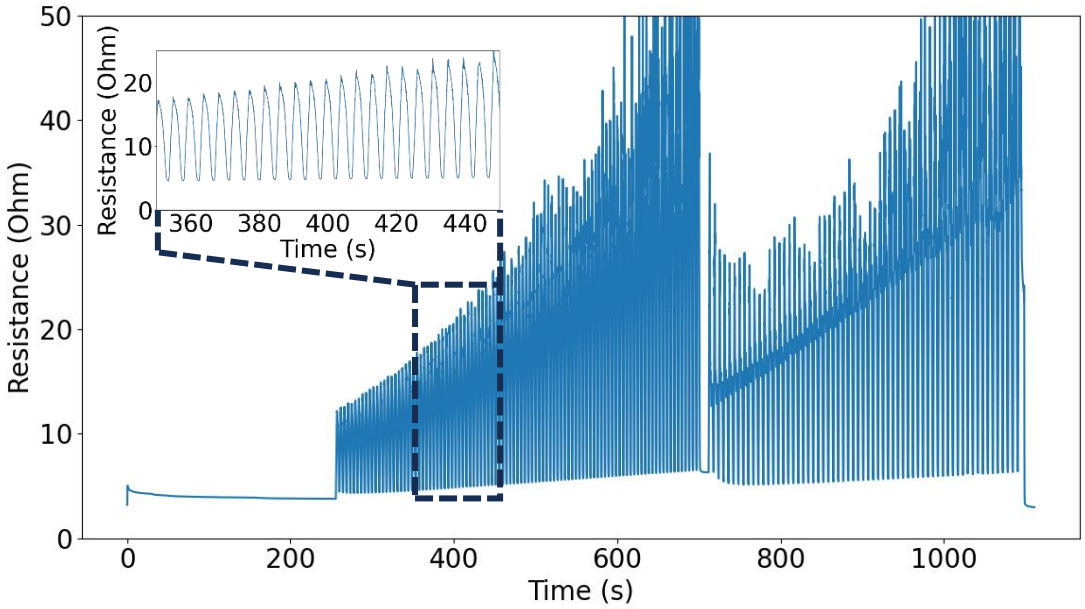

Figure 2.10: Results of the long-narrow sensor. 5% cyclic strain.

To address the identified issue, the thickness of the line has been selected as a critical parameter for observation. As a result, three distinct alternatives have been designed and fabricated, each featuring a pair of legs that are connected to enhance the overall resistance. The alternatives have varying leg thicknesses, specifically 2 mm, 3 mm, and 4 mm. These variations are illustrated in the accompanying figure (Figure 2.11), which highlights the differences in design and structure. This approach allows for a comprehensive evaluation of the effects of varying leg thickness on performance and resistance.

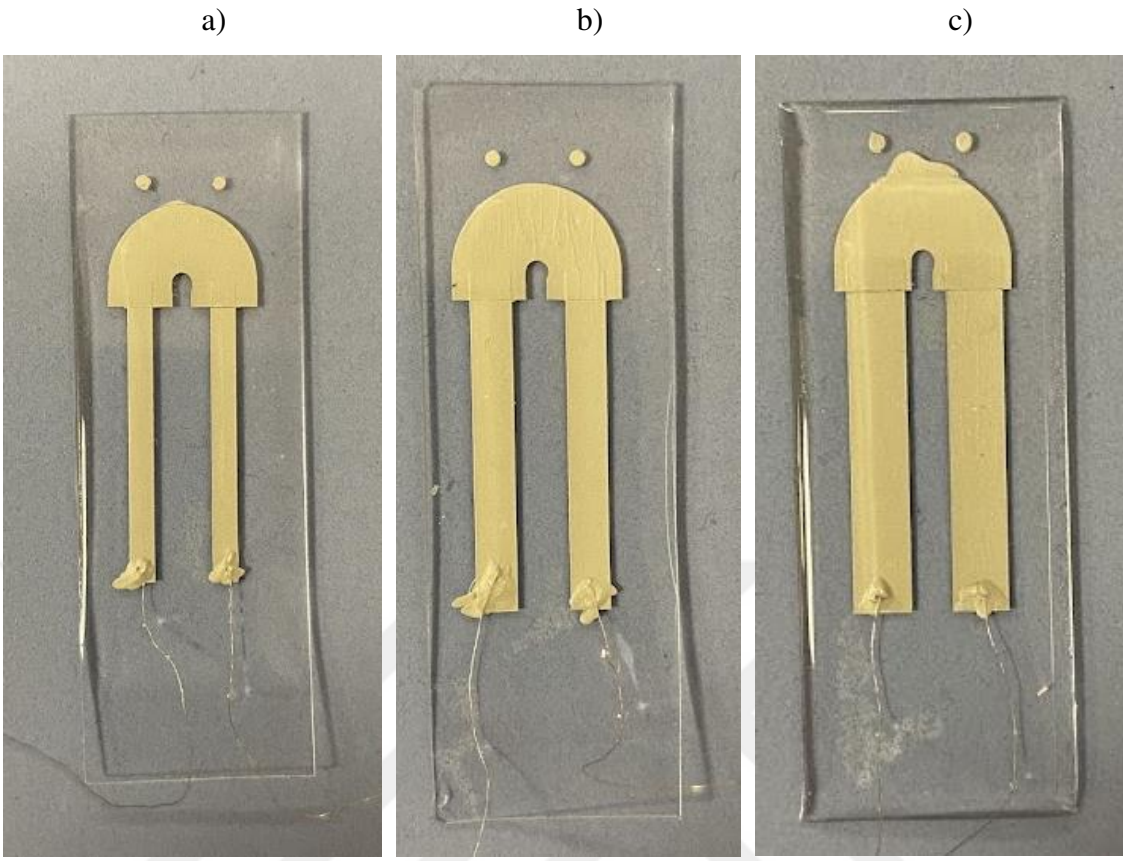

Figure 2.11: Parametric experiment samples to study effect of leg thickness. a) 2 mm, b) 3 mm, c) 4mm thick.

The three designs showed different resistance values and reacted differently when strain was applied. Each design had its own unique way of changing resistance under stress. However, they all had a common problem: their resistance patterns were unstable. This instability makes it difficult to create a reliable calibration curve, which is needed for accurate measurements. As a result, it becomes hard to take precise measurements since the inconsistency in resistance values interferes with getting clear and accurate data. (Figure 2.12)

a)

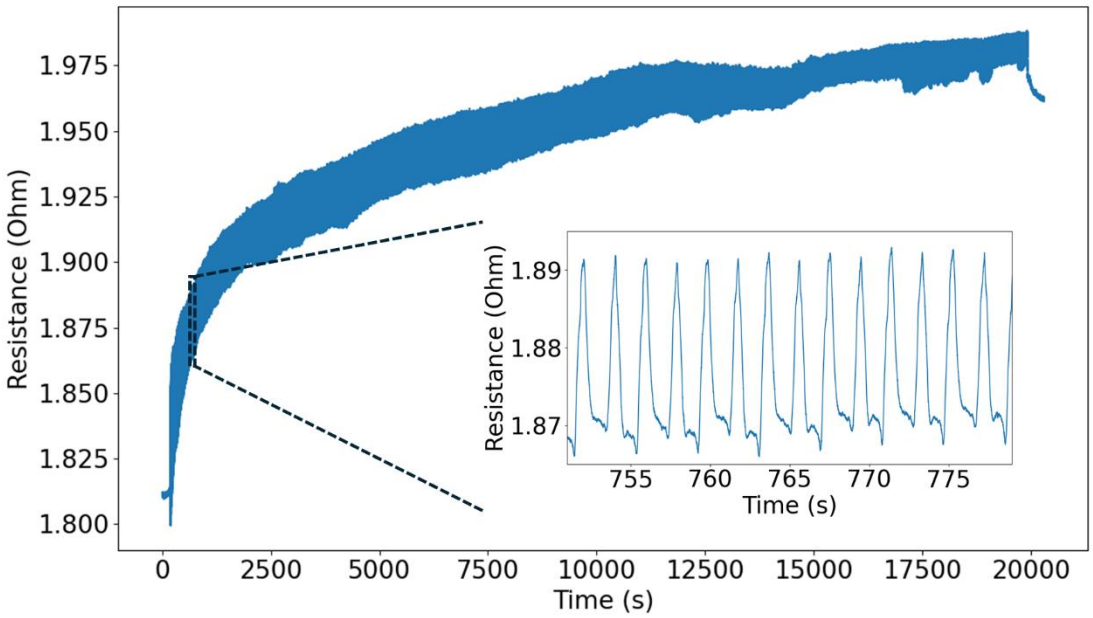
Resistance (Ohm)
1.975
1.950
1.925
1.900
1.875
1.850
1.825
1.800
0
2500
5000
7500
10000
12500
15000
17500
20000
Time (s)
Resistance (Ohm)
1.89
1.88
1.87
755
760
765
770
775
Time (s)

b)

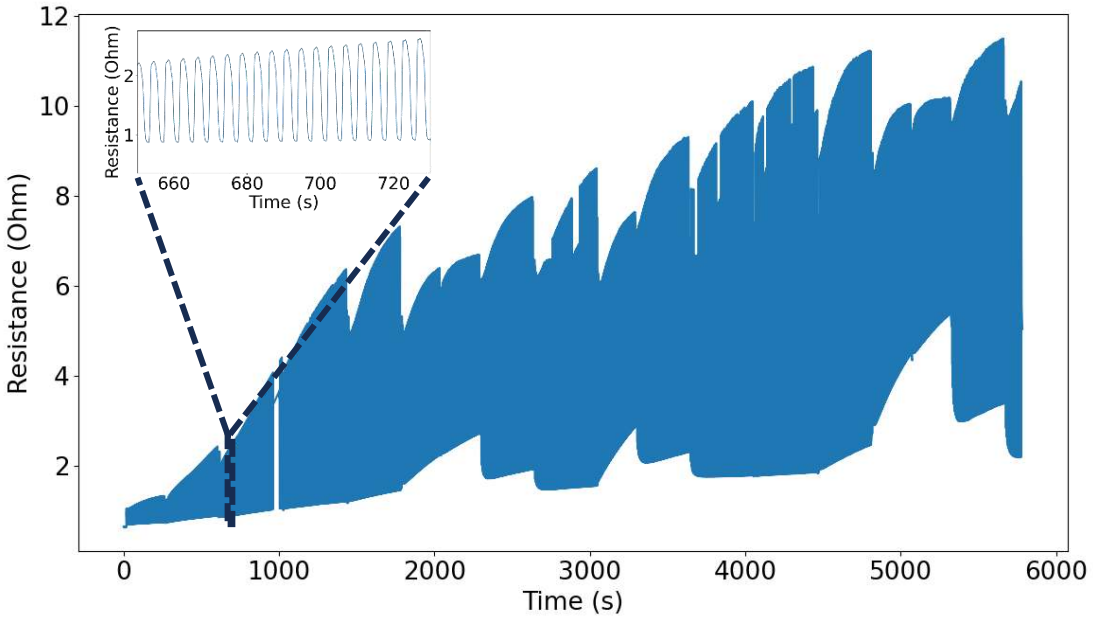
Resistance (Ohm)
12
10
8
6
4
2
0
1000
2000
3000
4000
5000
6000
Time (s)
Resistance (Ohm)
2
1
660
680
700
720
Time (s)

c)

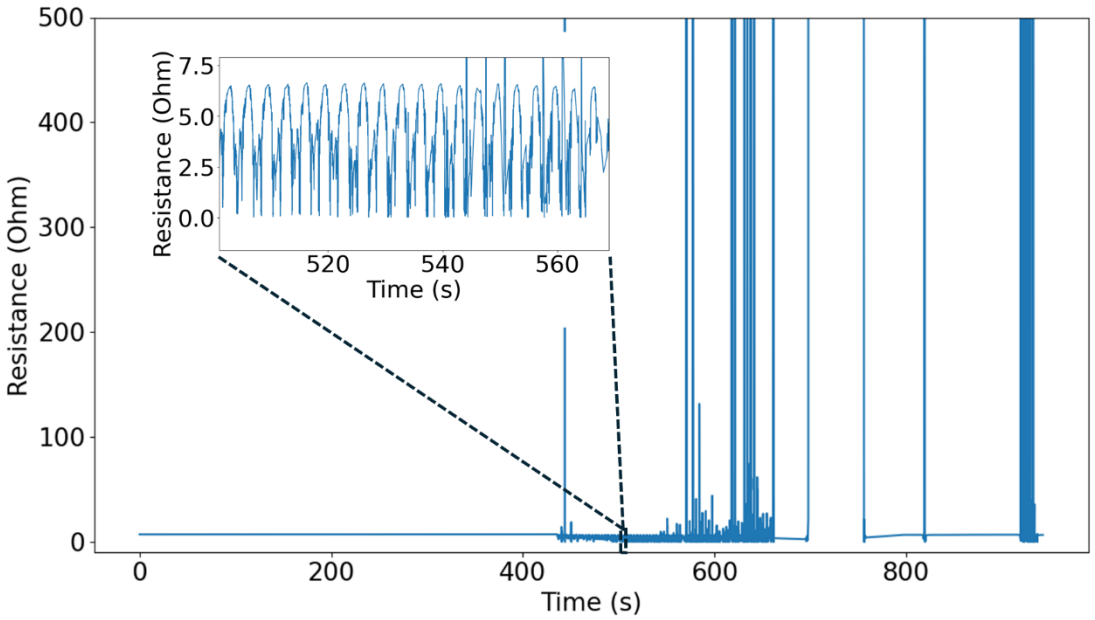

Figure 2.12: Line thickness optimization results. a) 4 mm wide sensor under 5000 cycles of 5% strain, b) 3mm wide sensor under a patterned cycle of 5, 10, 15, 15, 10, 5% strain, c) 2mm wide sensor under 5% cyclic strain.

The parametric study resulted in unstable patterns, which necessitated a geometric update. To further improve performance, a more advanced pattern was designed. This pattern features more arms to increase the change in resistance and, consequently, sensitivity. (Figure 2.13)

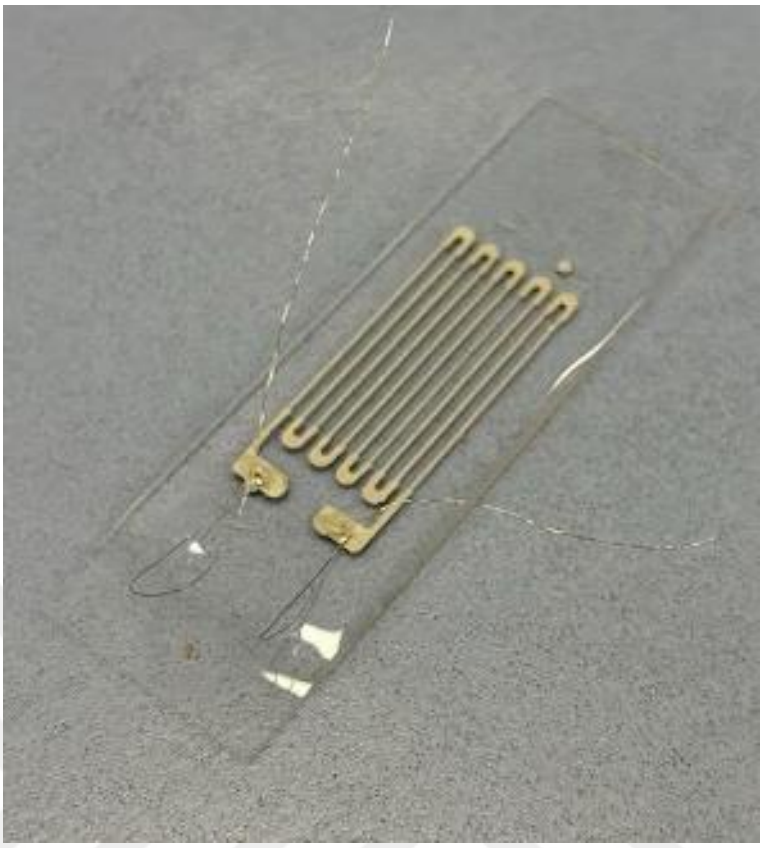

Figure 2.13: Improved pattern for stable measurement.

The design implemented in our study resulted in reliable and stable measurements during the initial phases, specifically throughout the first few hundred cycles. This stability was considered crucial for ensuring the accuracy of the data. However, as more cycles were conducted, unexpected peaks in the readings were observed. These anomalies led to fluctuations and introduced significant instability in the measurements. Consequently, the reliability of sensitive measurements was compromised, prompting a reassessment of the methodology to address these challenges. (Figure 2.14)

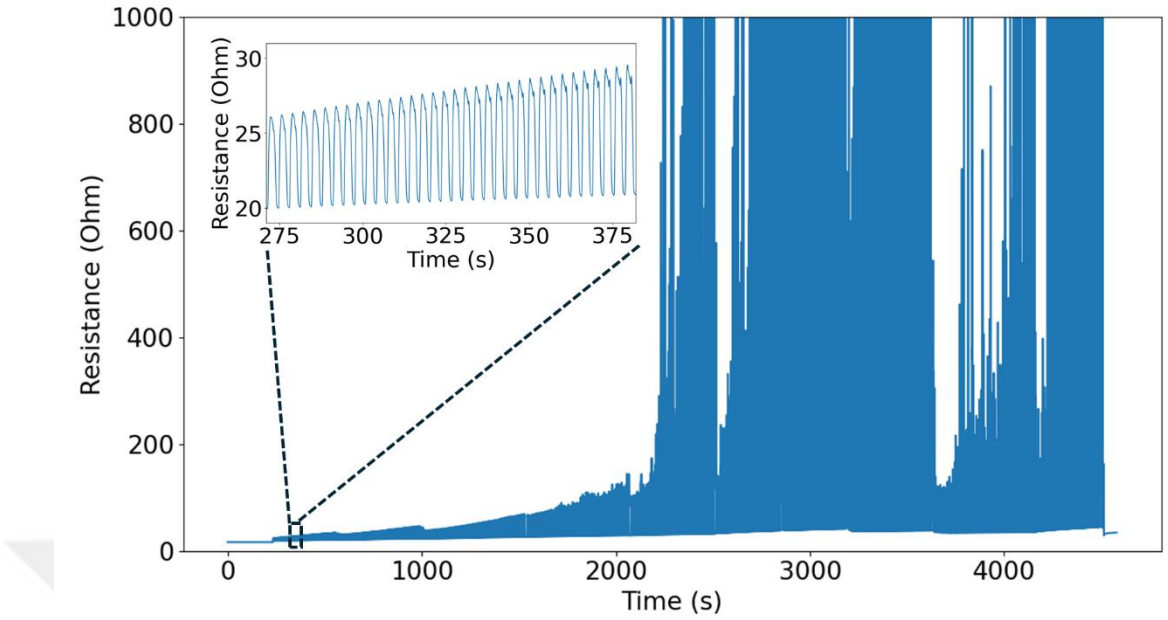

Figure 2.14: Advanced pattern results. 10% cyclic strain.

At this stage, a specific physical phenomenon is being investigated that appears to consistently impact the sensor's performance alongside each design enhancement implemented. This occurrence is believed to be linked to the formation of microcracks within the sensing layer, particularly in the conductive paste employed in the sensor. Such microcracks have been documented in various studies found in the literature, especially in similar applications, indicating that this issue is not unique to our design but rather a widespread challenge in the field. Further exploration into the underlying mechanisms responsible for the formation of these microcracks is expected to yield valuable insights that could improve sensor reliability and performance.

Chapter 3: **DESIGN, FABRICATION AND CHARACTERIZATION OF CAPACITIVE STRAIN SENSOR**

3.1 Design

Resistive strain sensors offer notable advantages such as straightforward fabrication processes and minimal electronic requirements for effective characterization. These benefits, however, are present with inherent challenges related to their material properties. Specifically, the soft and flexible nature of these sensors poses a significant dilemma that can compromise their operational efficacy.

To elaborate, resistive strain sensors operate on the principle that a change in length or shape corresponds to a measurable variation in electrical resistance. This mechanism is particularly effective under low strain conditions, as demonstrated in steel tensile tests. In such scenarios, the formation of microcracks within the sensing material often remains insignificant to the accuracy of the readout. The system is capable of absorbing these small imperfections without significant degradation of performance.

Conversely, when applying these sensors in applications requiring flexibility and durability, particularly under conditions of repeated stress cycling—such as operating at a frequency of 1 Hz with a strain amplitude of 10%—the situation becomes more problematic. The mechanical demands placed on the sensor can lead to the development of microcracks that multiply over time. Such structural compromises hinder the sensor's ability to provide reliable readouts, as the consistent formation of microcracks disrupts the electrical integrity and responsiveness of the sensing element. Thus, while resistive strain sensors exhibit beneficial traits, their performance can be severely limited in flexible applications subjected to dynamic strain conditions.

A capacitive strain sensor operates based on the variations in the characteristics of an interdigitated capacitor, which is a specialized type of capacitor designed for enhanced sensitivity and performance. To understand how these sensors function, it's essential to explore the fundamental differences between interdigitated capacitors and the more commonly recognized parallel-plate capacitors.

In parallel-plate capacitors, the capacitance (C) is determined using the equation (3.1), where:

$$C = k\frac{A}{d} \tag{3.1}$$

-C represents the capacitance,

-k is the relative permittivity of the dielectric material positioned between the plates,

-A denotes the effective conducting area of the plates, and

-d signifies the separation distance between the plates.

Interdigitated capacitors consist of multiple conductive "fingers" that are interleaved, resembling a comb-like structure. This unique configuration creates a significantly different electrical behavior compared to standard parallel-plate capacitors. Each finger pair acts as a miniaturized capacitor, allowing for greater interaction between the plates.

The formula for capacitance in interdigitated capacitors is an extension of that for parallel plates. Because there are two-way interactions for each conductive finger, the capacitance calculation must be multiplied by a factor of 2. Moreover, the repeating pattern of finger pairs necessitates multiplying this adjusted value by the total number of finger couples present in the design. This results in a more complex and effective arrangement that allows for greater sensitivity to strain, as even minor changes in distance or area can result in measurable shifts in capacitance (Figure 3.1).

Overall, the design of interdigitated capacitors makes them particularly advantageous for applications involving capacitive strain sensing, as they can effectively detect even small deformations by monitoring changes in capacitance due to their intricate structure.

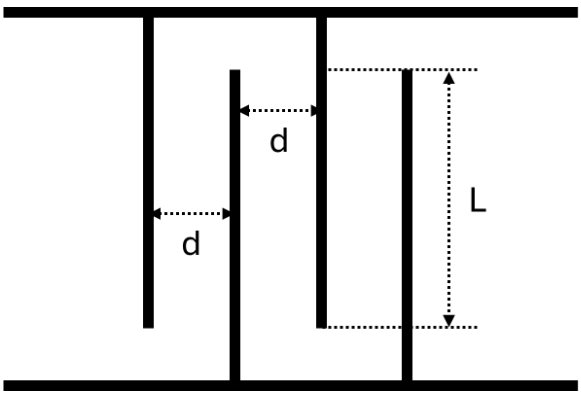

$$Conducting\ Area = L * Thickness$$

Figure 3.1: Illustration of an interdigitated capacitor structure.

The current design has been influenced by several limitations. The parameters to be selected include capacitance upper and lower limits, sensor thickness, sensor area, and the medium in which the sensor will be encapsulated.

The limits for capacitance measurement, both upper and lower, are determined by the specifications of the characterization device utilized in this project. The FDC 1004 Analog-To-Digital Converter (ADC) integrated circuit from Texas Instruments (Texas Instruments, Dallas, TX, USA) has been selected for this purpose. This microchip is designed as a high-resolution, 4-channel capacitance-to-digital converter, specifically intended for capacitive sensing applications (Figure 3.2).

Capacitance can be measured by the ADC within a range of 0 to 15 picofarads (pF), with a measurement resolution of 0.0005 pF. Such a fine resolution allows for the accurate capture of even the smallest variations in capacitance, making it highly suitable for the design objectives. However, while the design will primarily operate within this specified capacitance range, additional factors influencing the overall measurement must also be accounted for.

In particular, the contributions from sensor wiring, external circuitry, and various environmental influences that may lead to an increase in overall capacitance should be considered. These external factors can include temperature fluctuations, humidity, and the presence of nearby conductive materials. To ensure reliable performance and accurate readings, a margin accommodating the capacitance effects introduced by these external influences must be incorporated into the design. By planning for this additional capacitance, the robustness of the system can be enhanced, maintaining measurement integrity within the intended operational range.

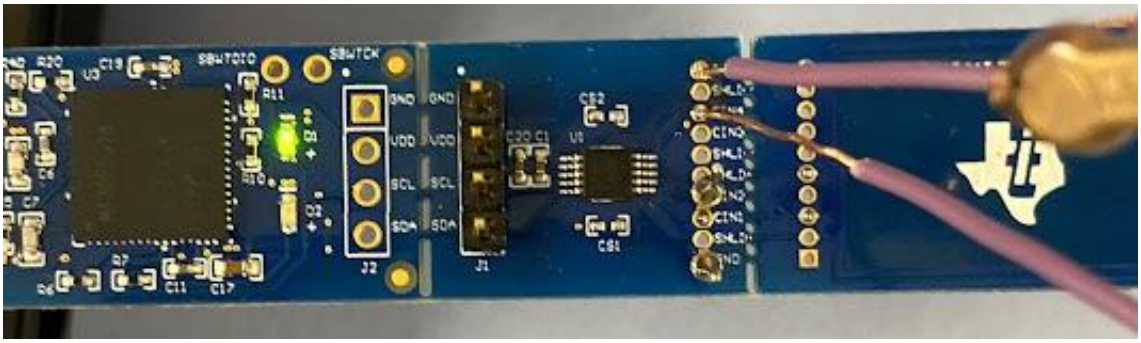

Figure 3.2: Texas Instruments FDC 1004 ADC evaluation module.

When designing a sensor intended for implantation in the human heart, numerous critical design choices must be made to ensure both functionality and biocompatibility. One of the essential considerations is the choice of encapsulation material that will protect the sensor from the physiological environment while also being safe for long-term contact

with biological tissues. In this case, PDMS has been selected as the encapsulation material due to its favorable properties.

PDMS is widely recognized for its biocompatibility, meaning it does not elicit harmful immune responses when in contact with body tissues. Its soft and flexible nature allows for ease of integration with the surrounding heart tissue, minimizing discomfort and potential damage during and after the implantation process. Moreover, PDMS exhibits excellent durability, which is critical in ensuring the long-term performance of the sensor within the dynamic environment of the heart. These attributes make PDMS an optimal choice for this application, ensuring the sensor remains functional and safe over time.

Additionally, this implant needs to be compact in design to ensure it does not interfere with the heart's natural movements. The selected maximum dimensions for the implant are 2 square centimeters, which translates to a rectangular shape with side lengths of 2 centimeters and 1 centimeter. This size limitation is crucial to maintain proper cardiac function and to allow the heart to operate efficiently without any obstruction or disruption caused by the presence of the implant.

Copper with a thickness of 25 µm was chosen for the sensing element, striking a balance between conductivity and mechanical stability. The layout of the sensor features 8 pairs of interdigitated fingers, which are strategically arranged with a separation of 0.1 mm between each finger. This close spacing is considered crucial for optimizing the capacitive coupling between the finger pairs.

To enhance performance and reliability, a pattern overlap of 2.3 mm is incorporated into the design, facilitating improved electrical contact and signal quality. Additionally, a serpentine-structured pattern is integrated to interconnect the finger pairs. This innovative approach ensures reliable connections and imparts structural stretchability to the copper, allowing the sensor to maintain functionality under mechanical strain.

Overall, this design aims to leverage the unique properties of the chosen materials and configurations to achieve a highly responsive and durable capacitive sensor (Figure 3.3).

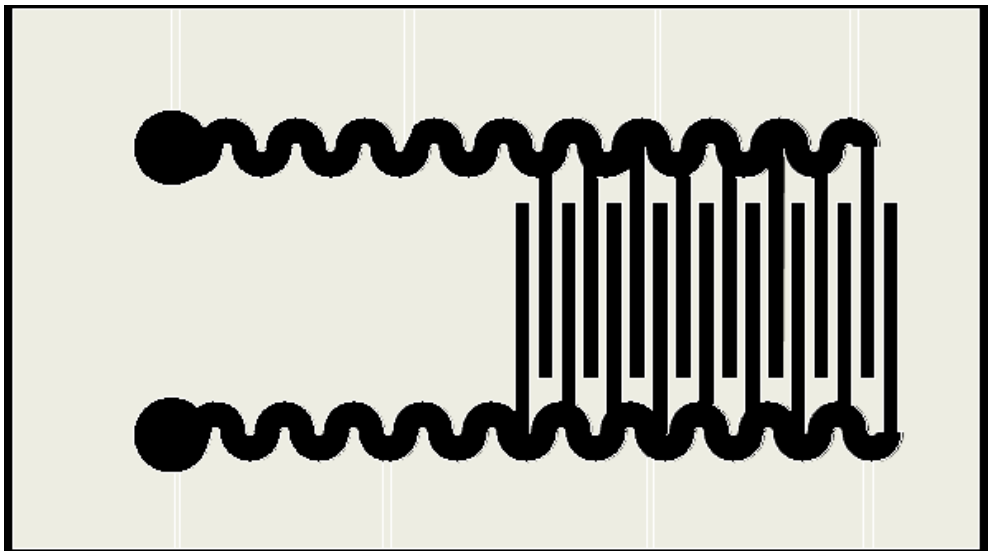

Figure 3.3: Illustration of the interdigitated capacitive sensor design.

The analytical formulation used to analyze the selected design is expressed in Equation 3.2. In this equation, C represents the capacitance of the system, while N denotes the total number of finger couples integrated into the design. The variable ϵ signifies the relative permittivity of the dielectric material used, in this case, PDMS, which has a value of 2.8 where vacuum permittivity is 0.00854 pF/mm. Additionally, t indicates the thickness of the conductive material, which in this design is copper with a thickness of 0.025 mm.

$$C = 2\frac{N\epsilon tl}{d} \tag{3.2}$$

The length of overlap between the finger couples is represented by the variable l, which is measured to be 2.3 mm, and d denotes the distance between adjacent fingers, set at 0.1 mm in the relaxed state of the sensor. The current design incorporates a total of 8 finger couples, contributing to its overall performance.

When these parameters are utilized in the capacitance calculation, they yield a nominal capacitance value of 0.22808 pF. Moreover, the sensor exhibits sensitivity to applied strains; specifically, strains of 5%, 10%, and 15% correspond to changes in capacitance of 10 fF, 20 fF, and 30 fF, respectively. These changes reflect the sensor's ability to respond to mechanical deformations, making it a valuable component for applications requiring precise measurements of strain.

3.1.1 Modelling And Simulation of the Implantable Capacitive Soft Strain Sensor

Modeling and simulation of capacitive soft strain sensors play a crucial role in predicting the sensor's performance across a range of strain conditions. This predictive capability is invaluable, as it enables engineers and researchers to optimize the sensor's design prior to the actual fabrication process. By simulating various scenarios, one can gain insights into both the mechanical and electrical behavior of the sensor, which is key to refining its overall performance.

Through detailed simulations, it becomes possible to explore the intricate multiphysics interactions at play within the sensor. This includes understanding how mechanical deformation impacts the capacitive readings, as well as how different materials and geometries influence the sensor's sensitivity and accuracy. Furthermore, these modeling techniques can pinpoint potential failure points within the sensor design, allowing for early intervention in the design process to mitigate risks associated with mechanical stress or material fatigue.

The ability to forecast the response of these sensors under different operating conditions also assists in making informed material choices. Selecting the appropriate materials based on their mechanical properties and compatibility with the intended application can significantly enhance the sensor's reliability and effectiveness. This is particularly important for implantable applications, where long-term stability and performance are critical for achieving successful integration into the human body. Overall, sophisticated modeling and simulation not only advance the understanding of capacitive soft strain sensors but also play a pivotal role in ensuring their robustness and performance in practical applications.

Comprehensive explanation of the analytical model of the sensor was provided in the design section. This model is founded on the principles of the parallel plate theorem, which allows for the simplification of calculations related to the sensor's performance. The section details the key geometrical parameters that influence the model, including the dimensions of the plates, the distance between them, and the material properties involved. These parameters are crucial for understanding how the sensor operates and how its performance can be optimized in various applications.

A series of multiphysics finite element analysis (FEA) simulations were performed to rigorously validate the theoretical model, employing a widely-used commercial FEA

software suite (COMSOL Multiphysics 5.6, COMSOL AB, Sweden). The methodology employed for these uncoupled multiphysics simulations is meticulously outlined below.

Initially, mechanically deformed geometries were generated as part of a comprehensive parametric study. This study involved creating models that experienced different levels of strain—specifically, 5%, 10%, and 15%—to analyze how varying degrees of deformation affected the subsequent electromagnetic properties. Once the strain-induced models were established, they were prepared for in-depth electromagnetic analysis.

In the final phase of the simulation, an electric potential of 2.25 volts was applied across the electrodes of the system. This setup aimed to investigate the resulting electrostatic behavior. To quantify the system's response, the capacitance was calculated by evaluating the electrostatic energy stored within the components in conjunction with the applied potential. This approach not only facilitated a detailed understanding of the electromagnetic interactions but also provided insights into the behavior of the deformed geometries under specified electrical conditions (Figure 3.4).

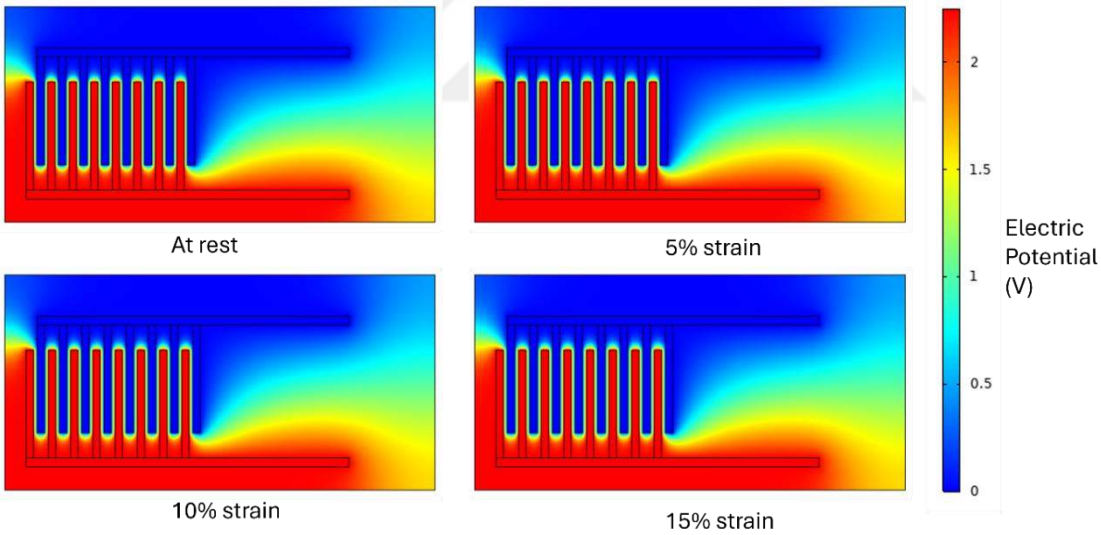

Figure 3.4: FEA simulation results for different strain levels.

3.2 Fabrication

The process of fabricating a capacitive strain sensor using an interdigitated design demands attention to detail, as uniformity in the spacing of the fingers is crucial for optimal sensor performance. Each finger's distance must be precisely controlled, and the overall pattern must yield closely to theoretical specifications to ensure the intended functionality.

To successfully create this sensor with soft materials like PDMS, it is essential to incorporate a rigid supporting layer. For this purpose, a glass slide has been chosen as the foundational substrate. This bottom layer will support the soft material during the initial fabrication process and will ultimately be removed to allow for the desired flexibility and responsiveness of the sensor.

The fabrication flow begins with preparing the PDMS substrate. In this step, a specific mixing ratio of curing agent to PDMS base of 1:10 is carefully measured and combined. This mixture is then thoroughly stirred to ensure a homogenous blend, which is vital for achieving consistent curing properties. The combined materials are poured onto the glass slide, forming a film that is cured at elevated temperatures to obtain a final thickness of 100 µm.

For a more efficient approach, utilizing commercially available PDMS sheets presents an alternative method to create the necessary film, bypassing the in-house preparation process. This option can significantly streamline production while still ensuring the desired material characteristics for the capacitive strain sensor.

Followingly, a polyimide-copper foil (Pyralux AP Series, DuPont, USA) is carefully positioned on top of the PDMS film substrate. This specific foil is a commercially available product that consists of a composite structure: a 25 µm layer of polyimide is laminated with a 25 µm layer of copper, resulting in a total thickness of 50 µm. The next step involves precise patterning of the metal foil using a high-resolution picosecond laser (LPKF ProtoLaser R4, LPKF Laser & Electronics AG, Garbsen, Germany).

To achieve successful patterning, an exact recipe of laser parameters must be delicately prepared. The laser operates with a frequency setting of 300 kHz, delivering a power level of 7.3 W. The speed at which the laser marks the material is set to 300 mm/s, and this procedure is performed with eight repetitions to ensure an accurate and clean cut through the foil.

Once the laser ablation process is completed, any excess portions of the foil, which are not part of the intended design, are carefully removed. This delicate removal process ensures that the final pattern retains its integrity and precision, resulting in a clean and accurate metal pattern on the PDMS film substrate.

Following the initial fabrication steps, the next crucial phase involves cabling the sensor components. Unlike the process used for resistive strain sensors, which typically necessitates alternative joining methods, soldering can be utilized here. This is feasible

because metal foil can tolerate brief episodes of elevated temperatures, just long enough for applying small amounts of solder without compromising the material.

Once the cabling is thoroughly completed, attention turns to encapsulation, specifically with regards to preparing the PDMS. To achieve the proper consistency and performance characteristics, a mixture comprising a curing agent and PDMS base is prepared at a weight ratio of 1:10. Before proceeding with the application, it is essential to eliminate any air bubbles from the mixture to ensure a flawless final product. This is accomplished by placing the mixed compound in a vacuum chamber, where it undergoes a degassing process.

After degassing, the PDMS mixture is carefully drop cast onto the sensor surface. It's important to distribute the mixture evenly to ensure comprehensive coverage and optimal encapsulation. Following the application, the sensor is then placed on a hot plate, where it remains for a designated period of three hours at a consistent temperature of 80° Celsius. This curing process solidifies the PDMS, providing enhanced protection and ensuring the integrity of the sensor.

Once the curing time has elapsed, the sensor is delicately removed from the glass slide, and it is now fully prepared and ready for operational use. The careful attention to detail throughout these steps is critical in achieving a high-quality and reliable sensor (Figure 3.5).

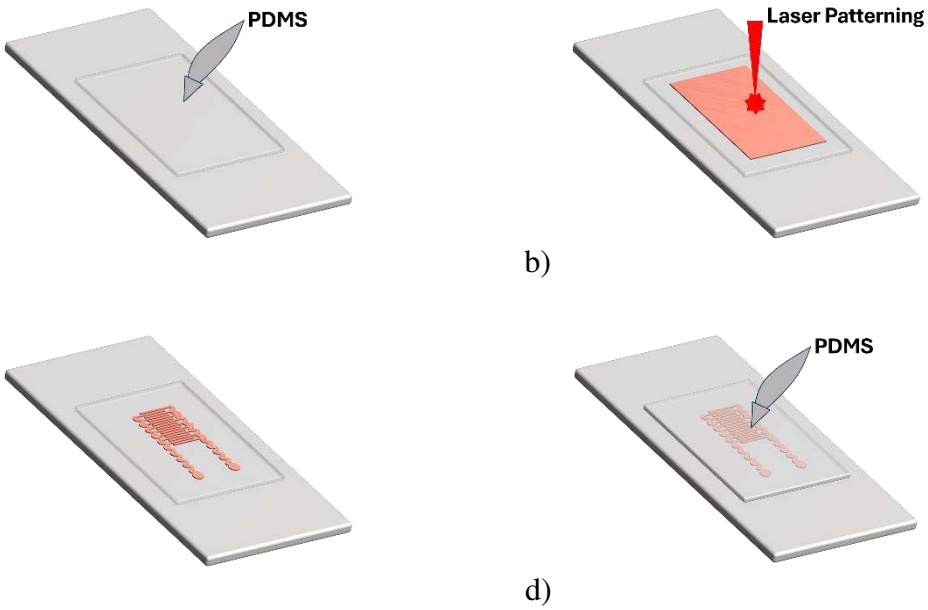

a) b)

c) d)

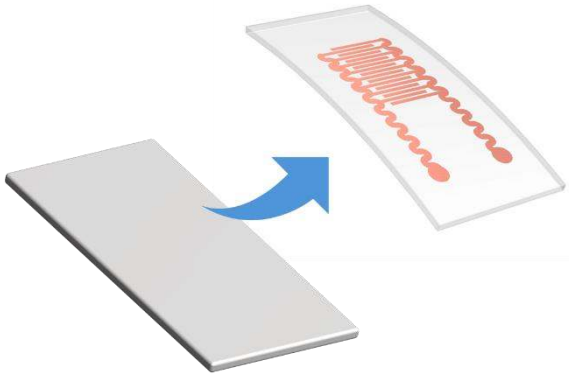

e)

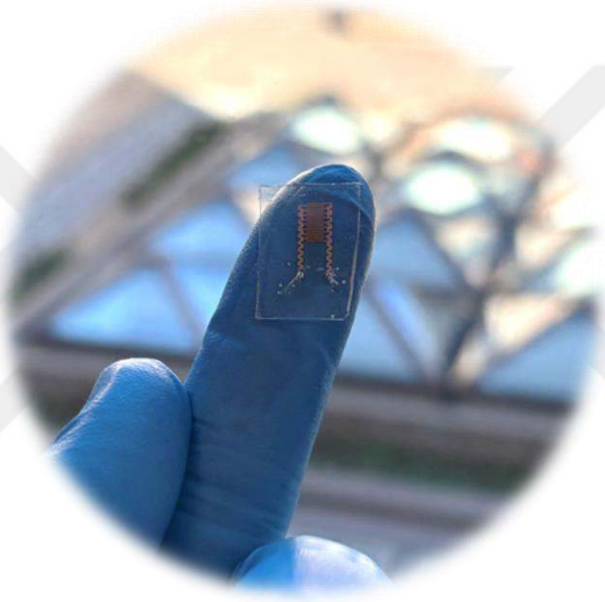

f)

Figure 3.5: Fabrication flow of capacitive strain sensor. a) PDMS substrate developed on the glass slide rigid layer. b) Commercially available polyimide-copper foil is patterned with LPKF ProtoLaser R4. c) Excess portions of the foil are removed. d) The sensor is encapsulated with PDMS. e) The completed sensor is delicately removed from the glass slide. f)Fabricated sensor.

3.3 Characterization

To effectively characterize the sensor, a precision moving stage is required to induce strain, along with an electrical measurement device to monitor the capacitance changes resulting from this strain. In this research, the Thorlabs MTS50-Z8 (Thorlabs, Newton, NJ, USA) has been selected as the precision moving stage, recognized for its high accuracy and reliability. This stage will allow for the application of controlled and precise movements to the sensor, facilitating accurate strain induction. Additionally, the Linkam MFS (Linkam MFS 350, UK) has been chosen as a complementary moving stage, known for its force sensing capabilities and extremely sensitive positioning.

For the electrical measurements, the Zurich Instruments MFIA (Zurich Instruments AG, Zürich, Switzerland) has been selected, providing advanced measurement capabilities with high sensitivity, which makes it ideal for monitoring small capacitance variations. Furthermore, a data acquisition system from Texas Instruments, specifically FDC1004EVM (Texas Instruments, Dallas, TX, USA), is being utilized, offering robust signal processing features necessary for experimental analysis (Figure 3.6).

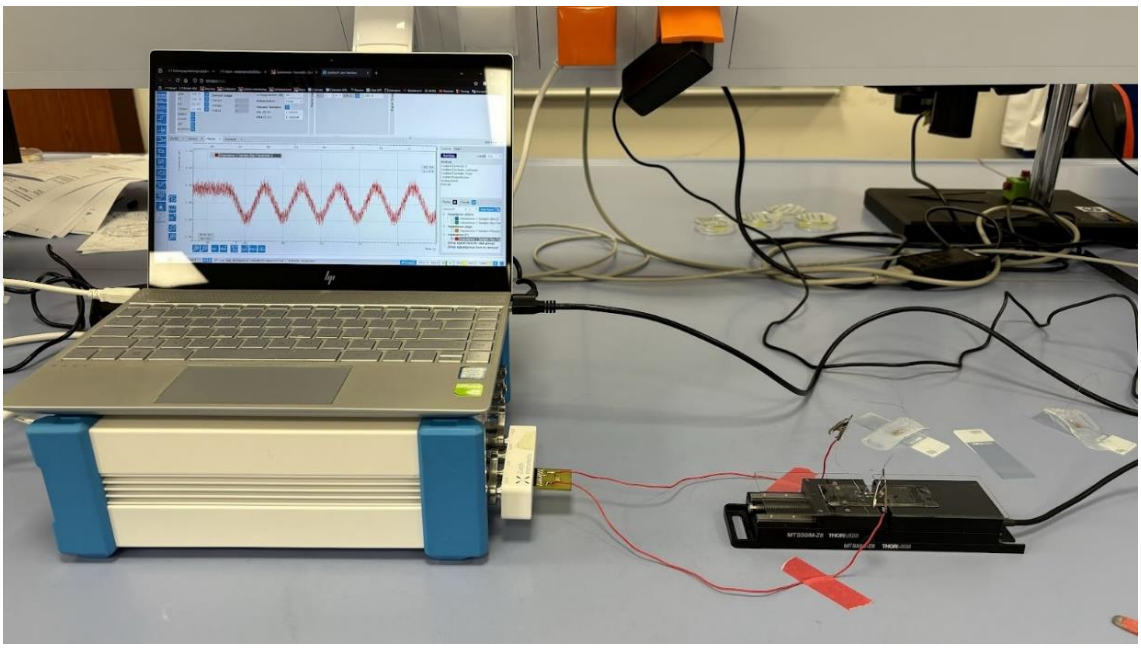

Figure 3.6: The characterization setup with Thorlabs moving stage and Zurich Instreuments MFIA.

The primary evaluation criterion for the implant application of the capacitive soft strain sensor is the stability and durability demonstrated under continuous operation over extended periods. To assess this, a rigorous 12-hour cyclic test was conducted to simulate real-world operating conditions. Throughout the test, remarkably stable performance was exhibited by the sensor, with consistent signal integrity maintained under the applied strain. However, it was noted that the only disruption observed in the signal was attributed to the gradual loss of adhesive properties in the double-sided transfer tape used for attachment during the testing process (Figure 3.7).

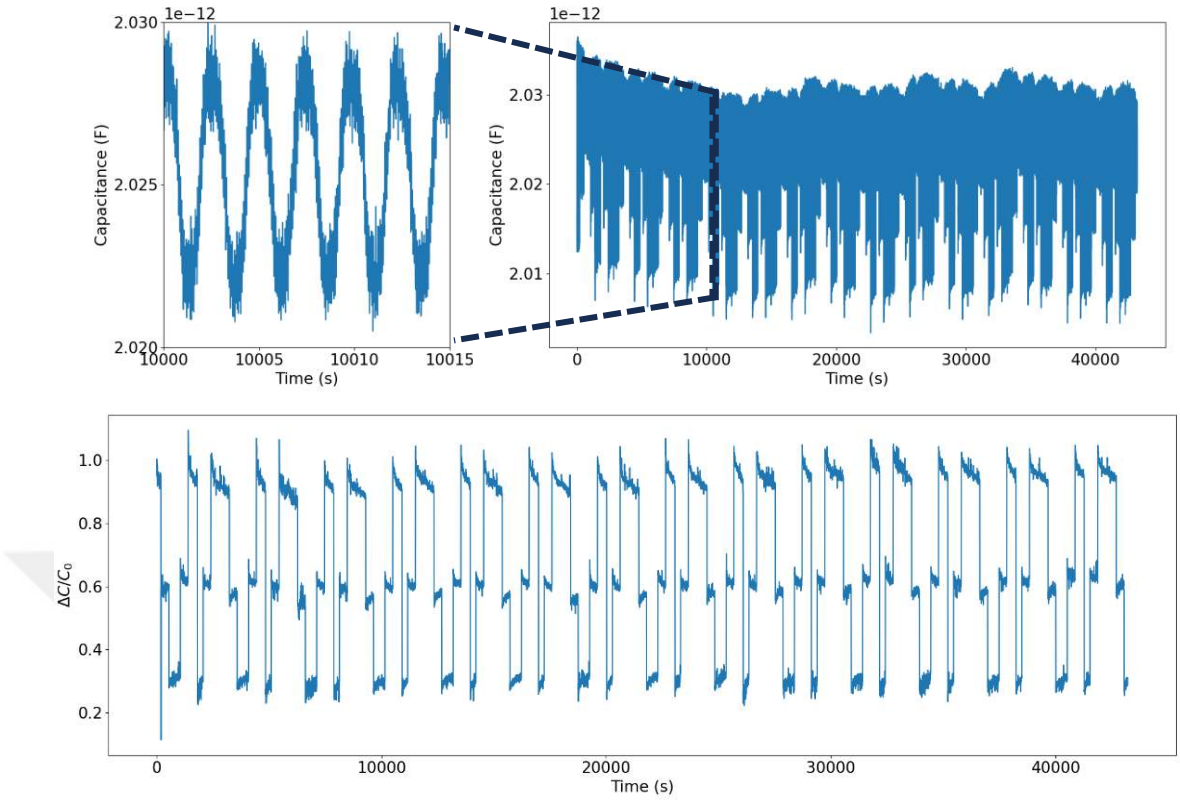

Figure 3.7: Capacitive sensor 12-hour cyclic measurement. Patterned cycle of 5, 10, 15, 15, 10, 5% strain.

Although the sensor is designed to operate under typical conditions where it experiences a strain of approximately 10% throughout the majority of its operational life, there are instances—albeit rare—where it may encounter strains of up to 20%. In light of this potential variability and the need to accommodate for occasional overshoots during usage, the sensor undergoes rigorous testing at a strain level of 25% for a duration of 1000 cycles. This comprehensive testing regime is critical, as it not only ensures the sensor's reliability under normal conditions but also evaluates its performance under extreme stress scenarios. The results of the experiment indicate that the sensor effectively retains its stability and functionality, even in these more demanding conditions, thereby affirming its robustness and durability in a range of applications (Figure 3.8).

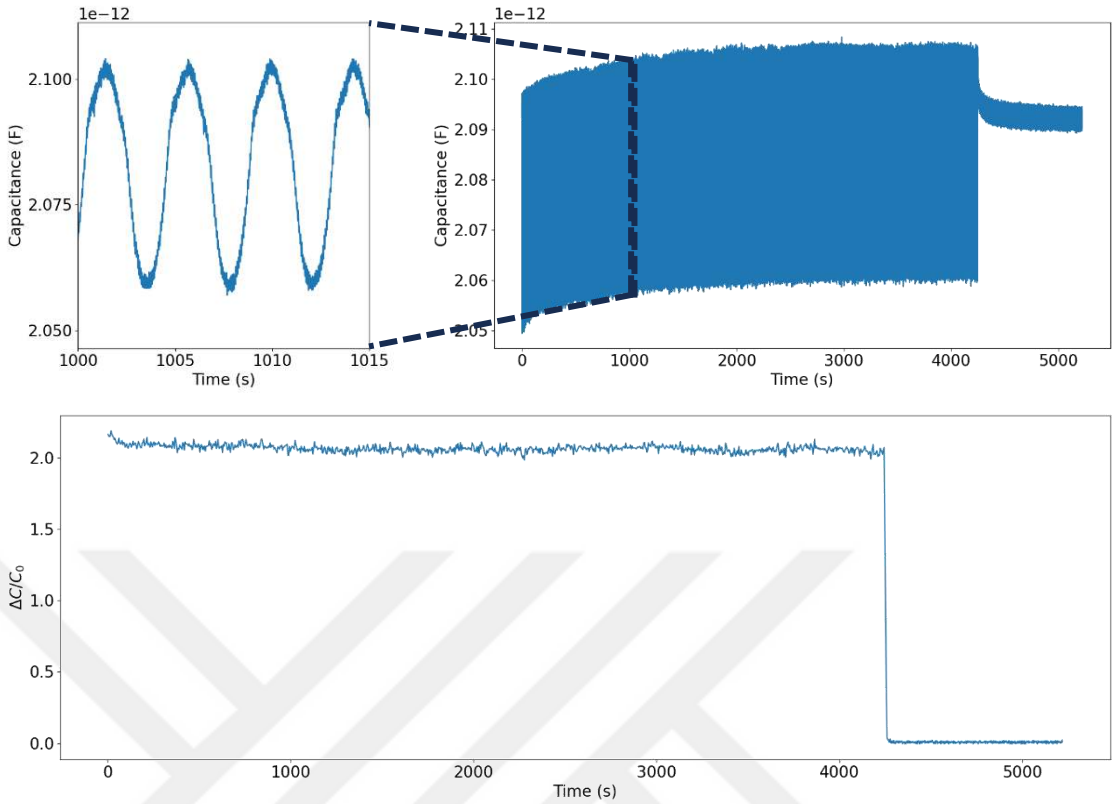

Figure 3.8: Large strain experiment at 25% strain for 1000 cycles.

The durability of the sensor is crucial, but equally important is its sensitivity, which must be evaluated in an environment that closely resembles the actual site of implantation. To achieve this, the Vivitro Superpump (Vivitro Superpump System, ViVitro Labs Inc., Canada) -a high-performance heart-simulating pulsatile pump- is utilized. This equipment is recognized as the leading system in the market for accurately replicating the dynamics of human heart function.

In the testing process, the Vivitro Superpump is meticulously prepared to assess various pumping capacities. This preparation involves configuring the pump to handle a range of fluid volumes and rates that simulate physiological conditions. By doing so, realistic stimuli are provided to the capacitive strain sensor, enabling effective evaluation of its performance and sensitivity. This approach highlights the sensor's capabilities and reinforces its potential reliability for future applications in real-world scenarios (Figure 3.9).

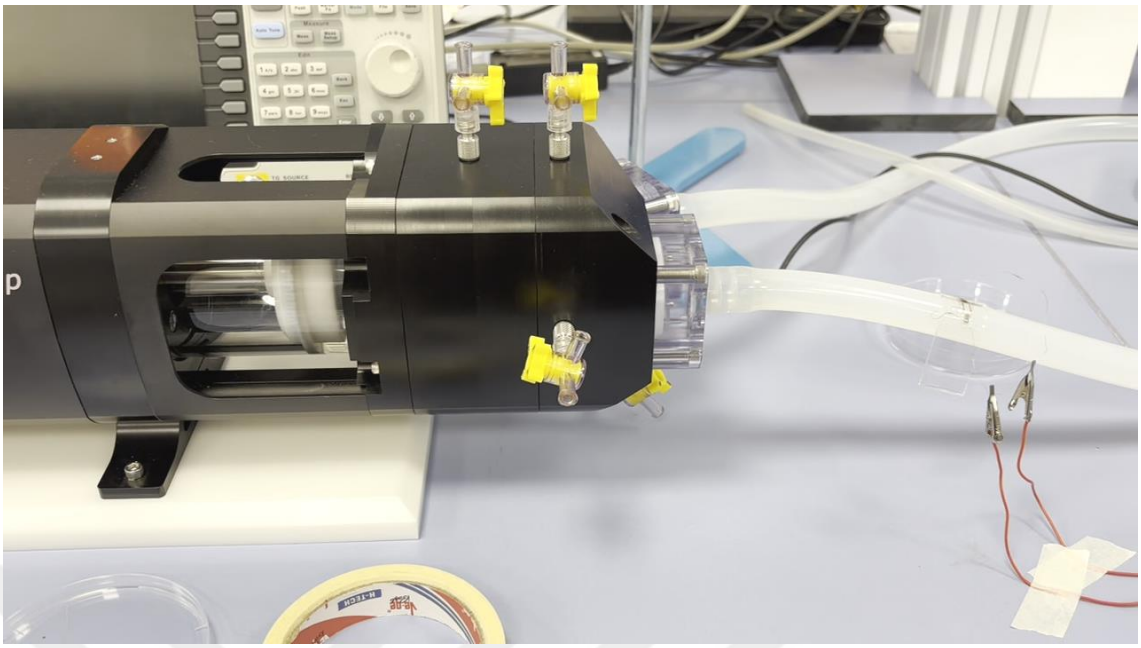

Figure 3.9: Sensitivity test setup with ViVitro Superpump.

The findings indicated that the sensor demonstrates a remarkable ability to distinguish even the smallest variations in blood flow, specifically being sensitive enough to detect changes as minimal as 5 milliliters per stroke. Additionally, it has proven capable of accurately identifying and monitoring every distinct phase of a regular heartbeat, providing a comprehensive analysis of cardiac function (Figure 3.10).

a)

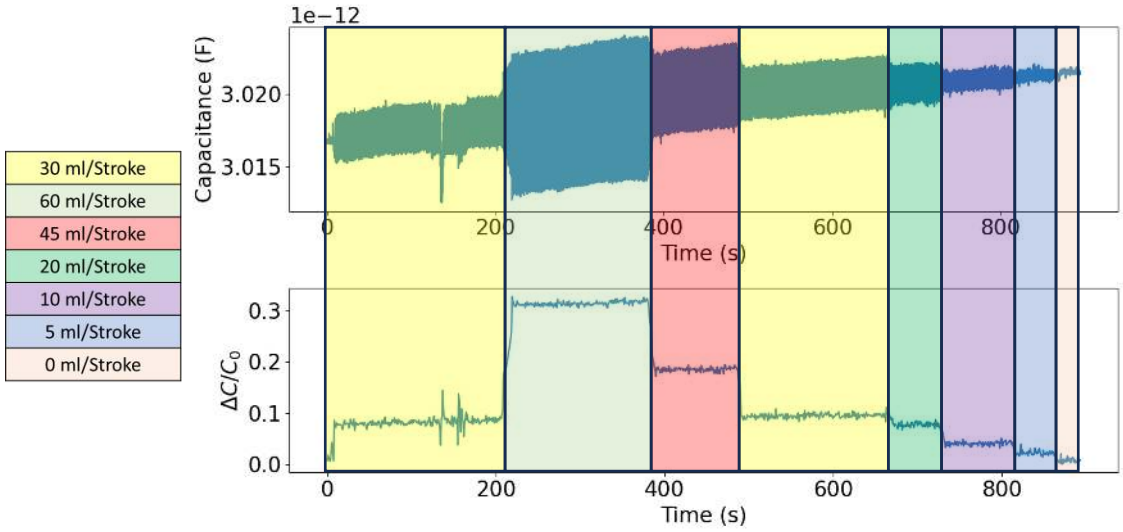

b)

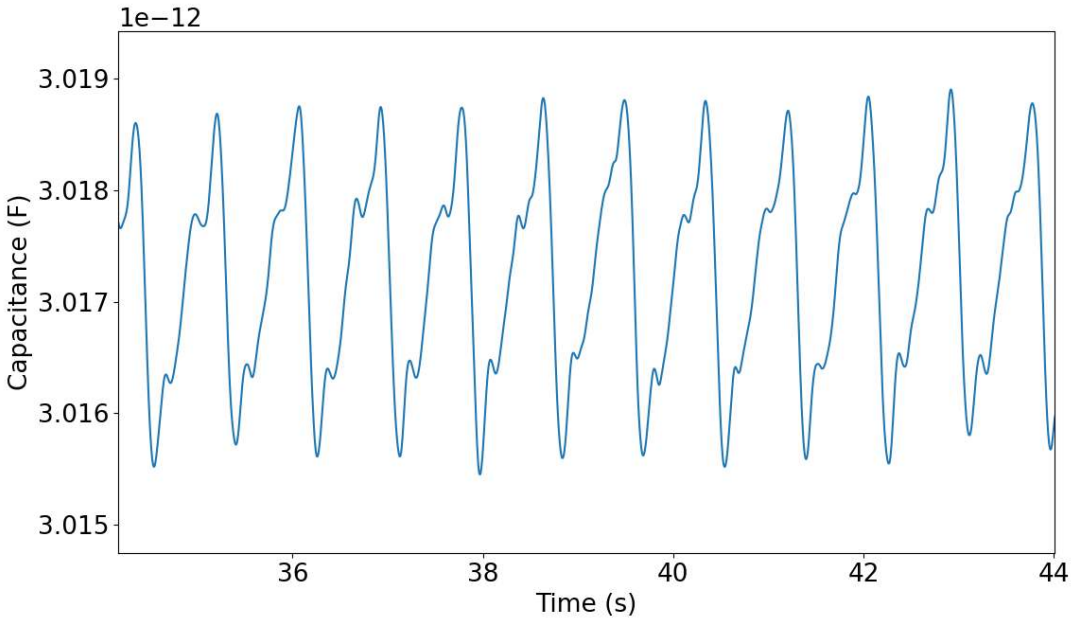

Figure 3.10: Vivitro superpump results. a) identification of pumping capacity changes. b) identification of healthy cardiovascular activity.

To ensure optimal functionality, it is essential for the sensor to exhibit insensitivity to external pressures that may be applied by the internal organs of patients. This sensitivity can vary depending on several factors, including the patient's height, weight, and the size of their internal organs. To systematically evaluate this characteristic, a comprehensive testing setup is prepared.

Initially, the sensor is mounted onto a moving stage, which is programmed to perform cyclic motion. This movement simulates the dynamic conditions that the sensor might encounter in practical applications. Next, the entire assembly, consisting of the sensor and the moving stage, is positioned beneath a Mark-10 Force Gauge (Mark-10 Corp. Copiague, NY). The purpose of the Force Gauge is to apply precise and measurable forces to the sensor, allowing for accurate assessment of its insensitivity to pressure variations. Additionally, a Z-axis stage is incorporated into the setup to provide controlled vertical adjustments, further facilitating the evaluation process. This combination of equipment is critical for conducting rigorous tests that will help ascertain the performance and reliability of the sensor under different pressure scenarios (Figure 3.11).

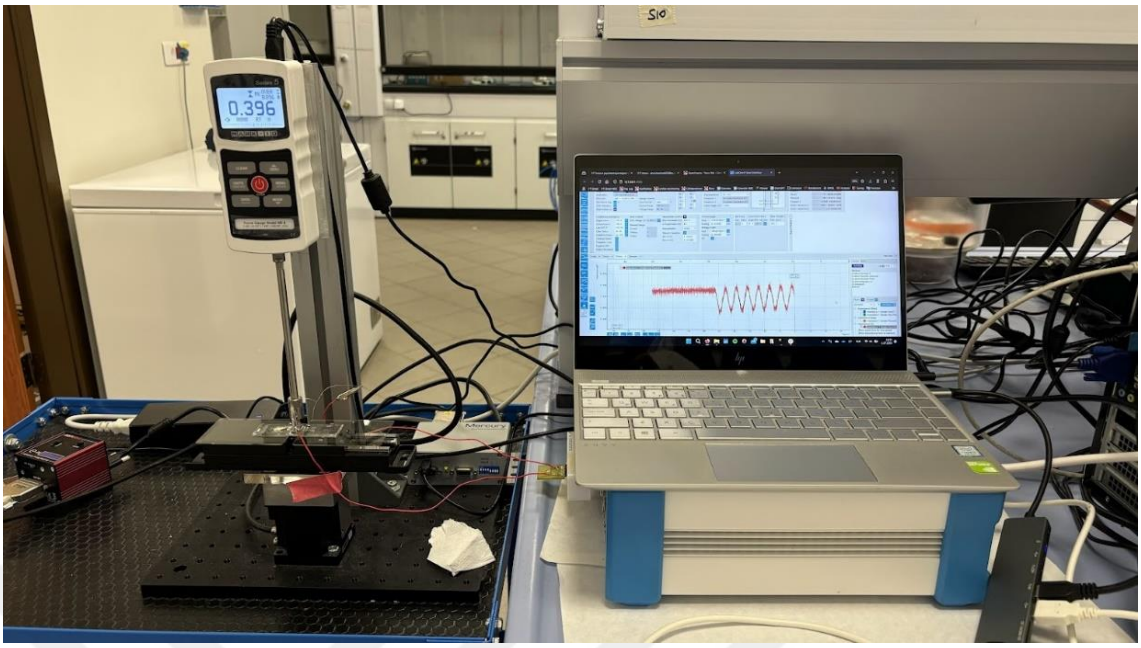

Figure 3.11: Pressure insensitivity test setup.

After the sensor was placed, it was subjected to an initial phase of cyclic motion, during which 15% cyclic strain was applied. This motion was intended to simulate the dynamic conditions that might be encountered within human body. Following the establishment of this cyclic motion, a constant force was applied to the sensor to replicate the pressure exerted by internal organs during various physiological activities.

To thoroughly assess the performance of the sensor, the experiment was conducted at three distinct pressure levels. The goal was to determine whether sensitivity could be maintained, and reliable calibration curves could be produced across all tested conditions.

The results obtained from the experiment were consistent with expectations. Each of the three pressure levels yielded calibration curves that were remarkably similar, indicating that the integrity and accuracy of the sensor were effectively retained even under varying pressures. This consistency in the calibration curves suggests robust performance of the sensor in conditions that mimic real-life human body pressures (Figure 3.12).

a)

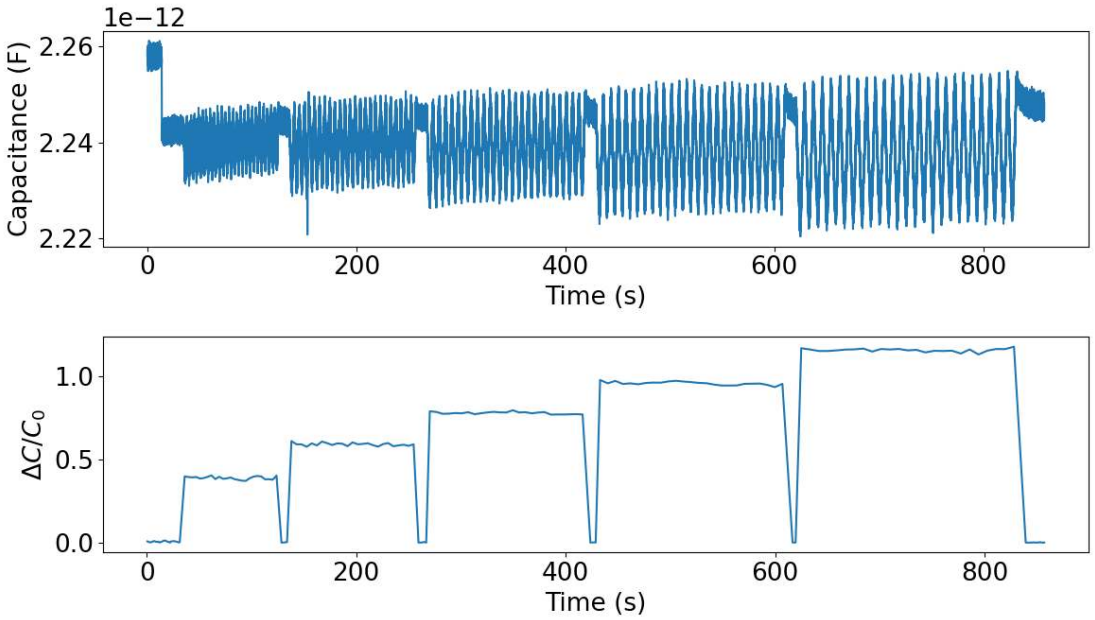
1e−12
Capacitance (F)
2.26
2.24
2.22
0
200
400
600
800
Time (s)
$\Delta C/C_0$
1.0
0.5
0.0
0
200
400
600
800
Time (s)

b)

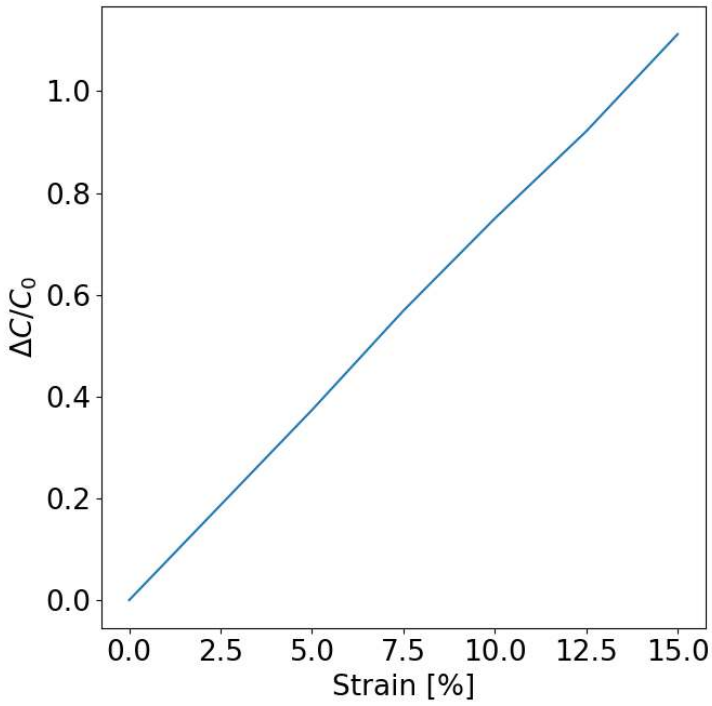
$\Delta C/C_0$
1.0
0.8
0.6
0.4
0.2
0.0
0.0
2.5
5.0
7.5
10.0
12.5
15.0
Strain [%]

c)

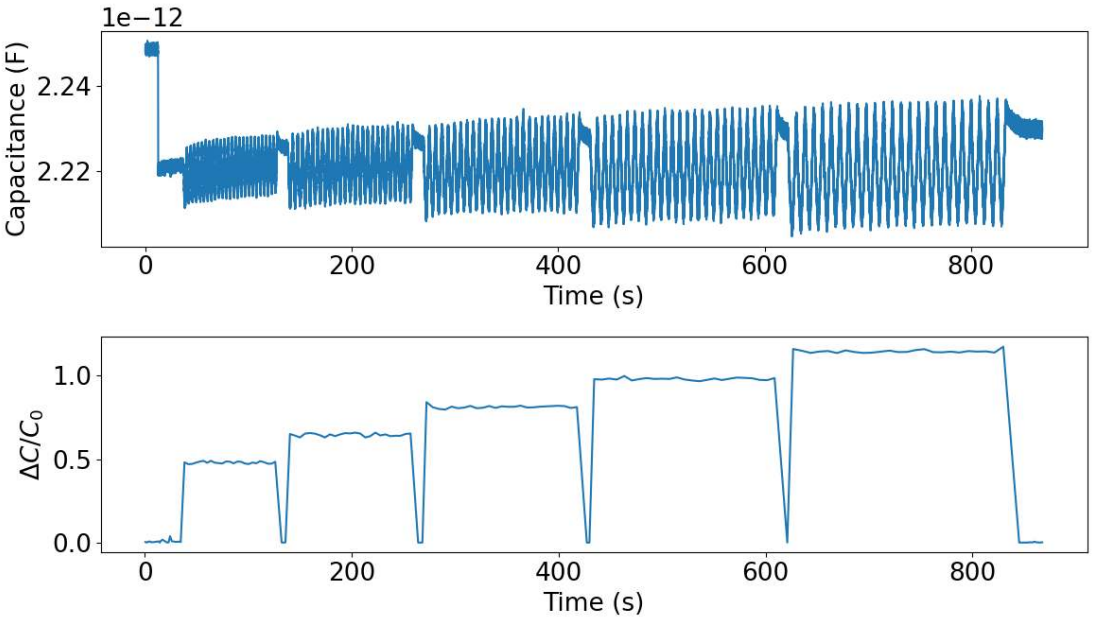
1e−12
Capacitance (F)
2.24
2.22
0
200
400
600
800
Time (s)
$\Delta C/C_0$
1.0
0.5
0.0
0
200
400
600
800
Time (s)

d)

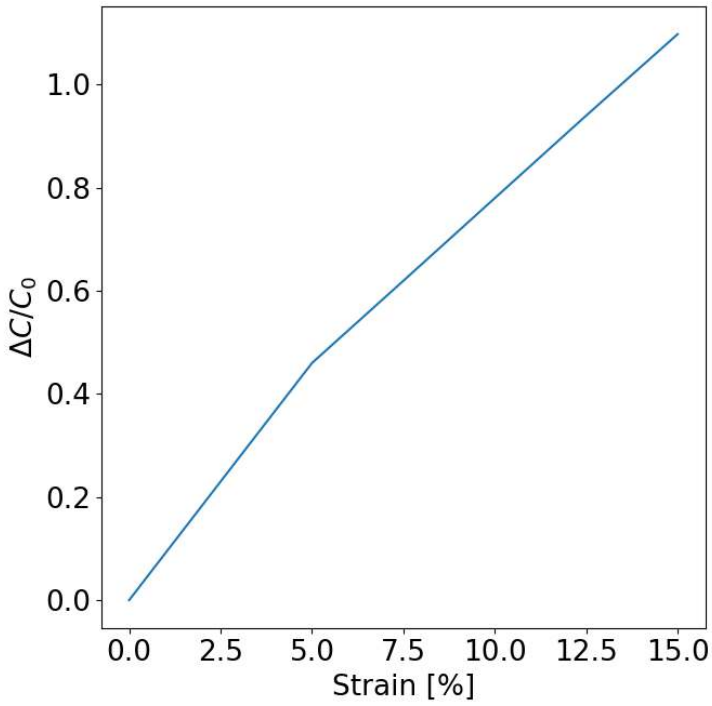
$\Delta C/C_0$
1.0
0.8
0.6
0.4
0.2
0.0
0.0
2.5
5.0
7.5
10.0
12.5
15.0
Strain [%]

e)

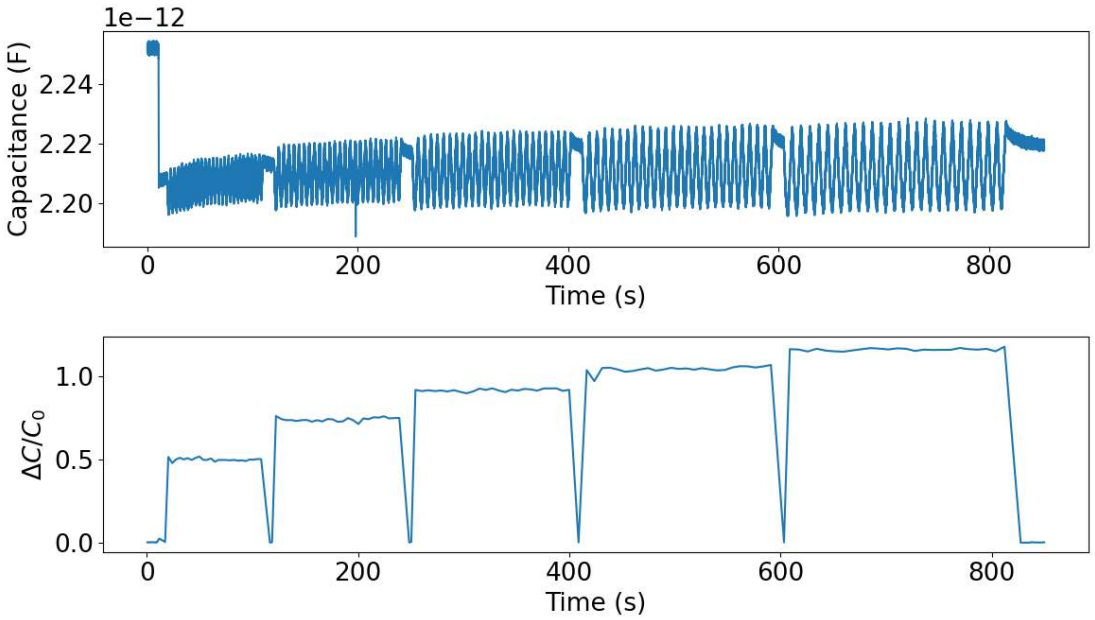
1e−12
Capacitance (F)
2.24
2.22
2.20
0
200
400
600
800
Time (s)
$\Delta C/C_0$
1.0
0.5
0.0
0
200
400
600
800
Time (s)

f)

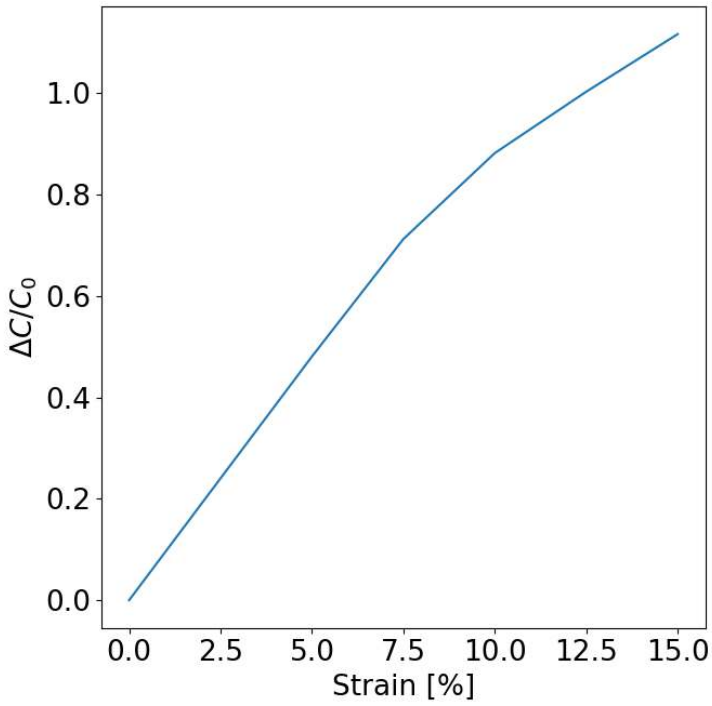
$\Delta C/C_0$
1.0
0.8
0.6
0.4
0.2
0.0
0.0
2.5
5.0
7.5
10.0
12.5
15.0
Strain [%]

g)

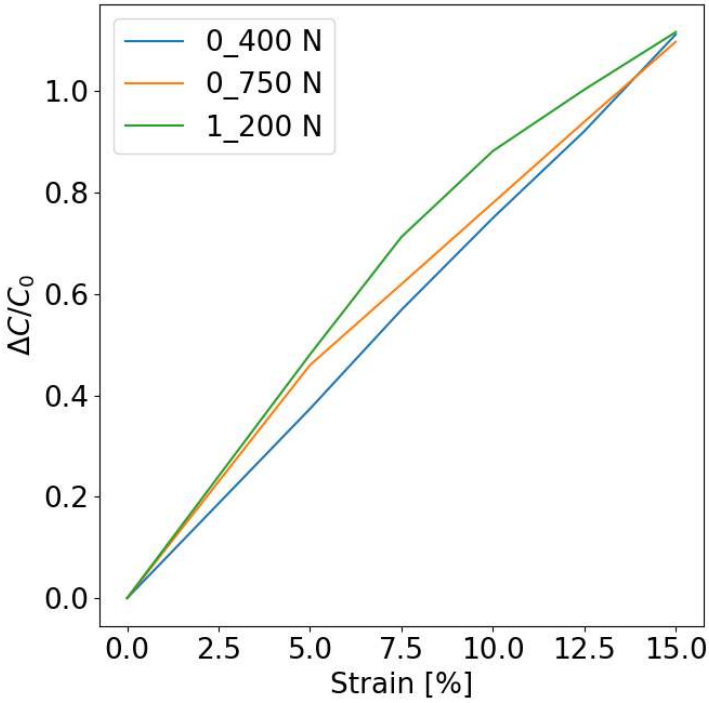

Figure 3.12: Pressure insensitivity experiment results. Sensors under a patterned cycle of 5, 7.5, 10, 12.5, 15% strain. a) 0.400 N force results and b) calibration curve. c) 0.750 N force results and d) calibration curve. e) 1.200 N force results and f) calibration curve. g) Calibration curve comparison.

In addition to the utilization of a sophisticated and highly sensitive tabletop signal collector for initial evaluations, thorough characterization of the sensor must also be conducted with a dedicated microchip to accurately simulate the conditions that would be experienced when implanted. For this purpose, FDC1004 was selected as the ADC microchip, known for its precision and reliability in capturing analog signals. To assess the compatibility and performance of the sensor with the ADC microchip, the FDC1004EVM evaluation board was employed, which is specifically designed for testing and development.

To facilitate the testing of the sensor's response, the Thorlabs MTS50-Z8 motorized stage was used, allowing for precise control over the application of strain. This setup enabled the systematic application of varying levels of strain, specifically at 5%, 10%, 15%, 20%, 25%, and 30%, each applied for 100 cycles. Accurate and repeatable movements were ensured by the motorized stage, allowing for thorough analysis and recording of the sensor's behavior under these strain conditions. This comprehensive

approach is aimed at ensuring that all necessary requirements for the sensor's intended application can be met (Figure 3.13).

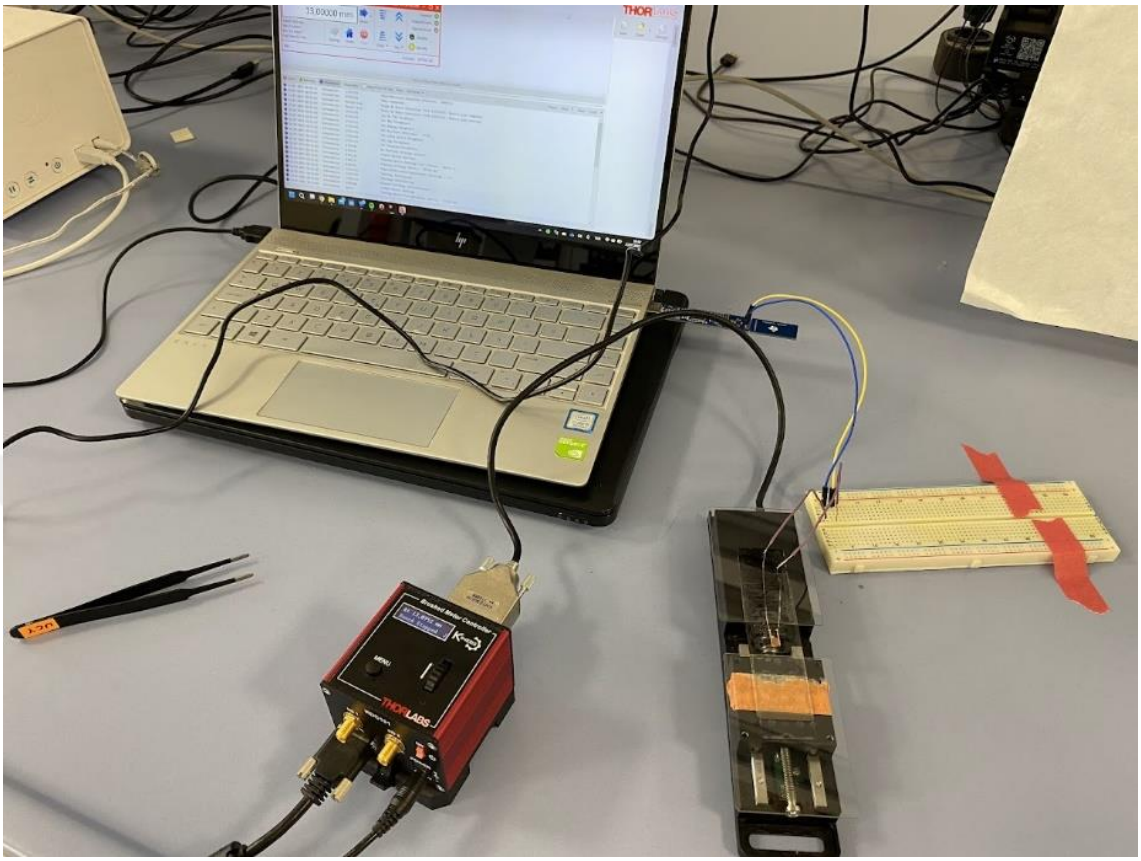

Figure 3.13: Setup for testing Texas Instruments FDC1004 sensing performance.

The results indicated that the selection of the microchip was appropriate for the intended application. Furthermore, the findings demonstrated that it is indeed possible to achieve sufficient sensitivity levels, which are crucial for the effectiveness of the device in its operational context (Figure 3.14).

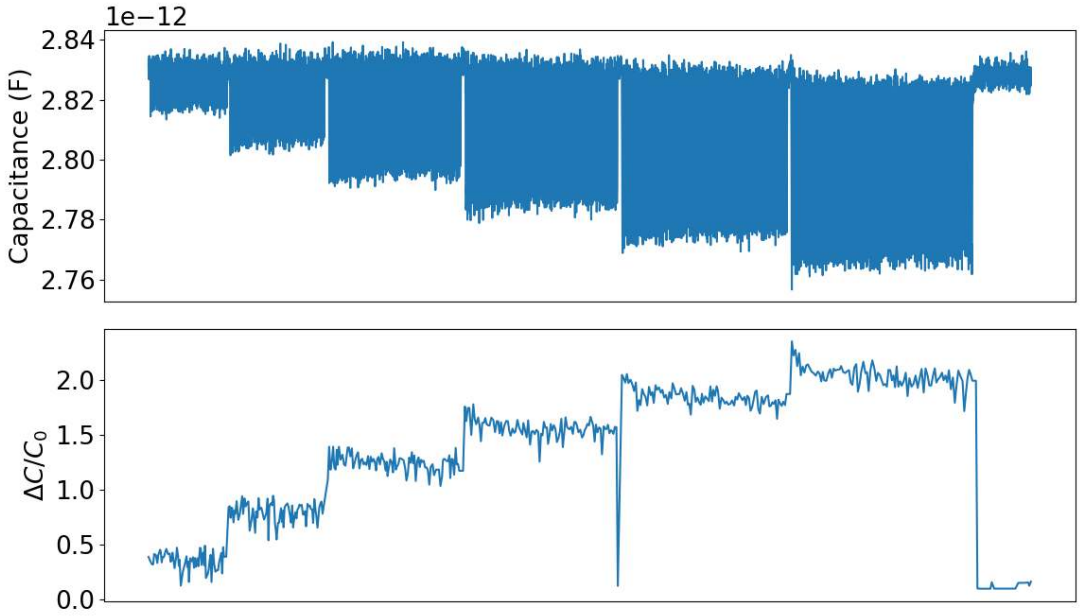

Figure 3.14: Results of Texas Instruments FDC1004 ADC microchip experiment. Sensor under a patterned cycle of 5, 10, 15, 20, 25, 30% strain.

The next step involves an assessment of the sensor's response and recovery reflexes. Given that the sensor will experience continuous and repetitive motion throughout its operational lifespan, it is crucial that both the response and recovery mechanisms function flawlessly. This ensures that the sensor can accurately detect and react to stimuli without any delays or malfunctions. Any defects in these reflexes could lead to compromised performance, potentially affecting the overall reliability and efficiency of the sensor during its use (Figure 3.15).

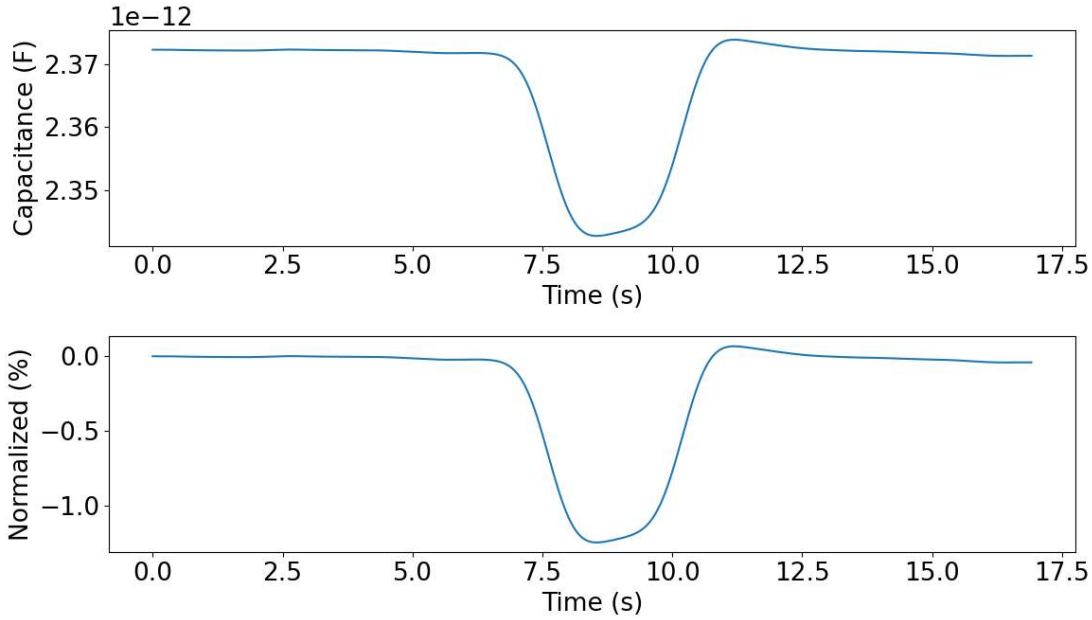

Figure 3.15: Response and recovery experiment results. 15% strain.

Before proceeding with the clinical studies of the sensor, it is essential to conduct in vivo animal tests to evaluate its performance and safety in a live organism. While the comprehensive in vivo experiments, which will involve detailed signal acquisition and a full implantation procedure, are left for future work of this thesis, an initial step has been taken to establish a foundational proof of concept. In this initial experiment, the sensor has been surgically implanted onto the myocardium of a sheep heart using suturing techniques. This preliminary implantation aims to assess not only the functionality of the sensor but also its mechanical stability within the cardiac tissue environment. The results of this initial phase will provide valuable insights and inform the subsequent stages of the research (Figure 3.16).

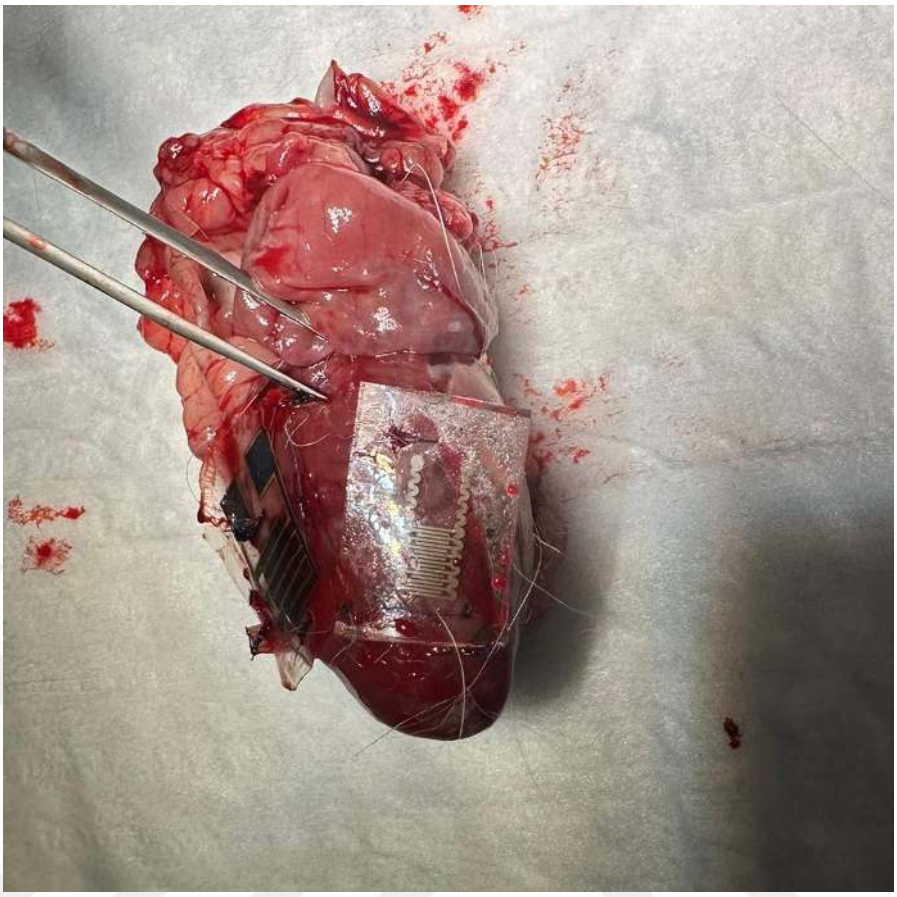

Figure 3.16: The sensor implanted on animal heart.

3.4 Optimization

The initial design serves as a foundational framework for the development of a fully implantable cardiac soft strain sensor. To enhance this design and improve the sensor's performance, a series of comprehensive optimization studies were undertaken.

These studies included an in-depth examination of the effects of pre-stretch on the sensor, which is critical for understanding how the material behaves under physiological conditions. Additionally, a thorough analysis of the material selection was conducted to determine the most suitable options that would provide the necessary sensitivity and durability.

The optimization process also involved a delicate evaluation of the PDMS compound, focusing on its formulation to achieve the desired mechanical properties. Moreover, the impact of the distance between the sensing layer and the neutral axis is investigated, as this parameter significantly influences the sensor's accuracy and responsiveness to strain changes. These optimization efforts aim to elevate the overall functionality and reliability of the cardiac strain sensor for clinical applications.

3.4.1 Effect of Pre-stretch

A variety of studies in the current literature on soft sensors indicate that their properties can be influenced by the degree of pre-stretch applied prior to their operational use. These effects often arise from either the encapsulation layer or the sensing layer of the sensors. Specifically, sensing layers that leverage piezoresistive properties typically necessitate a carefully optimized pre-stretch setting to ensure accurate performance. In contrast, our capacitive soft strain sensor is designed with the expectation that neither the encapsulation layer nor the sensing layer will require an initial pre-stretch setting.

To rigorously test this hypothesis, we subjected the sensor to a controlled pre-stretch process lasting 60 seconds, during which we applied three distinct levels of strain: 5 percent, 10 percent, and 15 percent. Following this pre-stretch phase, the sensors underwent a series of 25 repetitive cycles at a consistent strain level of 15 percent. In alignment with our initial expectations, the analysis revealed that the pre-stretch treatments did not result in any observable changes in the sensor's performance or sensing capabilities after the cycles were completed. This outcome supports the premise that our design effectively mitigates dependence on pre-stretch, highlighting its robustness under varying application scenarios. (Figure 3.17)

a)

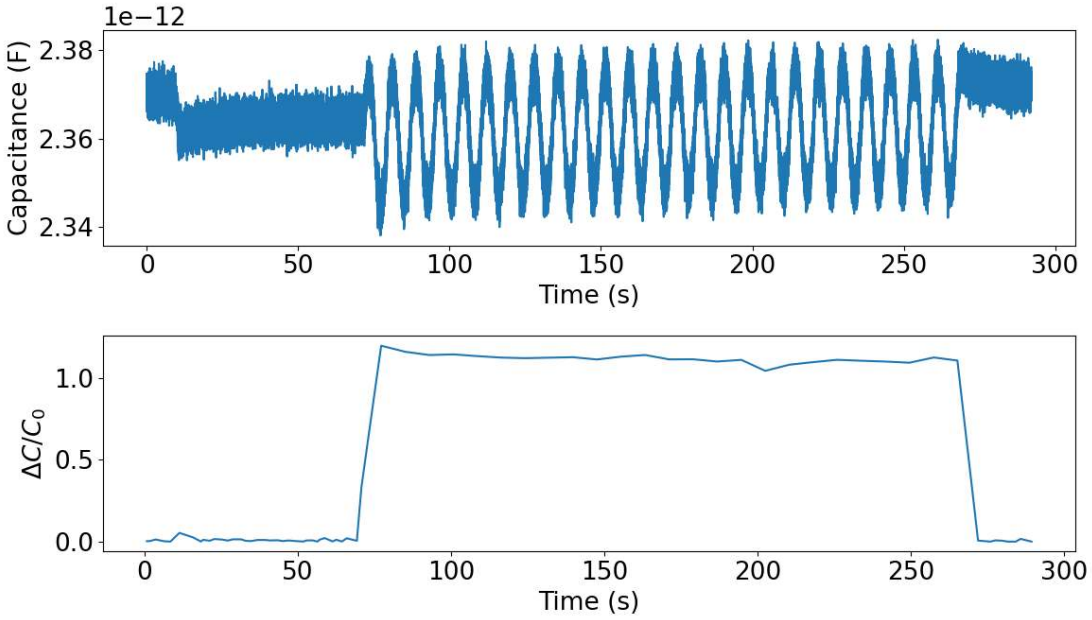
1e−12
Capacitance (F)
2.38
2.36
2.34
0
50
100
150
200
250
300
Time (s)
$\Delta C/C_0$
1.0
0.5
0.0
0
50
100
150
200
250
300
Time (s)

b)

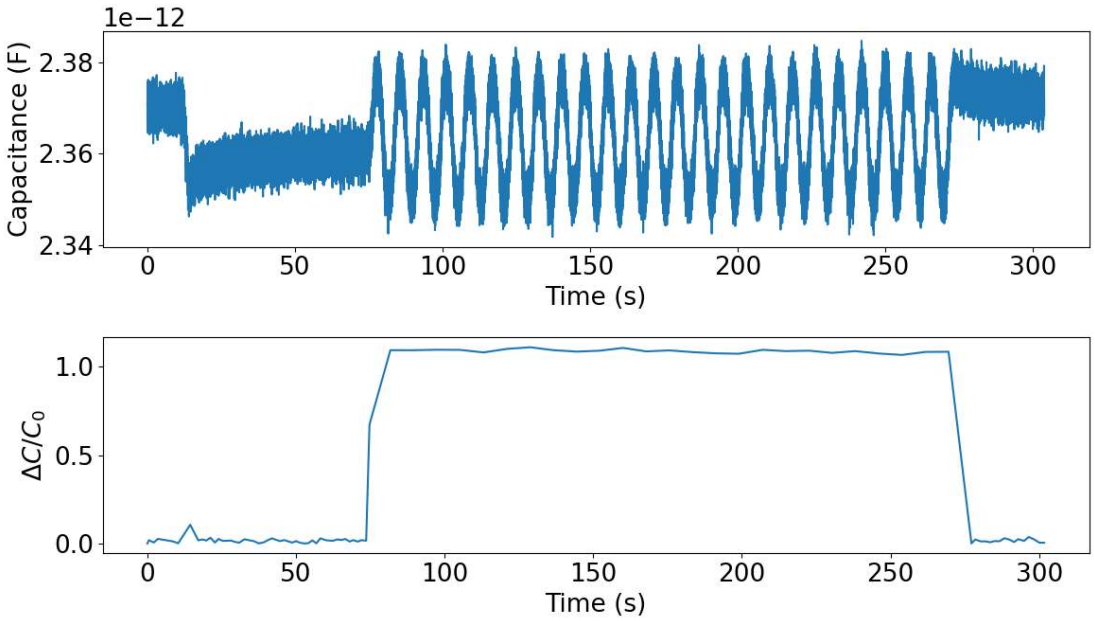
1e−12
Capacitance (F)
2.38
2.36
2.34
0
50
100
150
200
250
300
Time (s)
$\Delta C/C_0$
1.0
0.5
0.0
0
50
100
150
200
250
300
Time (s)

c)

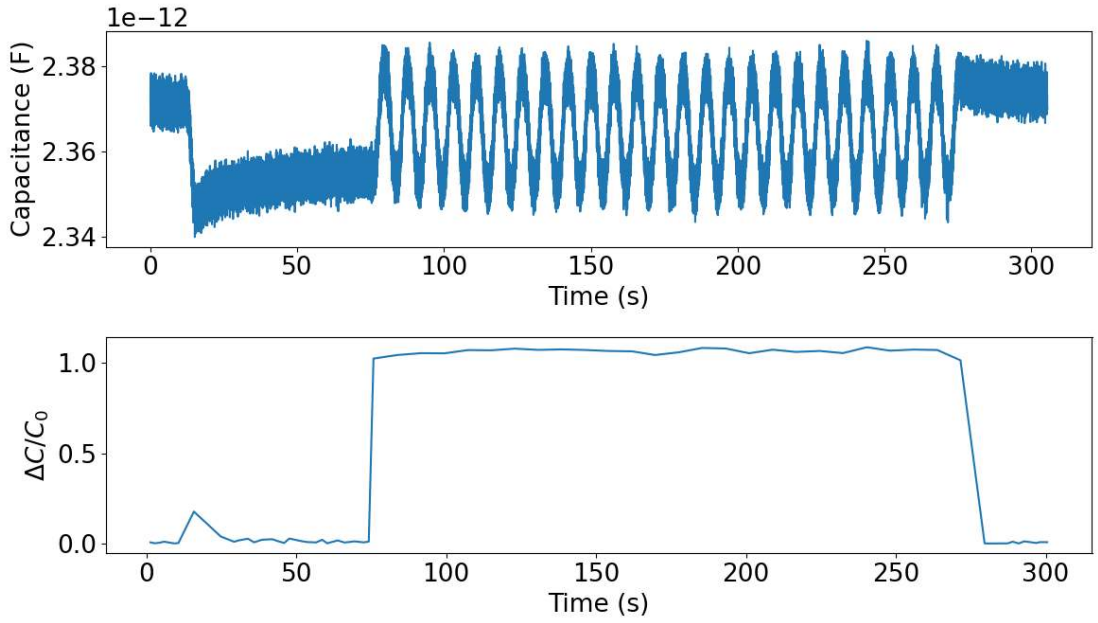

d)

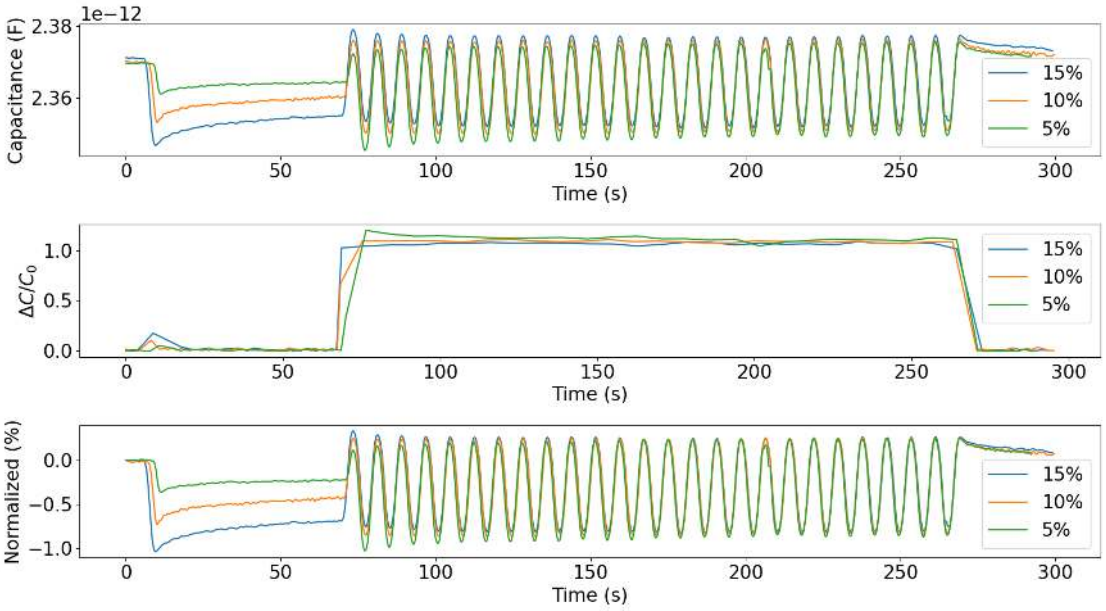

Figure 3.17: Effect of pre-stretch experiment. a) 5% strain, b) 10% strain, c) 15% strain and d) combined results.

3.4.2 Material

The encapsulation material is crucial for ensuring the sensitivity and overall performance of the sensor used in various applications, particularly in medical devices. There are specific requirements that this material must meet to function effectively in

sensitive environments, especially when interfacing with biological tissues. Primarily, the material must be biocompatible to ensure it does not provoke an adverse reaction within the body. Additionally, it should exhibit stretchability and flexibility to accommodate the dynamic movements of the heart without causing discomfort or additional strain on the surrounding tissues.

Moreover, the encapsulation material should possess a low elastic modulus. This characteristic is essential as it allows the material to deform easily in response to the natural motion of the heart, ensuring seamless integration and preventing any restrictions in movement that could affect both sensor performance and patient comfort.

Several commercially available elastomers are suitable for this application, meeting the outlined criteria. Among those considered, PDMS, EcoFlex, and Dragon Skin stand out as promising candidates due to their respective properties. However, choosing the most appropriate material involves an optimization process. Careful selection will lead to enhanced sensor performance and reliability in medical applications.

The fabricated sensors underwent a comprehensive characterization process consisting of two critical steps to assess their mechanical properties and performance in strain sensing applications.

The initial phase involved conducting a tensile test, which is essential for determining the elastic modulus of each material. This measurement not only provides insight into the material's stiffness but also allows for an estimation of the sensors' sensitivity. The results of the tensile tests revealed a significant variation in the elastic moduli among the materials used. Notably, PDMS demonstrated the highest strength, exhibiting an elastic modulus of 992 kPa. In contrast, Dragon Skin silicone followed as the second strongest material with an elastic modulus measured at 182 kPa. Meanwhile, Eco-Flex, although preferred for its flexibility, displayed the lowest elastic modulus value at 85 kPa.

Building on these findings, sensitivity tests were subsequently conducted to evaluate the performance of the sensors further. According to established theoretical principles, it is anticipated that the material with the highest elastic modulus would exhibit the greatest sensitivity to strain. To verify this hypothesis, calibration curves were derived for each sensor by performing a series of cyclic strain tests at varying strain levels, reaching up to 15%.

Analysis of the results revealed a direct correlation with the theoretical expectations: PDMS sensors exhibited the highest sensitivity, aligning with their superior elastic

modulus. Dragon Skin sensors followed in sensitivity, while Eco-Flex sensors confirmed their position as the least sensitive among the tested materials. These findings underscore the relationship between material stiffness and sensor performance, providing valuable insights for future applications in strain sensing technologies (Figure 3.18).

a)

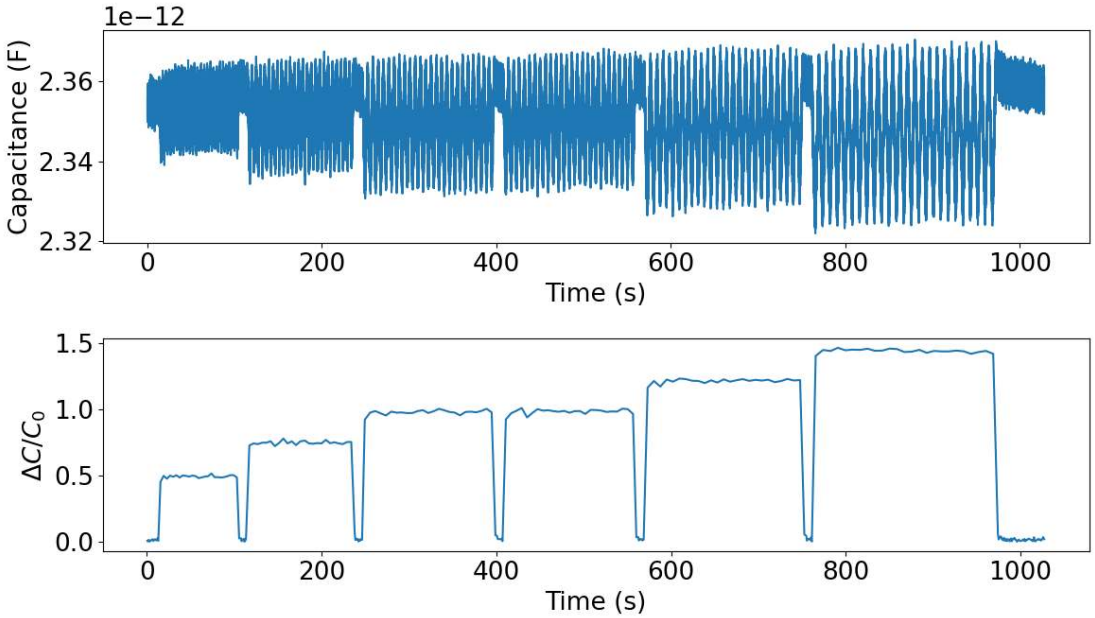

b)

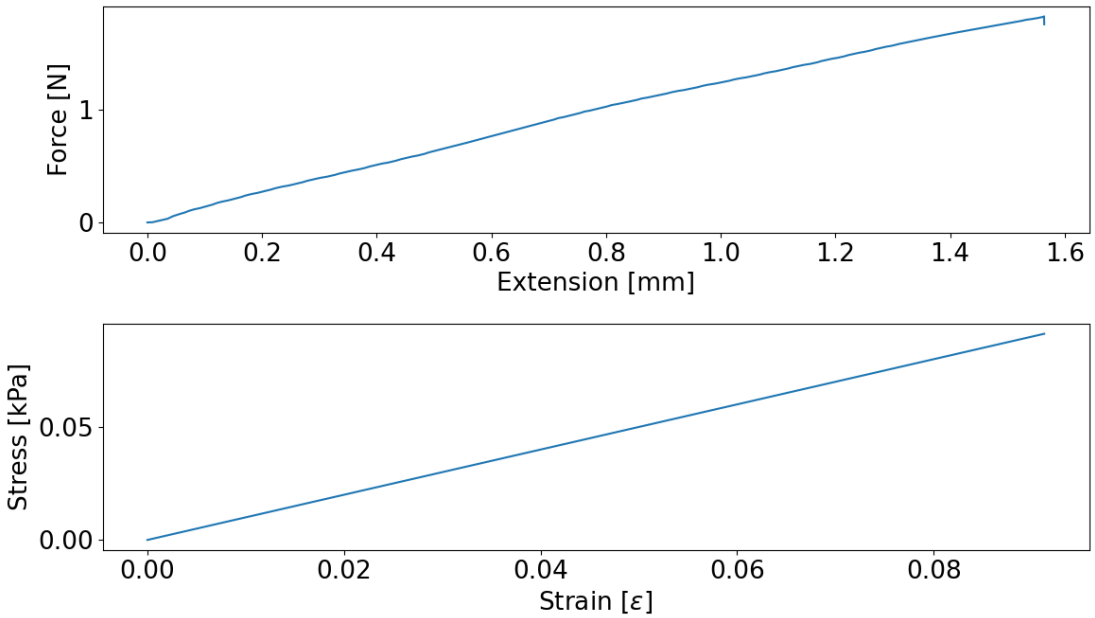
Force [N]
1
0
0.0
0.2
0.4
0.6
0.8
1.0
1.2
1.4
1.6
Extension [mm]
Stress [kPa]
0.05
0.00
0.00
0.02
0.04
0.06
0.08
Strain [ε]

c)

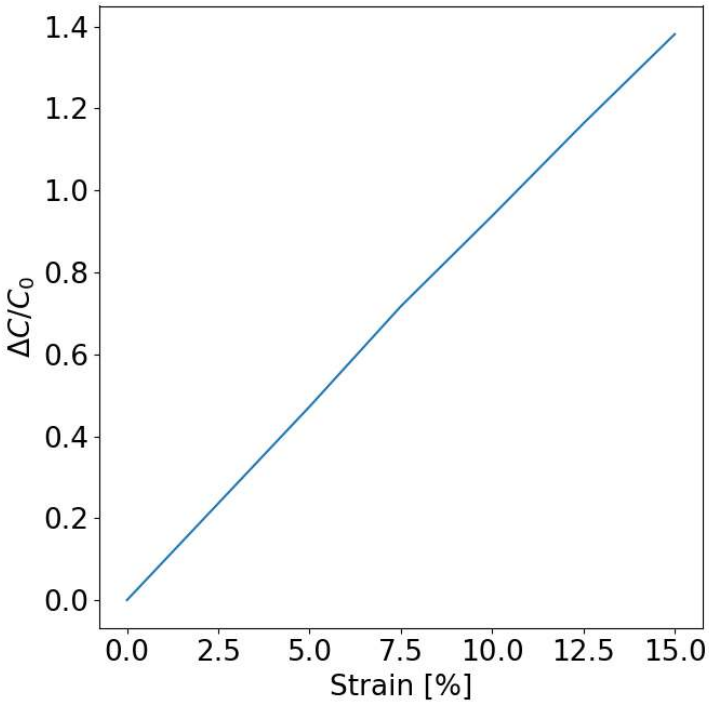
1.4
1.2
1.0
0.8
0.6
0.4
0.2
0.0
ΔC/C0
0.0
2.5
5.0
7.5
10.0
12.5
15.0
Strain [%]

d)

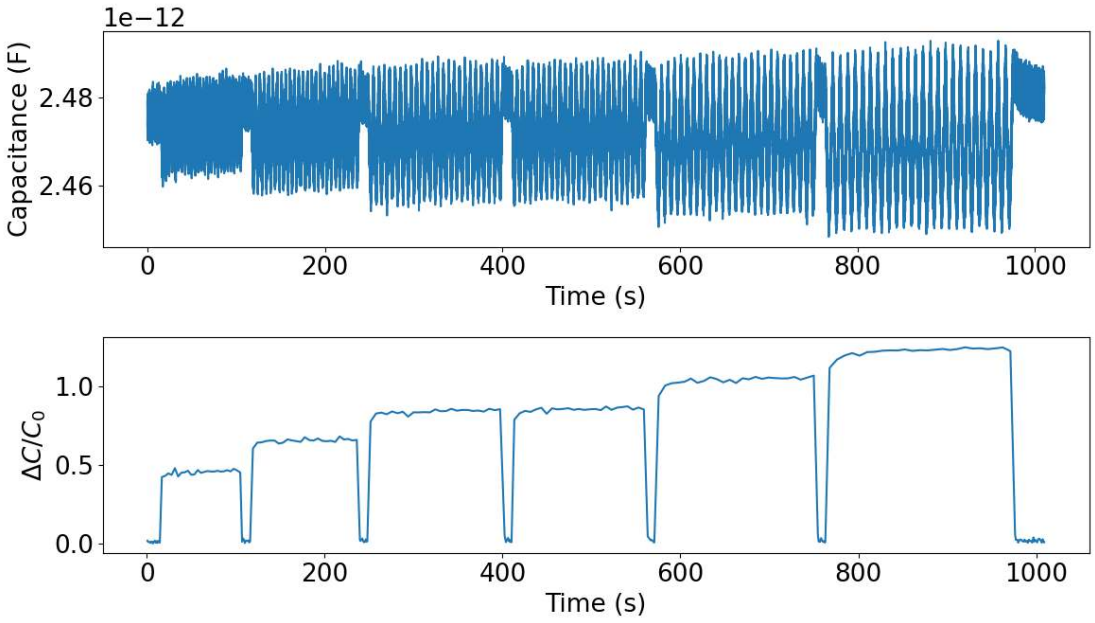
1e−12
Capacitance (F)
2.48
2.46
0
200
400
600
800
1000
Time (s)
$\Delta C/C_0$
1.0
0.5
0.0
0
200
400
600
800
1000
Time (s)

e)

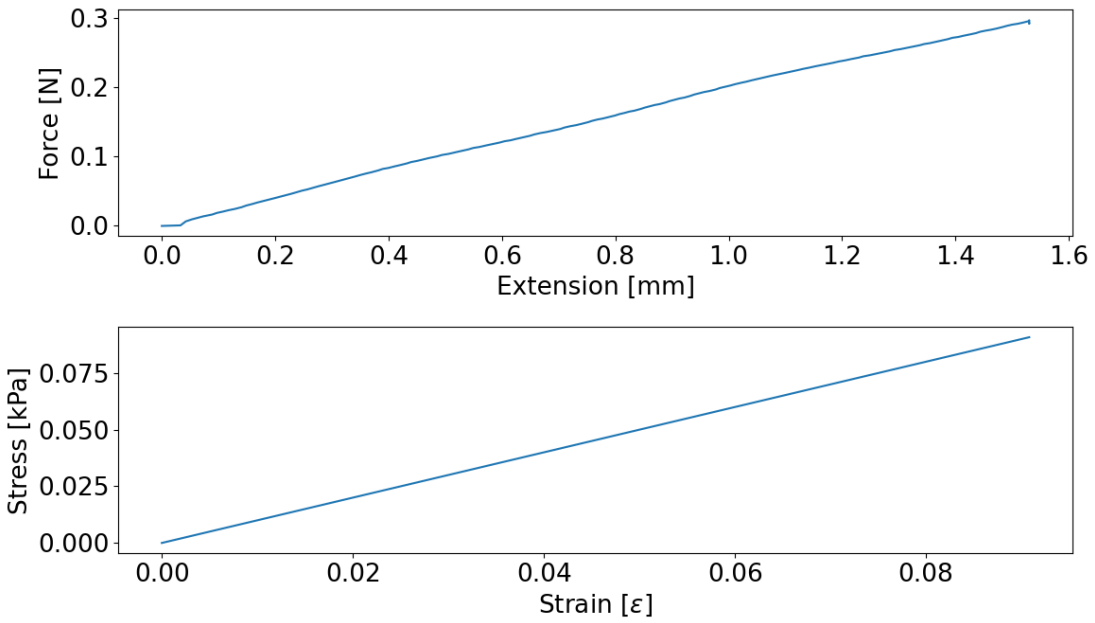
Force [N]
0.3
0.2
0.1
0.0
0.0
0.2
0.4
0.6
0.8
1.0
1.2
1.4
1.6
Extension [mm]
Stress [kPa]
0.075
0.050
0.025
0.000
0.00
0.02
0.04
0.06
0.08
Strain [ε]

f)

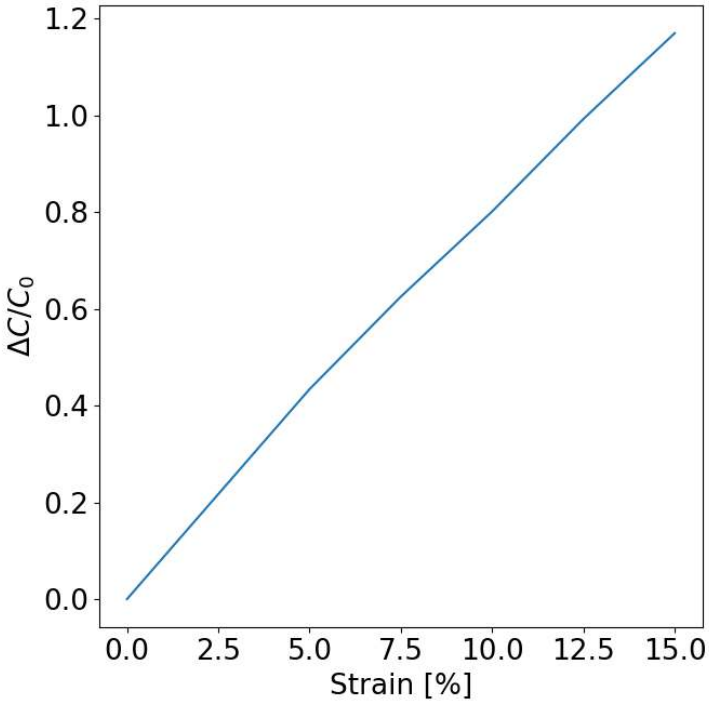
1.2
1.0
0.8
0.6
0.4
0.2
0.0
$\Delta C/C_0$
0.0
2.5
5.0
7.5
10.0
12.5
15.0
Strain [%]

g)

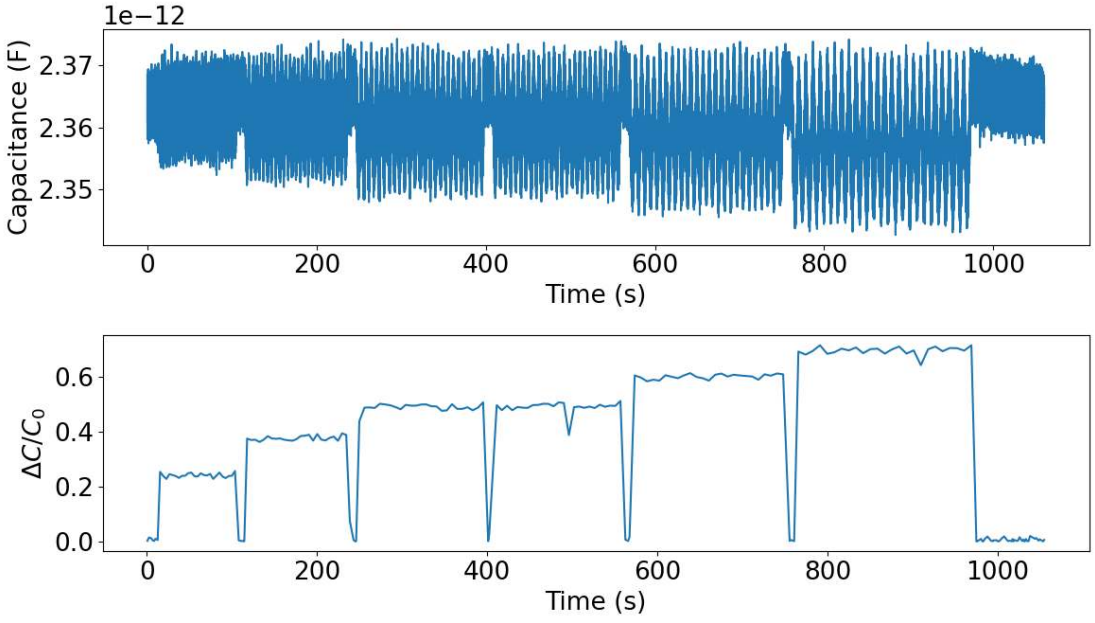
1e−12
Capacitance (F)
2.37
2.36
2.35
0
200
400
600
800
1000
Time (s)
$\Delta C/C_0$
0.6
0.4
0.2
0.0
0
200
400
600
800
1000
Time (s)

h)

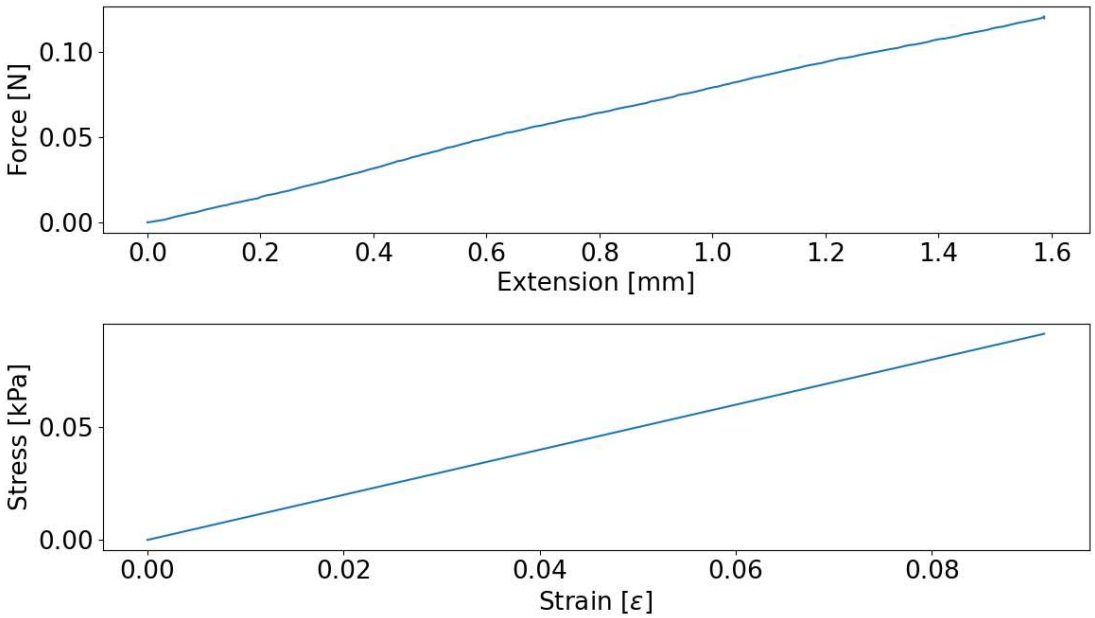
Force [N]
0.10
0.05
0.00
0.0
0.2
0.4
0.6
0.8
1.0
1.2
1.4
1.6
Extension [mm]
Stress [kPa]
0.05
0.00
0.00
0.02
0.04
0.06
0.08
Strain [ε]

i)

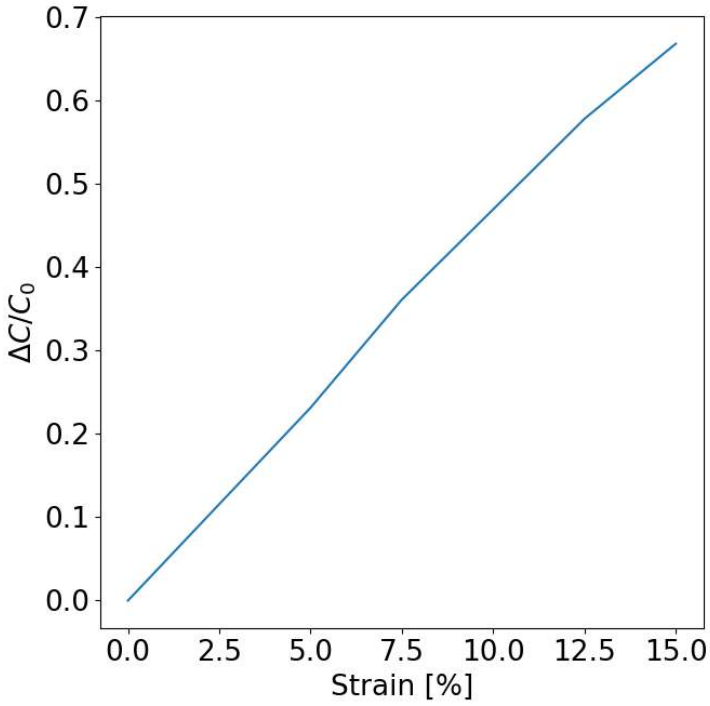
0.7
0.6
0.5
0.4
0.3
0.2
0.1
0.0
ΔC/C0
0.0
2.5
5.0
7.5
10.0
12.5
15.0
Strain [%]

j)

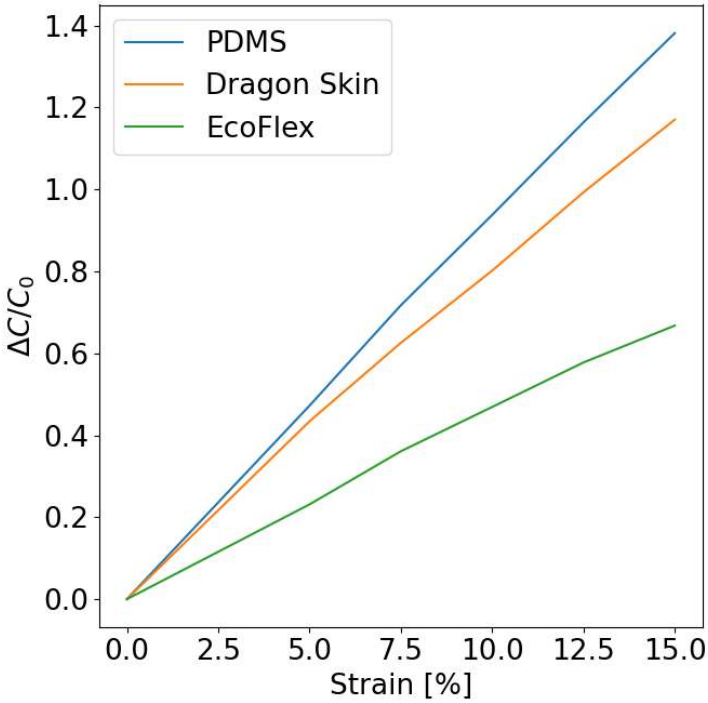

Figure 3.18: Material optimization results. Sensors under a patterned cycle of 5, 7.5, 10, 10, 12.5, 15% strain. a) cyclic strain results, b) force-displacement results, c) calibration curve of PDMS. d) cyclic strain results, e) force-displacement results, f) calibration curve of Dragon Skin. g) cyclic strain results, h) force-displacement results, i) calibration curve of EcoFlex. j) Calibration curve comparison.

3.4.3 PDMS Compound Optimization

The results from the optimization of encapsulation materials indicate that PDMS demonstrates the highest sensitivity in sensor applications while maintaining essential properties such as biocompatibility, flexibility, and stretchability. Additionally, PDMS features a relatively low elastic modulus, making it an ideal choice for delicate sensor designs.

An advantageous characteristic of PDMS is its ability to be finely tuned through variations in its fabrication process. For this study, the primary objective is to fabricate a sensor that possesses maximum sensitivity and delicateness. To achieve this, we focus on optimizing the fabrication flow of the PDMS encapsulation layer. Specifically, the manipulation of the base to curing agent ratio is identified as a key parameter for optimization.

We have selected three candidate ratios for our experiments: 10:1, 20:1, and 30:1 by wt.% of base to curing agent. The theoretical framework suggests that increasing the

proportion of curing agent in the mixture should result in a compound with an elevated elastic modulus. This increase in elastic modulus could potentially affect the overall performance characteristics of the sensor, making it crucial to analyze the effects of different ratios on the final material properties. By carefully investigating these parameters, we aim to develop the PDMS-based encapsulation layer that will enhance the sensitivity and functionality of the sensors.

In order to evaluate the performance of the sensors in relation to theoretical predictions, a series of tensile tests were conducted. These tests were carried out using the Linkam MFS. Each sensor was securely positioned within the testing apparatus utilizing mechanical jaws, ensuring stability and accurate data collection during the experiments.

The results from the tensile tests were highly consistent with the underlying theoretical framework, revealing distinct differences in elastic modulus values among the various sensor configurations. Specifically, the sensor with a 10:1 ratio exhibited the highest elastic modulus, measuring 1500 kPa. In contrast, the sensor with a 20:1 ratio demonstrated a lower elastic modulus of 460 kPa, while the 30:1 ratio sensor showed the least with an elastic modulus of 250 kPa. These findings underscore the significant impact of the curing agent ratio on material stiffness.

Following the tensile tests, we proceeded to assess the sensitivity of the sensors by applying a series of strain levels in a cyclic manner. This approach allowed for the generation of calibration curves, which are essential for understanding sensor behavior under varying levels of stress. Once again, the results aligned with theoretical expectations, indicating that the sensor with a 10:1 ratio was the most sensitive in detecting changes in strain, while the 30:1 ratio sensor displayed the least sensitivity. This comprehensive evaluation of both elastic modulus and sensitivity provides valuable insights into the performance characteristics of the sensors under testing (Figure 3.19).

a)

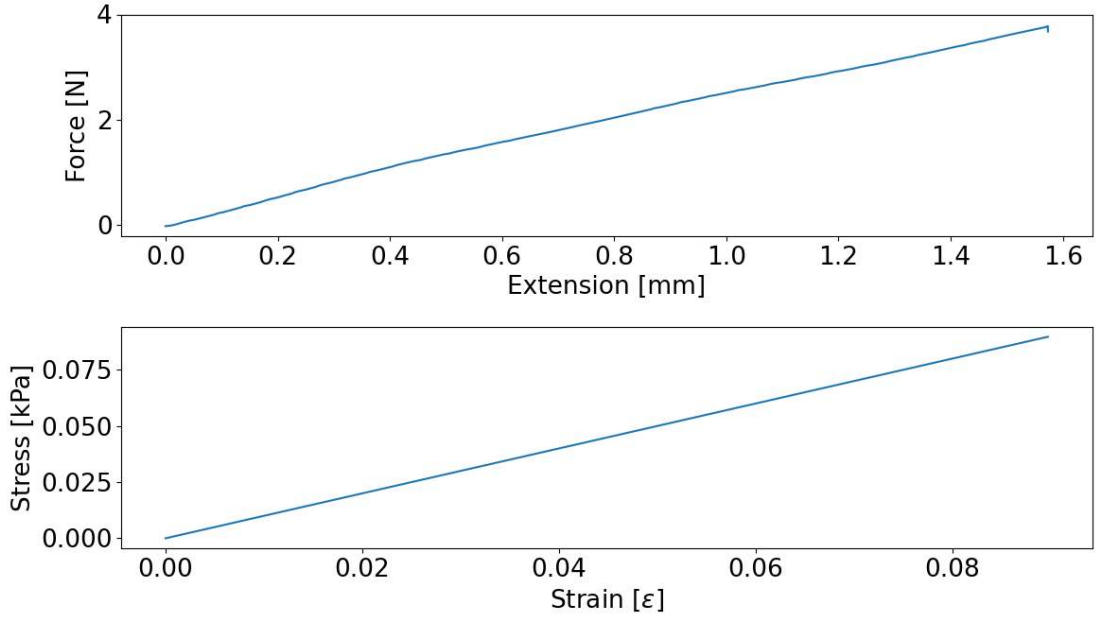
Force [N]
Extension [mm]
Stress [kPa]
Strain [ε]

b)

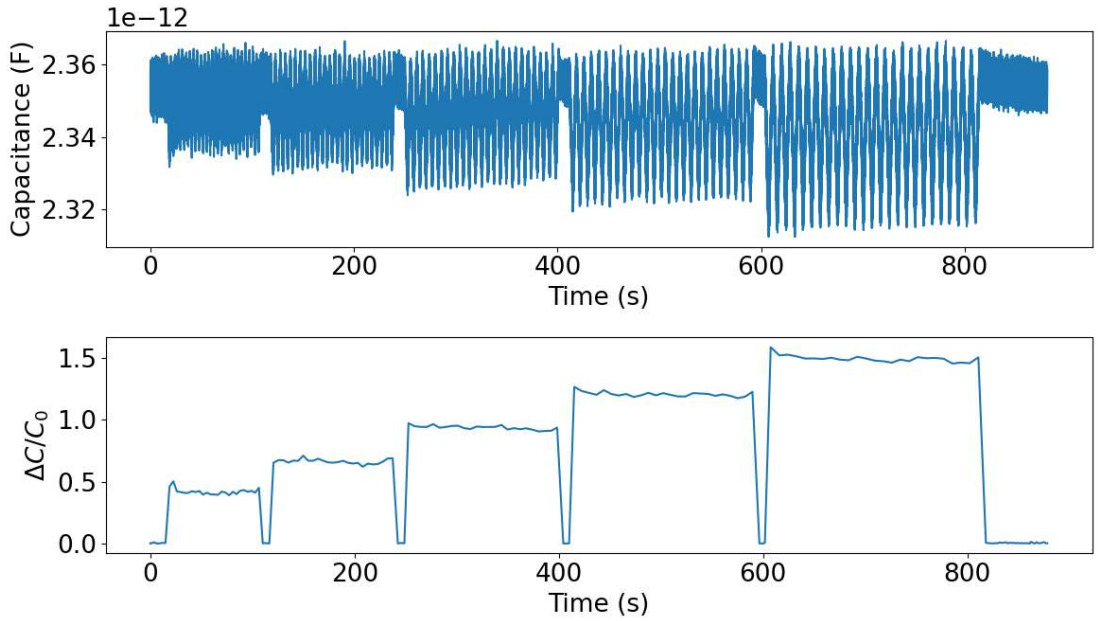
1e−12
Capacitance (F)
Time (s)
ΔC/C0
Time (s)

c)

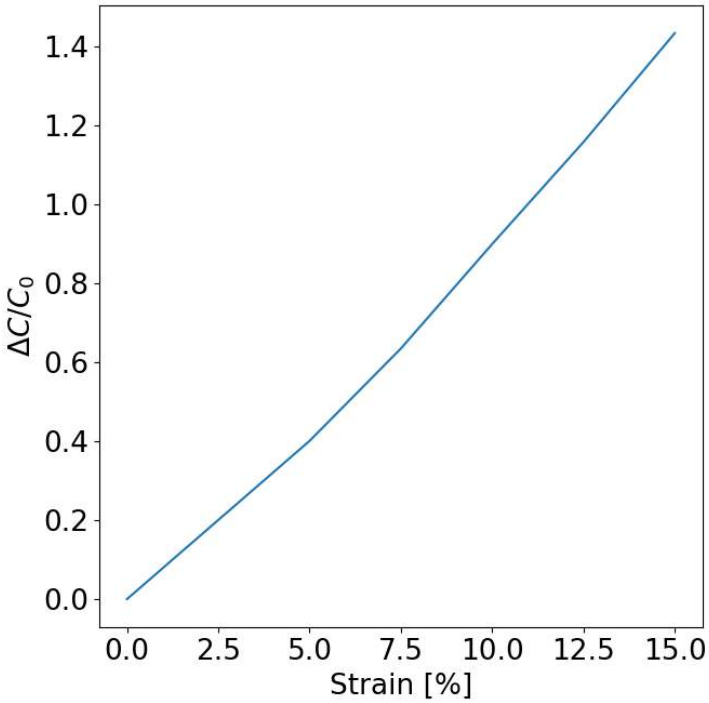
1.4
1.2
1.0
0.8
0.6
0.4
0.2
0.0
$\Delta C/C_0$
0.0
2.5
5.0
7.5
10.0
12.5
15.0
Strain [%]

d)

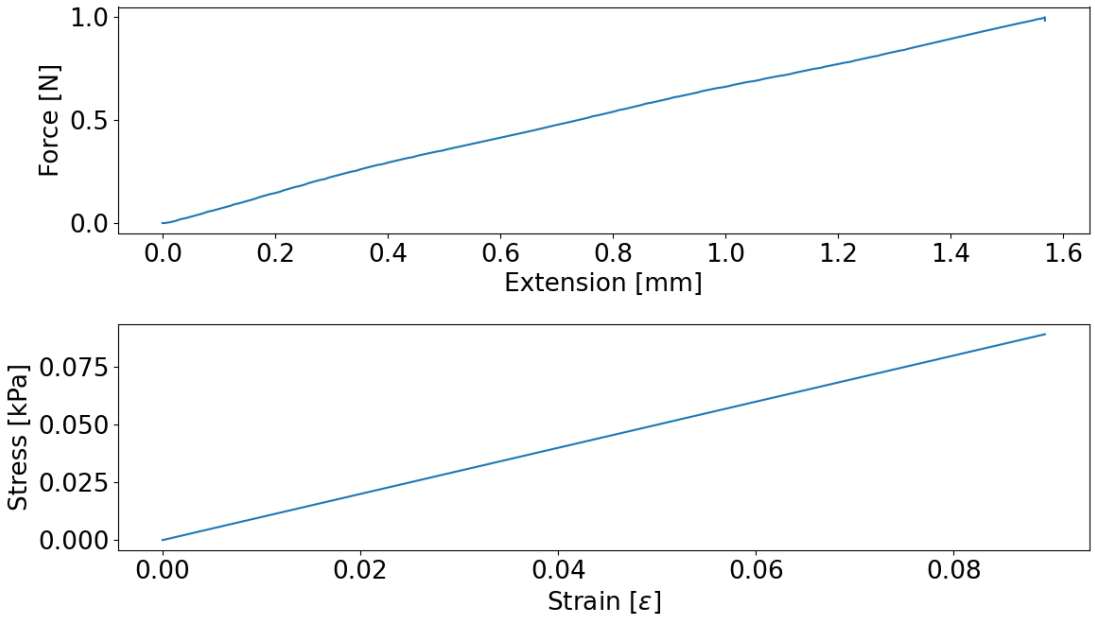
1.0
0.5
0.0
Force [N]
0.0
0.2
0.4
0.6
0.8
1.0
1.2
1.4
1.6
Extension [mm]
0.075
0.050
0.025
0.000
Stress [kPa]
0.00
0.02
0.04
0.06
0.08
Strain [ε]

e)

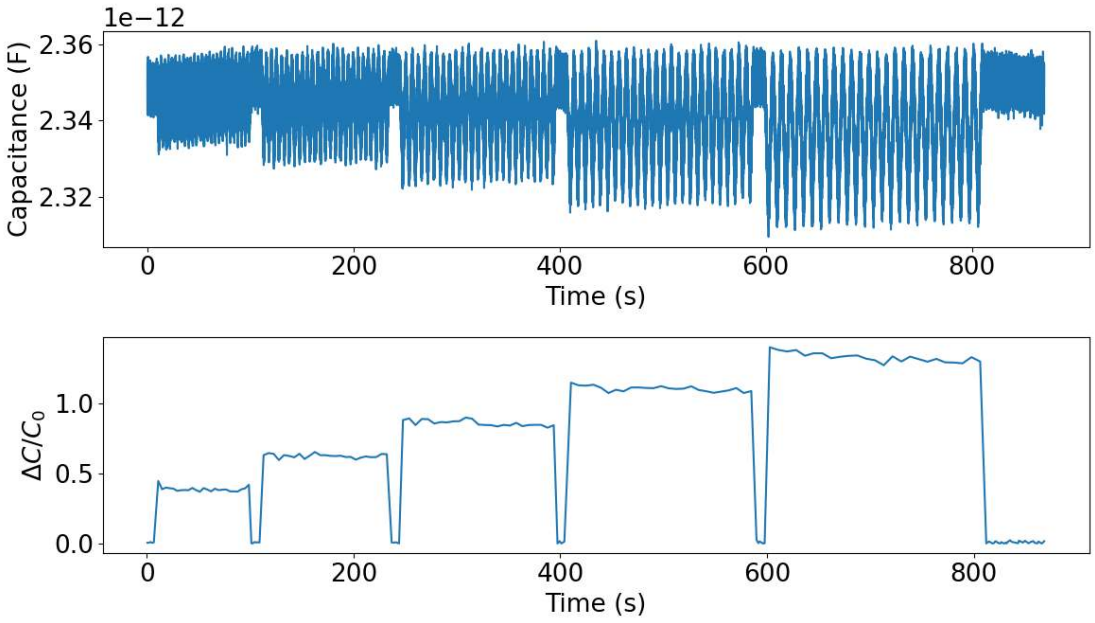
1e−12
Capacitance (F)
2.36
2.34
2.32
0
200
400
600
800
Time (s)
$\Delta C/C_0$
1.0
0.5
0.0
0
200
400
600
800
Time (s)

f)

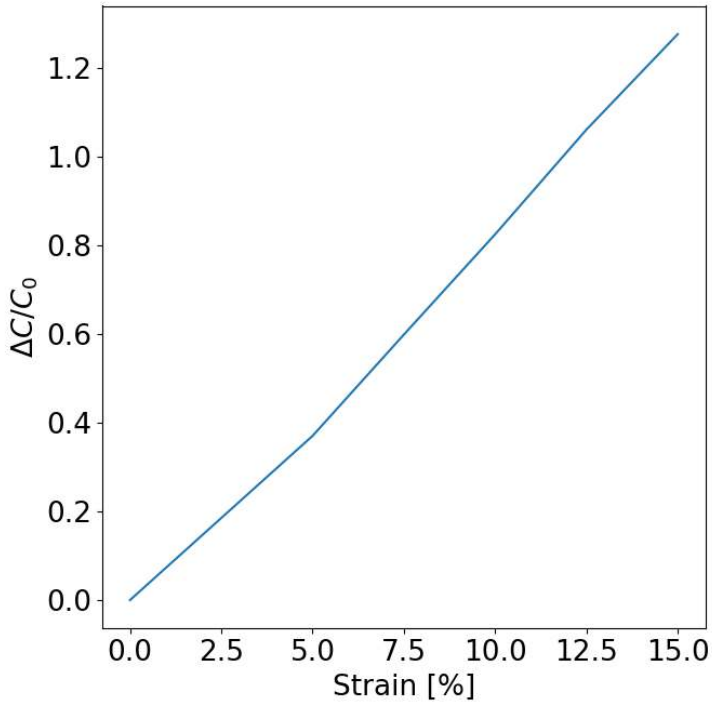
$\Delta C/C_0$
1.2
1.0
0.8
0.6
0.4
0.2
0.0
0.0
2.5
5.0
7.5
10.0
12.5
15.0
Strain [%]

g)

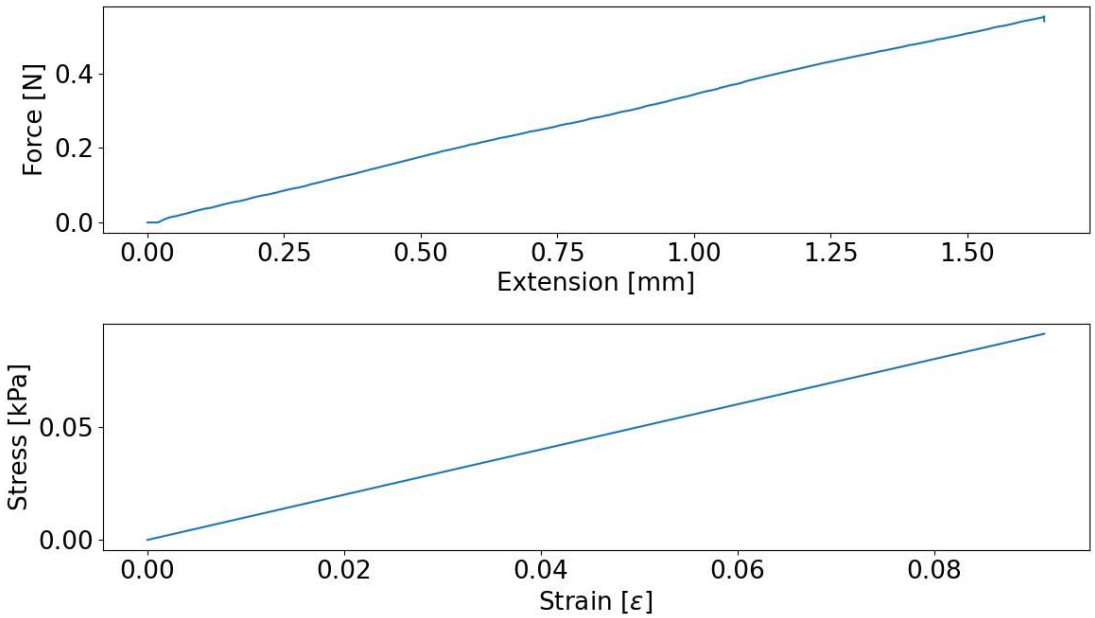
Force [N]
0.0
0.2
0.4
0.00
0.25
0.50
0.75
1.00
1.25
1.50
Extension [mm]
Stress [kPa]
0.00
0.05
0.00
0.02
0.04
0.06
0.08
Strain [ε]

h)

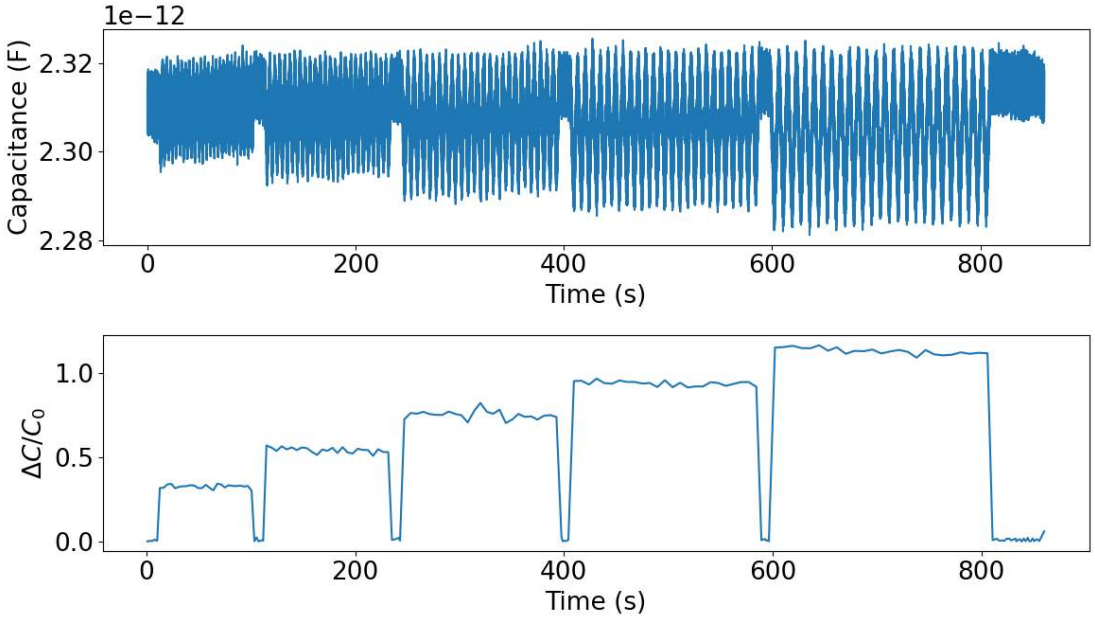
1e−12
Capacitance (F)
2.28
2.30
2.32
0
200
400
600
800
Time (s)
ΔC/C0
0.0
0.5
1.0
0
200
400
600
800
Time (s)

i)

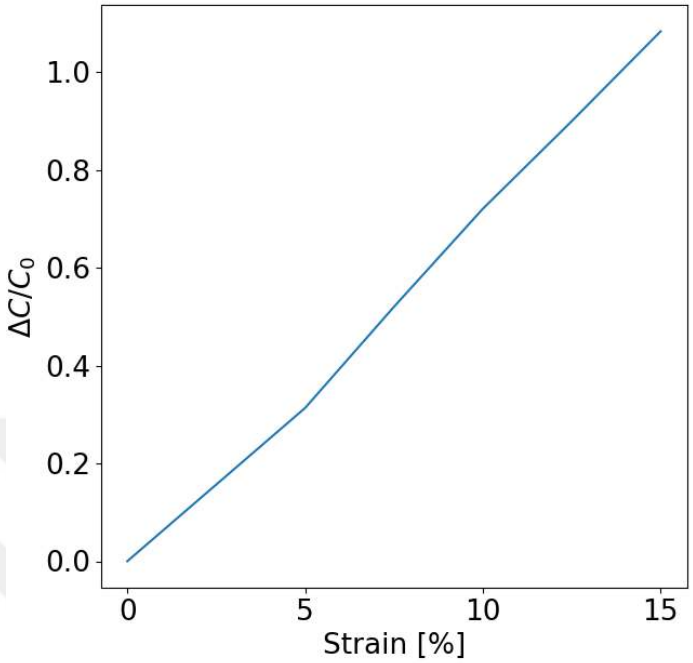

j)

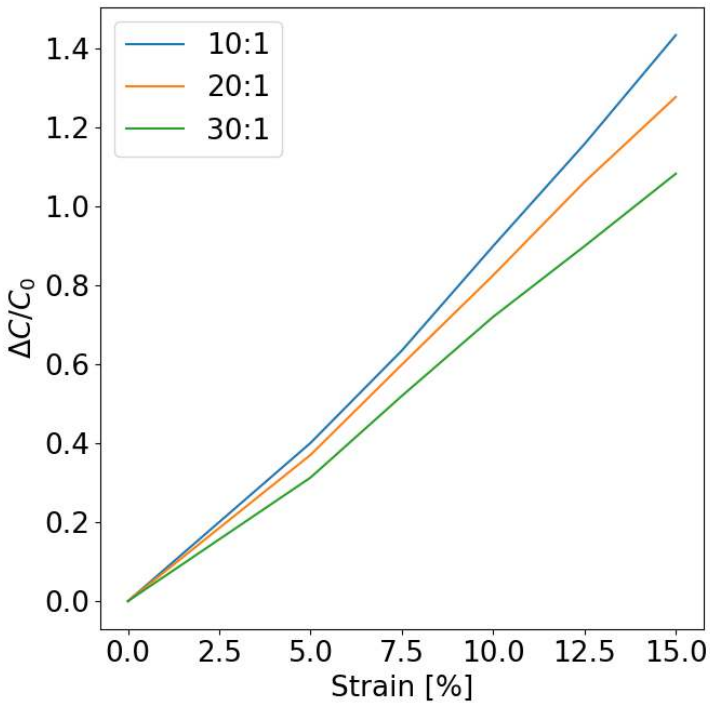

Figure 3.19: PDMS Compound optimization results. a) force-displacement results b) cyclic strain results c) calibration curve, of 10:1 ratio. d) force-displacement results e) cyclic strain results f) calibration curve, of 20:1 ratio, g) force-displacement results h) cyclic strain results i) calibration curve, of 30:1 ratio, j) Calibration curve comparison

The mechanical properties of cardiac tissue are highly dynamic, varying significantly between the phases of the cardiac cycle. During systole (contraction), myocardial tissue becomes markedly stiffer to generate the pressures necessary for blood ejection, whereas during diastole (relaxation), it softens to facilitate ventricular filling. Quantitative studies have demonstrated that the elastic modulus of myocardial tissue increases by several fold during contraction compared to relaxation. For instance, measurements in isolated rat myocardium show that the elastic modulus can rise from approximately 20–50 kPa during diastole to 100–500 kPa during systole, depending on the species and experimental conditions [82]. This dynamic stiffening is primarily attributed to sarcomere contraction and cross-bridge formation within the cardiomyocytes, in addition to extracellular matrix contributions. Understanding and accounting for these variations are crucial for accurately designing implantable sensors intended to operate in cardiac environments, as they must accommodate the wide mechanical range the tissue experiences within each heartbeat.

3.4.4 Effect of Distance Between Neutral Axis and Sensing Layer

Finally, we undertake a geometrical optimization process aimed specifically at maximizing sensitivity. This involves a detailed examination of the neutral axis, which is conceptualized as an imaginary plane running through the cross-section of a solid object undergoing bending or flexural deformation.

When a solid is subjected to bending forces, it experiences differential strain across its cross-section. Specifically, one segment of the material is elongated or stretched, while another segment is compressed. The neutral axis serves as a critical reference point within this context. It delineates the boundary in the cross-section where the material retains its original dimensions—meaning that there is no tensile or compressive strain acting on it.

To elaborate, the neutral axis is situated at a specific depth within the cross-section, where the fibers of the material experience zero elongation. Above this axis, the material remains in a state of tension, and below it, the material is in compression. This understanding of the neutral axis is essential for predicting how the structure will respond to applied loads, particularly when adjusting its geometry to improve its performance under bending conditions. By optimizing the configuration of the solid with sensitivity

maximization in mind, we aim to enhance its overall structural efficiency and performance.

In the context of implanting our sensor, it is important to consider the specific motions that will occur, primarily involving a combination of bending and relaxation. Our theoretical framework suggests that increasing the distance between the sensing layer and the neutral axis of the sensor enhances its sensitivity. This is because a greater distance allows the sensing layer to experience higher levels of strain during motion, amplifying its ability to detect changes.

However, there are significant trade-offs associated with increasing this distance. Firstly, an increased distance results in a thicker sensor, which complicates the implantation process. A thicker device may pose challenges regarding placement and could affect the overall comfort and safety for the patient. Secondly, as the distance from the neutral axis increases, the stiffness of the sensor likewise increases. This increased stiffness can hinder the natural motion of the heart, potentially leading to complications that could impact the sensor's functionality and the patient's health.

To explore these factors in greater detail, we have selected three specific distance candidates for the sensing layer: 0.75 mm, 0.95 mm, and 1.30 mm. A tensile test is conducted as a preliminary evaluation to assess the stiffness of these sensors. As anticipated, the results revealed that the sensor with a distance of 1.30 mm exhibited the highest stiffness. Conversely, the sensor with a distance of 0.75 mm displayed the lowest stiffness (Figure 3.20).

a)

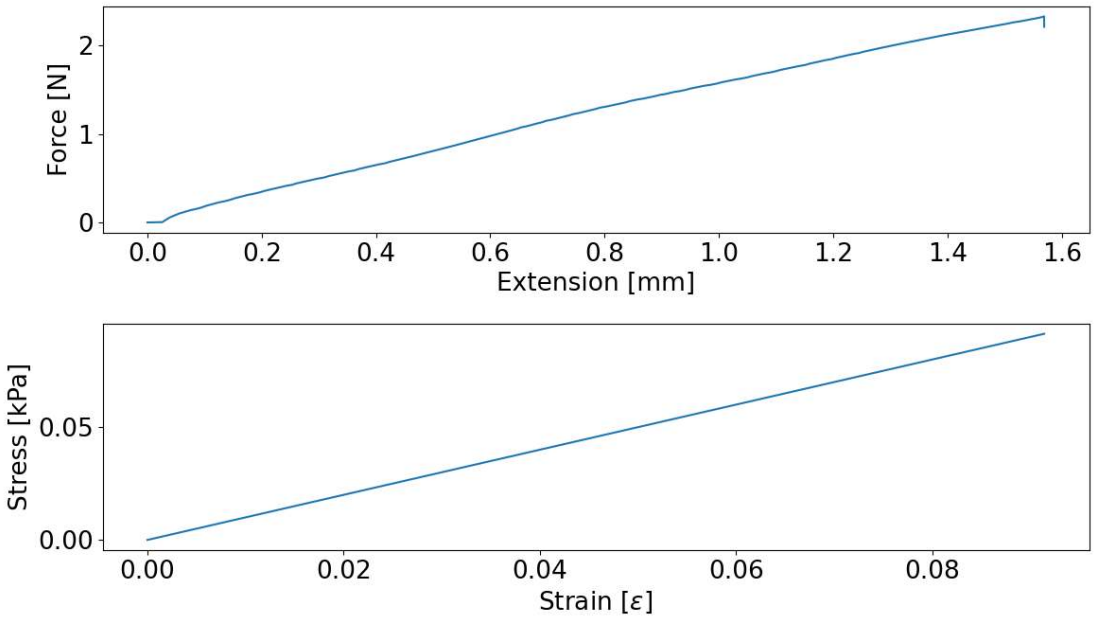
Force [N]
0
1
2
0.0
0.2
0.4
0.6
0.8
1.0
1.2
1.4
1.6
Extension [mm]

Stress [kPa]
0.00
0.05
0.00
0.02
0.04
0.06
0.08
Strain [ε]

b)

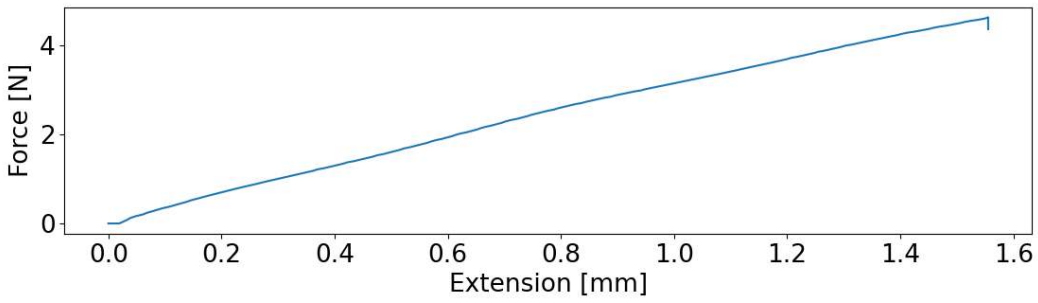
Force [N]
0
2
4
0.0
0.2
0.4
0.6
0.8
1.0
1.2
1.4
1.6
Extension [mm]

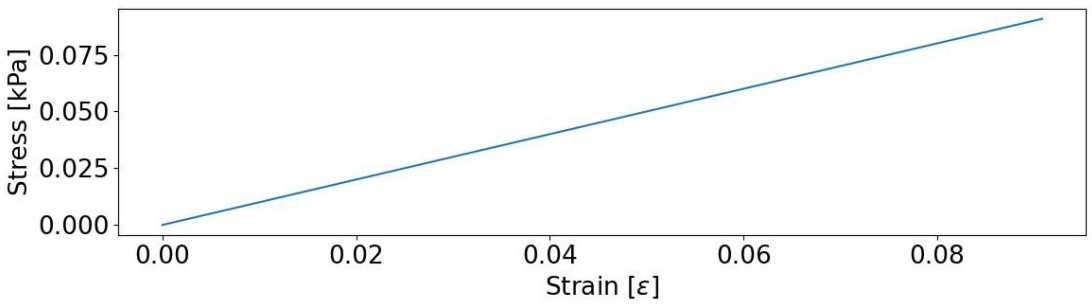
Stress [kPa]
0.000
0.025
0.050
0.075
0.00
0.02
0.04
0.06
0.08
Strain [ε]

c)

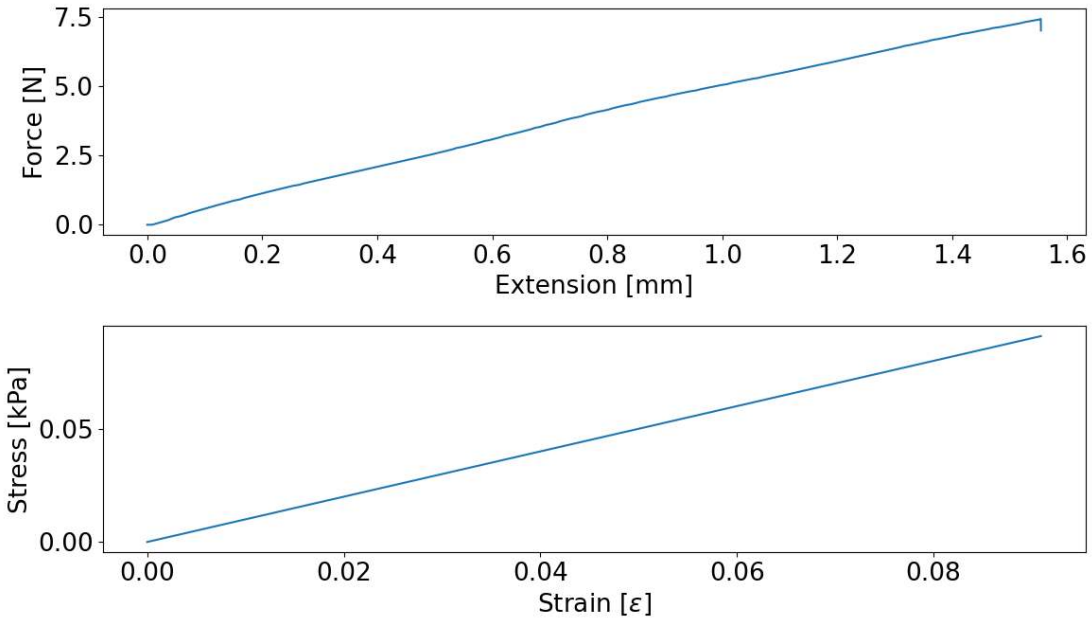

Figure 3.20: Effect of distance between neutral axis and sensing layer experiment force-displacement results. Sensor with a distance of a) 0.75 mm, b) 0.95 mm and c) 1.30 mm.

Following the initial experiments, a sensitivity test is conducted with a significant modification to the approach used in prior tests. In this instance, a setup is developed that closely mimics the heart's bent-relaxed cyclic motion, incorporating a controlled environment to ensure precision in measurements. Z-axis stage is utilized as the primary source for controlled bending, allowing consistent and measurable displacements to be applied to the system. The Zurich Instruments MFIA is employed to capture the resulting electrical signals generated during this process, known for its capability to accurately collect and analyze electrical signals. This combination of tools creates a reliable framework for assessing the sensitivity of the system under conditions that closely resemble the natural dynamics of heart motion (Figure 3.21).

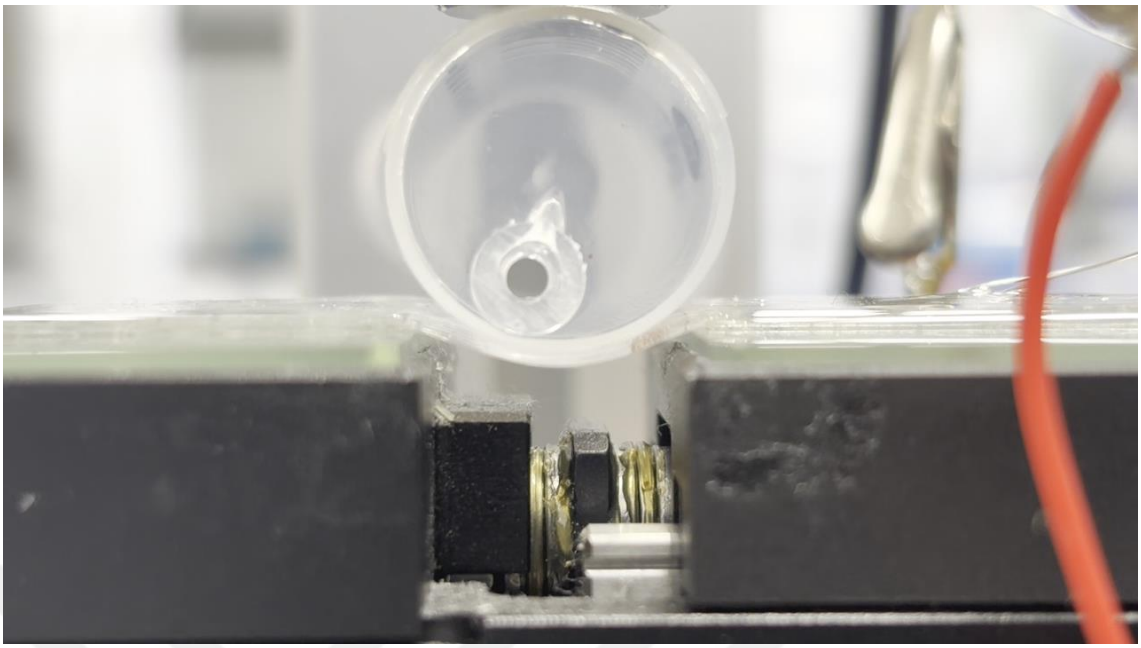

Figure 3.21: The sensor under bending test setup.

In this experiment, three sensors of varying distances were subjected to bending at three distinct levels, and the resulting capacitance responses were delicately recorded. The findings aligned well with the theoretical expectations. Among the sensors tested, the one with a distance of 1.30 mm demonstrated the highest sensitivity to bending, indicating its superior responsiveness to changes in curvature. Conversely, the sensor that measured 0.75 mm in distance exhibited the least sensitivity, making it the least effective in detecting the variations caused by bending. To quantify the bending levels, we employed a parameter known as the reciprocal of the radius of curvature (1/radius of curvature), which provides a clear metric for assessing the degree of curvature experienced by each sensor (Figure 3.22).

a)

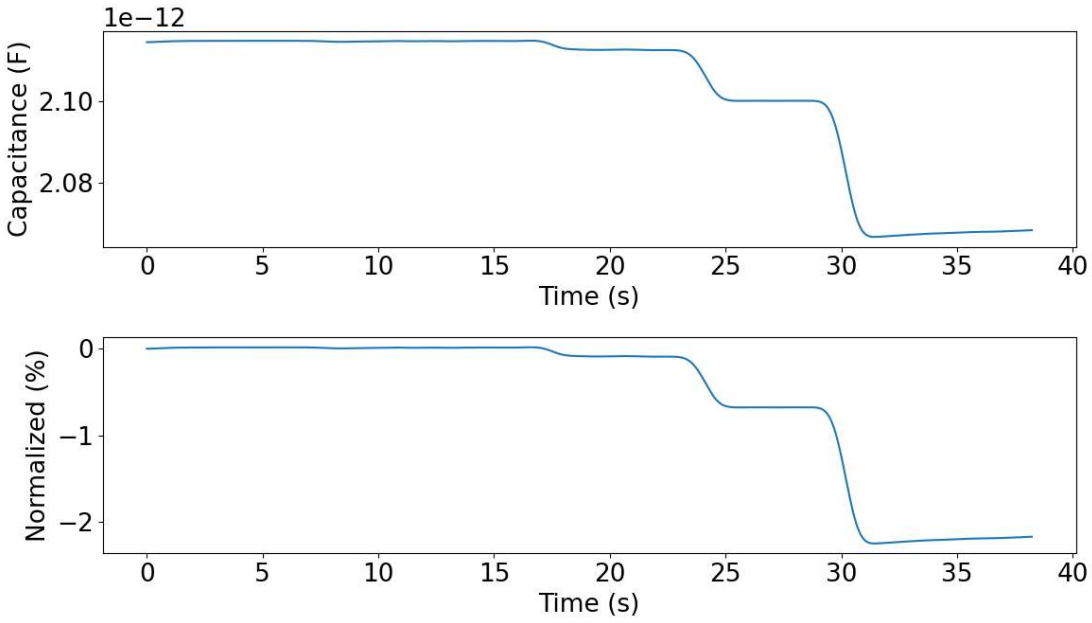
1e−12
Capacitance (F)
2.10
2.08
0
5
10
15
20
25
30
35
40
Time (s)
Normalized (%)
0
−1
−2
0
5
10
15
20
25
30
35
40
Time (s)

b)

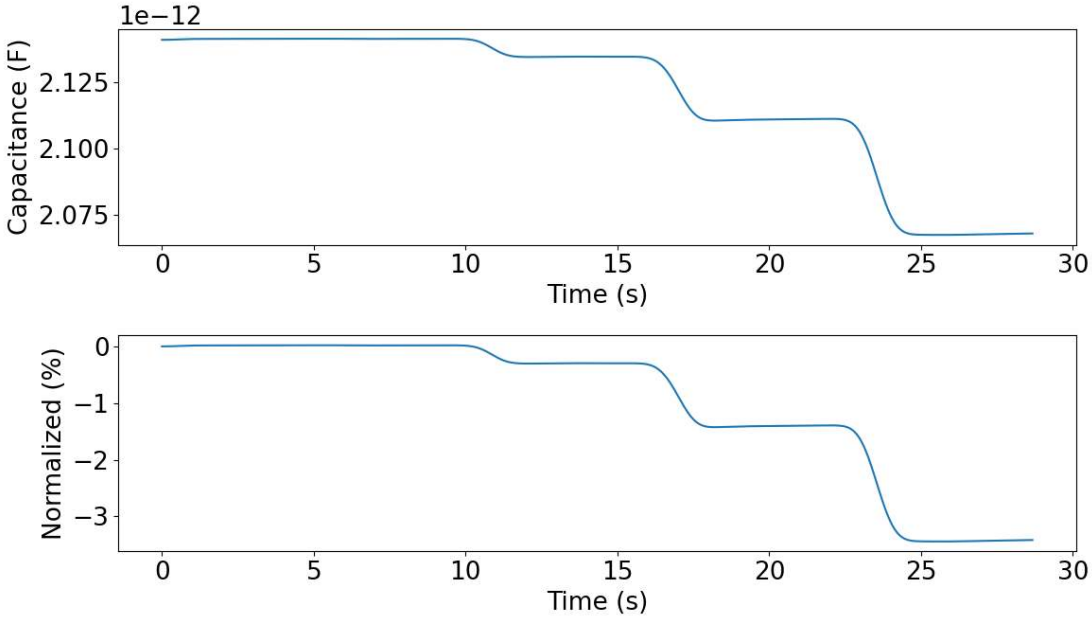
1e−12
Capacitance (F)
2.125
2.100
2.075
0
5
10
15
20
25
30
Time (s)
Normalized (%)
0
−1
−2
−3
0
5
10
15
20
25
30
Time (s)

c)

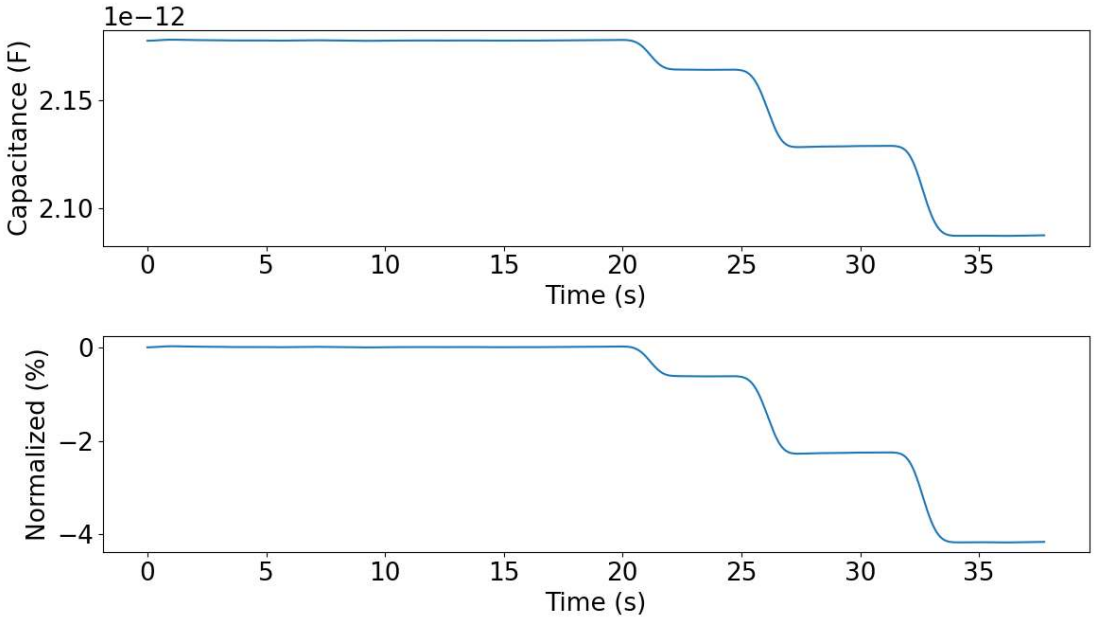
1e−12
Capacitance (F)
2.15
2.10
0
5
10
15
20
25
30
35
Time (s)
Normalized (%)
0
−2
−4
0
5
10
15
20
25
30
35
Time (s)

d)

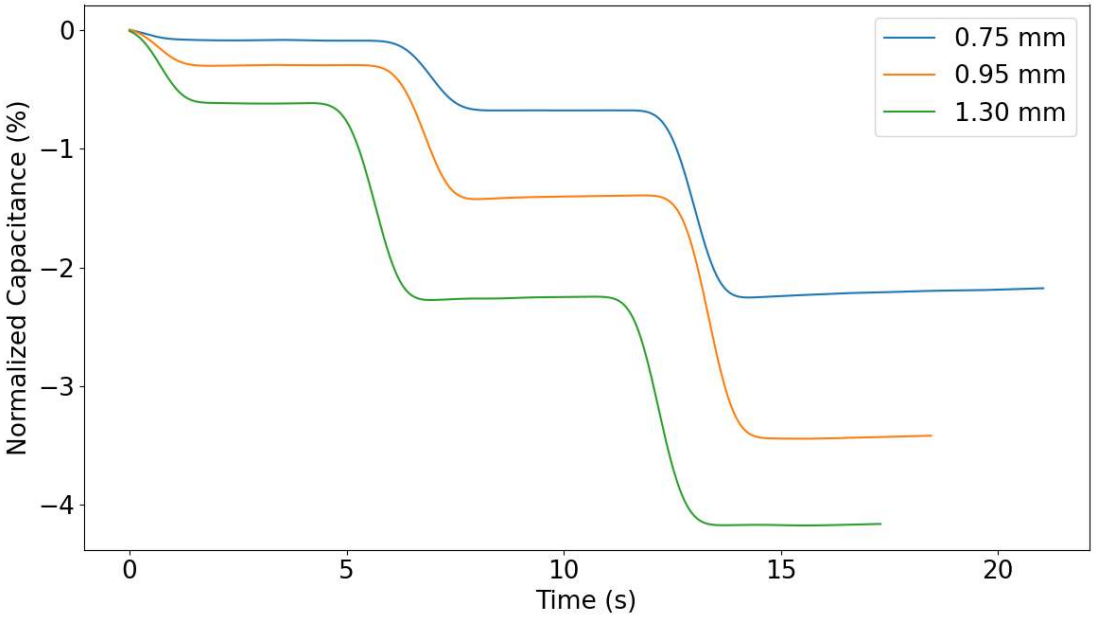
Normalized Capacitance (%)
0
−1
−2
−3
−4
0
5
10
15
20
Time (s)
0.75 mm
0.95 mm
1.30 mm

e)

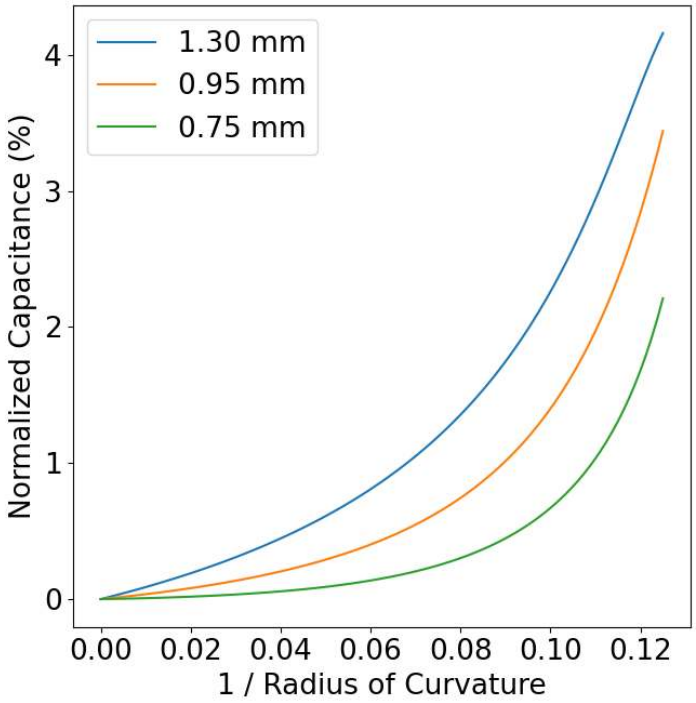

Figure 3.22: Effect of distance between neutral axis and sensing layer experiments sensitivity results. Strain results of the sensors with a distance of a) 0.75mm, b) 0.95mm and c) 1.30 mm. d) Combined strain results. e) Combined calibration curves.

3.5 Comparison of Analytical, Numerical and Experimental Models

In the plot presented in Figure 3.23, a comprehensive comparison is made between experimental, analytical, and numerical models. The discrepancies observed between the FEA results and the analytical solutions can largely be attributed to numerical errors that arise during the FEA process, as well as the inherent assumptions made when deriving the analytical solutions. Furthermore, the variations in capacitance between the experimental results and those obtained from the analytical and numerical approaches can primarily be explained by the additional electrical energy that is stored in the space between the edges of the conductive fingers. This effect is significantly influenced by the presence of fringing fields, which contribute to the total capacitance by generating electric field lines that extend beyond the immediate boundaries of the conductive elements.

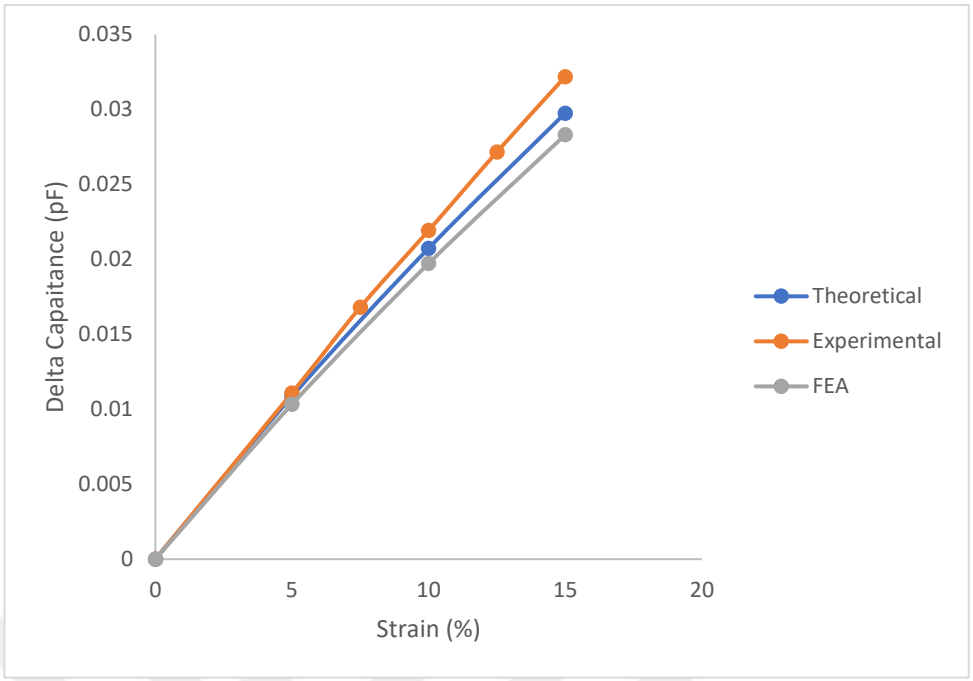

Figure 3.23: Results of, analytical, numerical and experimental models.

Chapter 4:

CONCLUSION

This thesis presents a comprehensive study on the design, fabrication, and characterization of biocompatible soft strain sensors tailored for implantable applications. By addressing the pressing need for reliable and continuous cardiac monitoring, the research contributes significantly to advancing healthcare technologies for postoperative care and long-term management of cardiovascular diseases.

The resistive strain sensor demonstrated a straightforward design and initial success in strain measurement. However, challenges such as durability under cyclic loading and sensitivity to microcrack formation highlighted the need for improvement. This led to the development of capacitive strain sensors, which leveraged interdigitated designs and capacitive sensing principles to achieve superior stability, sensitivity, and adaptability to dynamic physiological conditions. Material optimization, including the use of PDMS as the encapsulating layer, ensured biocompatibility and mechanical compatibility with soft tissues, while innovative fabrication techniques enhanced sensor performance.

Extensive testing under simulated physiological conditions validated the sensors' ability to detect subtle strain changes with high precision, even under cyclic and large-strain scenarios. The capacitive sensors, in particular, exhibited pressure insensitivity and long-term stability, making them viable for real-time cardiac function monitoring. This capability is pivotal for early detection of adverse cardiac events, personalized treatment regimens, and reducing hospital readmission rates.

The study lays a robust foundation for the integration of soft strain sensors into implantable devices, with potential applications extending beyond cardiac monitoring to other fields requiring precise, biocompatible sensing solutions. Future work can explore miniaturization, wireless telemetry, and energy-harvesting techniques to enhance the functionality and usability of these sensors in clinical settings. Ultimately, this research contributes to bridging the gap between innovative sensor technologies and improved patient outcomes in modern healthcare.

BIBLIOGRAPHY

[1] A. Groenewegen, F. H. Rutten, A. Mosterd, and A. W. Hoes, "Epidemiology of heart failure," *Eur J Heart Fail*, vol. 22, no. 8, pp. 1342–1356, Aug. 2020, doi: 10.1002/ejhf.1858.

[2] M. Urbich *et al.*, "A Systematic Review of Medical Costs Associated with Heart Failure in the USA (2014-2020)," *Pharmacoeconomics*, vol. 38, no. 11, pp. 1219–1236, Nov. 2020, doi: 10.1007/s40273-020-00952-0.

[3] K. Stokes, "The Biocompatibility and Biostability of New Cardiovascular Materials and Devices," in *Implantable Neural Prostheses 2: Techniques and Engineering Approaches*, D. Zhou and E. Greenbaum, Eds., New York, NY: Springer, 2010, pp. 1–26. doi: 10.1007/978-0-387-98120-8_1.

[4] J. A. Rushakoff and E. P. Kransdorf, "Heart Transplant in Older Adults," *Curr Transplant Rep*, vol. 9, no. 1, pp. 48–54, 2022, doi: 10.1007/s40472-022-00358-1.

[5] W. Greatbatch and C. F. Holmes, "History of implantable devices," *IEEE Engineering in Medicine and Biology Magazine*, vol. 10, no. 3, pp. 38–41, Sep. 1991, doi: 10.1109/51.84185.

[6] S. Jhanji, B. Thomas, A. Ely, D. Watson, C. J. Hinds, and R. M. Pearse, "Mortality and utilisation of critical care resources amongst high-risk surgical patients in a large NHS trust," *Anaesthesia*, vol. 63, no. 7, pp. 695–700, Jul. 2008, doi: 10.1111/j.1365-2044.2008.05560.x.

[7] M. K. Ong *et al.*, "Effectiveness of Remote Patient Monitoring After Discharge of Hospitalized Patients With Heart Failure: The Better Effectiveness After Transition -- Heart Failure (BEAT-HF) Randomized Clinical Trial," *JAMA Intern Med*, vol. 176, no. 3, pp. 310–318, Mar. 2016, doi: 10.1001/jamainternmed.2015.7712.

[8] K. Takeda *et al.*, "Incidence and clinical significance of late right heart failure during continuous-flow left ventricular assist device support," *J Heart Lung Transplant*, vol. 34, no. 8, pp. 1024–1032, Aug. 2015, doi: 10.1016/j.healun.2015.03.011.

[9] T. M. Ruppar, P. S. Cooper, D. R. Mehr, J. M. Delgado, and J. M. Dunbar-Jacob, "Medication Adherence Interventions Improve Heart Failure Mortality and Readmission Rates: Systematic Review and Meta-Analysis of Controlled Trials," *J Am Heart Assoc*, vol. 5, no. 6, p. e002606, Jun. 2016, doi: 10.1161/JAHA.115.002606.

[10] R. A. Clark, S. C. Inglis, F. A. McAlister, J. G. F. Cleland, and S. Stewart, "Telemonitoring or structured telephone support programmes for patients with chronic heart failure: systematic review and meta-analysis," *BMJ*, vol. 334, no. 7600, p. 942, May 2007, doi: 10.1136/bmj.39156.536968.55.

[11] J. F. Veenis and J. J. Brugts, "Remote monitoring of chronic heart failure patients: invasive versus non-invasive tools for optimising patient management," *Neth Heart J*, vol. 28, no. 1, pp. 3–13, Jan. 2020, doi: 10.1007/s12471-019-01342-8.

[12] A. T. Pezzella, "Global aspects of cardiothoracic surgery with focus on developing countries," *Asian Cardiovasc Thorac Ann*, vol. 18, no. 3, pp. 299–310, Jun. 2010, doi: 10.1177/0218492310370060.

[13] M. Dalén, L. H. Lund, T. Ivert, M. J. Holzmann, and U. Sartipy, "Survival After Coronary Artery Bypass Grafting in Patients With Preoperative Heart Failure and Preserved vs Reduced Ejection Fraction," *JAMA Cardiol*, vol. 1, no. 5, pp. 530–538, Aug. 2016, doi: 10.1001/jamacardio.2016.1465.

[14] ' Mateja K. Jezovnik', 'Igor D. Gregoric', and 'Pavel Poredos', "Medical complications in patients with LVAD devices." Accessed: Nov. 19, 2024. [Online].

Available: https://www.escardio.org/Journals/E-Journal-of-Cardiology-Practice/Volume-14/Medical-complications-in-patients-with-LVAD-devices
[15] "CFR - Code of Federal Regulations Title 21." Accessed: Nov. 19, 2024. [Online]. Available: https://www.accessdata.fda.gov/scripts/cdrh/cfdocs/cfcfr/CFRsearch.cfm?CFRPart=812
[16] S. F. Khuri, "The NSQIP: a new frontier in surgery," *Surgery*, vol. 138, no. 5, pp. 837–843, Nov. 2005, doi: 10.1016/j.surg.2005.08.016.
[17] G. J. Murphy and G. D. Angelini, "Side Effects of Cardiopulmonary Bypass:," *Journal of Cardiac Surgery*, vol. 19, no. 6, pp. 481–488, 2004, doi: 10.1111/j.0886-0440.2004.04101.x.
[18] L. W. Busse, N. Barker, and C. Petersen, "Vasoplegic syndrome following cardiothoracic surgery—review of pathophysiology and update of treatment options," *Critical Care*, vol. 24, no. 1, p. 36, Feb. 2020, doi: 10.1186/s13054-020-2743-8.
[19] G. W. Fischer and M. A. Levin, "Vasoplegia During Cardiac Surgery: Current Concepts and Management," *Seminars in Thoracic and Cardiovascular Surgery*, vol. 22, no. 2, pp. 140–144, Jun. 2010, doi: 10.1053/j.semtcvs.2010.09.007.
[20] C. Krittanawong *et al.*, "Integration of novel monitoring devices with machine learning technology for scalable cardiovascular management," *Nat Rev Cardiol*, vol. 18, no. 2, pp. 75–91, Feb. 2021, doi: 10.1038/s41569-020-00445-9.
[21] S. Emmons-Bell, C. Johnson, and G. Roth, "Prevalence, incidence and survival of heart failure: a systematic review," *Heart*, vol. 108, no. 17, pp. 1351–1360, Aug. 2022, doi: 10.1136/heartjnl-2021-320131.
[22] K. Dharmarajan *et al.*, "Diagnoses and timing of 30-day readmissions after hospitalization for heart failure, acute myocardial infarction, or pneumonia," *JAMA*, vol. 309, no. 4, pp. 355–363, Jan. 2013, doi: 10.1001/jama.2012.216476.
[23] G. de Couto, M. Ouzounian, and P. P. Liu, "Early detection of myocardial dysfunction and heart failure," *Nat Rev Cardiol*, vol. 7, no. 6, pp. 334–344, Jun. 2010, doi: 10.1038/nrcardio.2010.51.
[24] D. L. Mann and M. R. Bristow, "Mechanisms and models in heart failure: the biomechanical model and beyond," *Circulation*, vol. 111, no. 21, pp. 2837–2849, May 2005, doi: 10.1161/CIRCULATIONAHA.104.500546.
[25] D. L. Mann and G. M. Felker, "Mechanisms and Models in Heart Failure: A Translational Approach," *Circ Res*, vol. 128, no. 10, pp. 1435–1450, May 2021, doi: 10.1161/CIRCRESAHA.121.318158.
[26] S. Mandala, T. Cai Di, M. S. Sunar, and null Adiwijaya, "ECG-based prediction algorithm for imminent malignant ventricular arrhythmias using decision tree," *PLoS One*, vol. 15, no. 5, p. e0231635, 2020, doi: 10.1371/journal.pone.0231635.
[27] U. R. Acharya, H. Fujita, S. L. Oh, Y. Hagiwara, J. H. Tan, and M. Adam, "Application of deep convolutional neural network for automated detection of myocardial infarction using ECG signals," *Information Sciences*, vol. 415–416, pp. 190–198, Nov. 2017, doi: 10.1016/j.ins.2017.06.027.
[28] L. Lambert, K. Brown, E. Segal, J. Brophy, J. Rodes-Cabau, and P. Bogaty, "Association between timeliness of reperfusion therapy and clinical outcomes in ST-elevation myocardial infarction," *JAMA*, vol. 303, no. 21, pp. 2148–2155, Jun. 2010, doi: 10.1001/jama.2010.712.

[29] S. Chun *et al.*, "Lifetime Analysis of Hospitalizations and Survival of Patients Newly Admitted With Heart Failure," *Circulation: Heart Failure*, vol. 5, no. 4, pp. 414–421, Jul. 2012, doi: 10.1161/CIRCHEARTFAILURE.111.964791.
[30] C. D. Kemp and J. V. Conte, "The pathophysiology of heart failure," *Cardiovasc Pathol*, vol. 21, no. 5, pp. 365–371, 2012, doi: 10.1016/j.carpath.2011.11.007.
[31] S. Shaefi *et al.*, "Vasoplegia After Cardiovascular Procedures-Pathophysiology and Targeted Therapy," *J Cardiothorac Vasc Anesth*, vol. 32, no. 2, pp. 1013–1022, Apr. 2018, doi: 10.1053/j.jvca.2017.10.032.
[32] M. Metra *et al.*, "Worsening of chronic heart failure: definition, epidemiology, management and prevention. A clinical consensus statement by the Heart Failure Association of the European Society of Cardiology," *European Journal of Heart Failure*, vol. 25, no. 6, pp. 776–791, 2023, doi: 10.1002/ejhf.2874.
[33] P. Jong, S. Yusuf, M. F. Rousseau, S. A. Ahn, and S. I. Bangdiwala, "Effect of enalapril on 12-year survival and life expectancy in patients with left ventricular systolic dysfunction: a follow-up study," *Lancet*, vol. 361, no. 9372, pp. 1843–1848, May 2003, doi: 10.1016/S0140-6736(03)13501-5.
[34] B. A. Popescu, C. C. Beladan, S. F. Nagueh, and O. A. Smiseth, "How to assess left ventricular filling pressures by echocardiography in clinical practice," *Eur Heart J Cardiovasc Imaging*, vol. 23, no. 9, pp. 1127–1129, Aug. 2022, doi: 10.1093/ehjci/jeac123.
[35] F. Seemann *et al.*, "Noninvasive Quantification of Pressure-Volume Loops From Brachial Pressure and Cardiovascular Magnetic Resonance," *Circ Cardiovasc Imaging*, vol. 12, no. 1, p. e008493, Dec. 2019, doi: 10.1161/CIRCIMAGING.118.008493.
[36] R. Salem *et al.*, "Left ventricular end-diastolic pressure is a predictor of mortality in cardiac surgery independently of left ventricular ejection fraction," *Br J Anaesth*, vol. 97, no. 3, pp. 292–297, Sep. 2006, doi: 10.1093/bja/ael140.
[37] M.-J. Cha, H.-S. Kim, S. H. Kim, J.-H. Park, and G.-Y. Cho, "Prognostic power of global 2D strain according to left ventricular ejection fraction in patients with ST elevation myocardial infarction," *PLoS One*, vol. 12, no. 3, p. e0174160, 2017, doi: 10.1371/journal.pone.0174160.
[38] A. Ochs *et al.*, "Myocardial mechanics in dilated cardiomyopathy: prognostic value of left ventricular torsion and strain," *J Cardiovasc Magn Reson*, vol. 23, no. 1, p. 136, Dec. 2021, doi: 10.1186/s12968-021-00829-x.
[39] M. Reindl *et al.*, "Prognostic Implications of Global Longitudinal Strain by Feature-Tracking Cardiac Magnetic Resonance in ST-Elevation Myocardial Infarction," *Circ Cardiovasc Imaging*, vol. 12, no. 11, p. e009404, Nov. 2019, doi: 10.1161/CIRCIMAGING.119.009404.
[40] Y. Zheng *et al.*, "Morphological, functional, and biomechanical progression of LV remodelling in a porcine model of HFpEF," *J Biomech*, vol. 144, p. 111348, Nov. 2022, doi: 10.1016/j.jbiomech.2022.111348.
[41] R. Xu *et al.*, "Identification of early cardiac dysfunction and heterogeneity after pressure and volume overload in mice by high-frequency echocardiographic strain imaging," *Front Cardiovasc Med*, vol. 9, p. 1071249, Jan. 2023, doi: 10.3389/fcvm.2022.1071249.
[42] T. Edvardsen, T. Helle-Valle, and O. A. Smiseth, "Systolic dysfunction in heart failure with normal ejection fraction: speckle-tracking echocardiography," *Prog Cardiovasc Dis*, vol. 49, no. 3, pp. 207–214, 2006, doi: 10.1016/j.pcad.2006.08.008.

[43] M. Cameli *et al.*, "Left atrial longitudinal strain by speckle tracking echocardiography correlates well with left ventricular filling pressures in patients with heart failure," *Cardiovasc Ultrasound*, vol. 8, p. 14, Apr. 2010, doi: 10.1186/1476-7120-8-14.

[44] T. H. Marwick, S. J. Shah, and J. D. Thomas, "Myocardial Strain in the Assessment of Patients With Heart Failure: A Review," *JAMA Cardiol*, vol. 4, no. 3, pp. 287–294, Mar. 2019, doi: 10.1001/jamacardio.2019.0052.

[45] H. Motoki *et al.*, "Incremental prognostic value of assessing left ventricular myocardial mechanics in patients with chronic systolic heart failure," *J Am Coll Cardiol*, vol. 60, no. 20, pp. 2074–2081, Nov. 2012, doi: 10.1016/j.jacc.2012.07.047.

[46] A. M. Katz and E. L. Rolett, "Heart failure: when form fails to follow function," *European Heart Journal*, vol. 37, no. 5, pp. 449–454, Feb. 2016, doi: 10.1093/eurheartj/ehv548.

[47] V. Lionetti *et al.*, "Mismatch between uniform increase in cardiac glucose uptake and regional contractile dysfunction in pacing-induced heart failure," *Am J Physiol Heart Circ Physiol*, vol. 293, no. 5, pp. H2747-2756, Nov. 2007, doi: 10.1152/ajpheart.00592.2007.

[48] A. Pingitore *et al.*, "Early subclinical increase in pulmonary water content in athletes performing sustained heavy exercise at sea level: ultrasound lung comet-tail evidence," *Am J Physiol Heart Circ Physiol*, vol. 301, no. 5, pp. H2161-2167, Nov. 2011, doi: 10.1152/ajpheart.00388.2011.

[49] P. Claus, A. M. S. Omar, G. Pedrizzetti, P. P. Sengupta, and E. Nagel, "Tissue Tracking Technology for Assessing Cardiac Mechanics: Principles, Normal Values, and Clinical Applications," *JACC Cardiovasc Imaging*, vol. 8, no. 12, pp. 1444–1460, Dec. 2015, doi: 10.1016/j.jcmg.2015.11.001.

[50] T. S. Clemmensen, H. Eiskjær, B. B. Løgstrup, L. B. Ilkjær, and S. H. Poulsen, "Left ventricular global longitudinal strain predicts major adverse cardiac events and all-cause mortality in heart transplant patients," *J Heart Lung Transplant*, vol. 36, no. 5, pp. 567–576, May 2017, doi: 10.1016/j.healun.2016.12.002.

[51] E. E. C. de Waal *et al.*, "Vasoplegia after implantation of a continuous flow left ventricular assist device: incidence, outcomes and predictors," *BMC Anesthesiol*, vol. 18, no. 1, p. 185, Dec. 2018, doi: 10.1186/s12871-018-0645-y.

[52] J. L. Dorosz, D. C. Lezotte, D. A. Weitzenkamp, L. A. Allen, and E. E. Salcedo, "Performance of 3-Dimensional Echocardiography in Measuring Left Ventricular Volumes and Ejection Fraction: A Systematic Review and Meta-Analysis," *Journal of the American College of Cardiology*, vol. 59, no. 20, pp. 1799–1808, May 2012, doi: 10.1016/j.jacc.2012.01.037.

[53] P. S. Rajiah *et al.*, "Myocardial Strain Evaluation with Cardiovascular MRI: Physics, Principles, and Clinical Applications," *Radiographics*, vol. 42, no. 4, pp. 968–990, 2022, doi: 10.1148/rg.210174.

[54] R. Amacher *et al.*, "Control of ventricular unloading using an electrocardiogram-synchronized Thoratec paracorporeal ventricular assist device," *The Journal of Thoracic and Cardiovascular Surgery*, vol. 146, no. 3, pp. 710–717, Sep. 2013, doi: 10.1016/j.jtcvs.2012.12.048.

[55] J. Baan *et al.*, "Continuous measurement of left ventricular volume in animals and humans by conductance catheter.," *Circulation*, vol. 70, no. 5, pp. 812–823, Nov. 1984, doi: 10.1161/01.CIR.70.5.812.

[56] G. Ochsner *et al.*, "In Vivo Evaluation of Physiologic Control Algorithms for Left Ventricular Assist Devices Based on Left Ventricular Volume or Pressure," *ASAIO Journal*, vol. 63, no. 5, p. 568, Oct. 2017, doi: 10.1097/MAT.0000000000000533.
[57] "Transesophageal Echocardiogram," Amelia Heart & Vascular Center. Accessed: Feb. 02, 2025. [Online]. Available: https://www.ameliaheartcenter.com/transesophageal-echocardiogram/
[58] "Echocardiogram - Mayo Clinic." Accessed: Feb. 02, 2025. [Online]. Available: https://www.mayoclinic.org/tests-procedures/echocardiogram/about/pac-20393856
[59] A. M. Katz, "Ernest Henry Starling, His Predecessors, and the 'Law of the Heart,'" *Circulation*, vol. 106, no. 23, pp. 2986–2992, Dec. 2002, doi: 10.1161/01.CIR.0000040594.96123.55.
[60] A. Kovács, B. Lakatos, M. Tokodi, and B. Merkely, "Right ventricular mechanical pattern in health and disease: beyond longitudinal shortening," *Heart Fail Rev*, vol. 24, no. 4, pp. 511–520, Jul. 2019, doi: 10.1007/s10741-019-09778-1.
[61] K. G. Skaarup *et al.*, "Link between myocardial deformation phenotyping using longitudinal and circumferential strain and risk of incident heart failure and cardiovascular death," *Eur Heart J Cardiovasc Imaging*, vol. 24, no. 8, pp. 999–1006, Jul. 2023, doi: 10.1093/ehjci/jead075.
[62] S. A. Dual *et al.*, "Continuous Heart Volume Monitoring by Fully Implantable Soft Strain Sensor," *Advanced Healthcare Materials*, vol. 9, no. 19, p. 2000855, 2020, doi: 10.1002/adhm.202000855.
[63] K. Magkoutas *et al.*, "Continuous Monitoring of Blood Pressure and Vascular Hemodynamic Properties With Miniature Extravascular Hall-Based Magnetic Sensor," *JACC: Basic to Translational Science*, vol. 8, no. 5, pp. 546–564, May 2023, doi: 10.1016/j.jacbts.2022.12.008.
[64] M. Rav Acha, E. Soifer, and T. Hasin, "Cardiac Implantable Electronic Miniaturized and Micro Devices," *Micromachines*, vol. 11, no. 10, Art. no. 10, Oct. 2020, doi: 10.3390/mi11100902.
[65] A. Magalski *et al.*, "Continuous ambulatory right heart pressure measurements with an implantable hemodynamic monitor: A multicenter, 12-month follow-up study of patients with chronic heart failure," *Journal of Cardiac Failure*, vol. 8, no. 2, pp. 63–70, Apr. 2002, doi: 10.1054/jcaf.2002.32373.
[66] V. Tchantchaleishvili *et al.*, "Clinical Implications of Physiologic Flow Adjustment in Continuous-Flow Left Ventricular Assist Devices," *ASAIO Journal*, vol. 63, no. 3, p. 241, Jun. 2017, doi: 10.1097/MAT.0000000000000477.
[67] H. E. Verdejo *et al.*, "Comparison of a Radiofrequency-Based Wireless Pressure Sensor to Swan-Ganz Catheter and Echocardiography for Ambulatory Assessment of Pulmonary Artery Pressure in Heart Failure," *Journal of the American College of Cardiology*, vol. 50, no. 25, pp. 2375–2382, Dec. 2007, doi: 10.1016/j.jacc.2007.06.061.
[68] G. de Simone *et al.*, "Estimation of left ventricular chamber and stroke volume by limited M-mode echocardiography and validation by two-dimensional and Doppler echocardiography," *Am J Cardiol*, vol. 78, no. 7, pp. 801–807, Oct. 1996, doi: 10.1016/s0002-9149(96)00425-0.
[69] F. Grothues, J. C. Moon, N. G. Bellenger, G. S. Smith, H. U. Klein, and D. J. Pennell, "Interstudy reproducibility of right ventricular volumes, function, and mass with cardiovascular magnetic resonance," *Am Heart J*, vol. 147, no. 2, pp. 218–223, Feb. 2004, doi: 10.1016/j.ahj.2003.10.005.

[70] Z. Sun, G. H. Choo, and K. H. Ng, “Coronary CT angiography: current status and continuing challenges,” *Br J Radiol*, vol. 85, no. 1013, pp. 495–510, May 2012, doi: 10.1259/bjr/15296170.

[71] R. L. Summers, W. C. Shoemaker, W. F. Peacock, D. S. Ander, and T. G. Coleman, “Bench to bedside: electrophysiologic and clinical principles of noninvasive hemodynamic monitoring using impedance cardiography,” *Acad Emerg Med*, vol. 10, no. 6, pp. 669–680, Jun. 2003, doi: 10.1111/j.1553-2712.2003.tb00054.x.

[72] J. Huygh, Y. Peeters, J. Bernards, and M. L. N. G. Malbrain, “Hemodynamic monitoring in the critically ill: an overview of current cardiac output monitoring methods,” *F1000Res*, vol. 5, p. F1000 Faculty Rev-2855, Dec. 2016, doi: 10.12688/f1000research.8991.1.

[73] W. T. Abraham *et al.*, “Wireless pulmonary artery haemodynamic monitoring in chronic heart failure: a randomised controlled trial,” *Lancet*, vol. 377, no. 9766, pp. 658–666, Feb. 2011, doi: 10.1016/S0140-6736(11)60101-3.

[74] C. M. Boutry *et al.*, “Biodegradable and flexible arterial-pulse sensor for the wireless monitoring of blood flow,” *Nat Biomed Eng*, vol. 3, no. 1, Art. no. 1, Jan. 2019, doi: 10.1038/s41551-018-0336-5.

[75] K. Sim *et al.*, “An epicardial bioelectronic patch made from soft rubbery materials and capable of spatiotemporal mapping of electrophysiological activity,” *Nat Electron*, vol. 3, no. 12, Art. no. 12, Dec. 2020, doi: 10.1038/s41928-020-00493-6.

[76] I. Pour-Ghaz, D. Hana, J. Raja, U. N. Ibebuogu, and R. N. Khouzam, “CardioMEMS: where we are and where can we go?,” *Annals of Translational Medicine*, vol. 7, no. 17, Art. no. 17, Sep. 2019, doi: 10.21037/atm.2019.07.53.

[77] J. C. Hwang *et al.*, “In situ diagnosis and simultaneous treatment of cardiac diseases using a single-device platform,” *Science Advances*, vol. 8, no. 37, p. eabq0897, Sep. 2022, doi: 10.1126/sciadv.abq0897.

[78] Z. Liu *et al.*, “Transcatheter Self-Powered Ultrasensitive Endocardial Pressure Sensor,” *Advanced Functional Materials*, vol. 29, no. 3, p. 1807560, 2019, doi: 10.1002/adfm.201807560.

[79] Y.-L. Park, D. Tepayotl-Ramirez, R. J. Wood, and C. Majidi, “Influence of cross-sectional geometry on the sensitivity and hysteresis of liquid-phase electronic pressure sensors,” *Applied Physics Letters*, vol. 101, no. 19, p. 191904, Nov. 2012, doi: 10.1063/1.4767217.

[80] H.-S. Shin, J. Ryu, C. Majidi, and Y.-L. Park, “Enhanced performance of microfluidic soft pressure sensors with embedded solid microspheres,” *J. Micromech. Microeng.*, vol. 26, no. 2, p. 025011, Jan. 2016, doi: 10.1088/0960-1317/26/2/025011.

[81] L. Cai *et al.*, “Super-stretchable, Transparent Carbon Nanotube-Based Capacitive Strain Sensors for Human Motion Detection,” *Sci Rep*, vol. 3, no. 1, p. 3048, Oct. 2013, doi: 10.1038/srep03048.

[82] G. Sommer *et al.*, “Biomechanical properties and microstructure of human ventricular myocardium,” *Acta Biomaterialia*, vol. 24, pp. 172–192, Sep. 2015, doi: 10.1016/j.actbio.2015.06.031.